

In compliance with the
Canadian Privacy Legislation
some supporting forms
may have been removed from
this dissertation.

While these forms may be included
in the document page count,
their removal does not represent
any loss of content from the dissertation.

Scalar Dispersion in Turbulent Channel Flow

by

Robert A. Lavertu

Department of Mechanical Engineering

McGill University

Montreal, Quebec, Canada

A thesis submitted to the Faculty of Graduate Studies and Research
in partial fulfillment of the requirements for the degree of
Master of Engineering

© Robert A. Lavertu, Montreal, Canada, 2002.



National Library
of Canada

Bibliothèque nationale
du Canada

Acquisitions and
Bibliographic Services

Acquisitons et
services bibliographiques

395 Wellington Street
Ottawa ON K1A 0N4
Canada

395, rue Wellington
Ottawa ON K1A 0N4
Canada

Your file *Votre référence*
ISBN: 0-612-88369-8
Our file *Notre référence*
ISBN: 0-612-88369-8

The author has granted a non-exclusive licence allowing the National Library of Canada to reproduce, loan, distribute or sell copies of this thesis in microform, paper or electronic formats.

L'auteur a accordé une licence non exclusive permettant à la Bibliothèque nationale du Canada de reproduire, prêter, distribuer ou vendre des copies de cette thèse sous la forme de microfiche/film, de reproduction sur papier ou sur format électronique.

The author retains ownership of the copyright in this thesis. Neither the thesis nor substantial extracts from it may be printed or otherwise reproduced without the author's permission.

L'auteur conserve la propriété du droit d'auteur qui protège cette thèse. Ni la thèse ni des extraits substantiels de celle-ci ne doivent être imprimés ou autrement reproduits sans son autorisation.

Canada

Abstract

Experimental results of scalar dispersion from a concentrated source in an inhomogeneous turbulent flow field are presented in this thesis.

The flow field is fully developed channel flow – one of the simplest inhomogeneous turbulent flows. A fine line source is used to inject the scalar (temperature). The temperature injection does not affect the flow field, hence it is passive. The line source is in the spanwise (z) direction of the channel, and is located at transverse (i.e., wall-normal) locations: $y/h = 0.067, 0.17,$ and 1.0 (where h is the channel half-width). Measurements of the resultant thermal plume for each source location are taken for two Reynolds numbers: 10400 and 22800 (where $Re = U_c h/\nu$: U_c is the centerline velocity and ν is the kinematic viscosity). Hot-wire anemometry and cold-wire thermometry are used to acquire velocity and temperature data, respectively.

It is shown that the downstream decay of the mean temperature rise is less than that of isotropic grid-generated turbulence and homogenous turbulent shear flow. The peak RMS temperature fluctuation also decays at a slower rate. For the near-wall source locations, the peak of the transverse RMS temperature profile drifts toward the channel centerline with increasing downstream distance from the source. Also, for the near-wall source locations, the scalar PDF is quasi-Gaussian, indicating improved mixing in that region. As the plume is traversed toward the centerline, the PDF evolves into a very positively skewed shape.

An extensive database of the thermal plume is compiled, which consists of the mean, RMS, and skewness profiles of the temperature field, PDFs of the temperature field, and temperature-velocity correlations. This database can be used to test numerical and/or theoretical models, highlighting their strengths and weaknesses.

Résumé

Des résultats expérimentaux sur la dispersion des scalaires à partir d'une source concentrée en écoulement turbulent non-homogène sont présentés dans ce mémoire.

L'écoulement étudié est un écoulement de canal pleinement développé, c'est-à-dire l'un des écoulements turbulents inhomogènes le plus simple. Une fine source linéaire est utilisée pour injecter le scalaire (température). L'injection de la température n'influence pas l'écoulement, la température est donc passive. La source linéaire est située en direction de la profondeur (z) du tunnel à des distances (perpendiculaires au mur): $y/h = 0.067, 0.17$ et 1.0 (h étant la moitié de la largeur du canal). Des mesures du panache thermique ainsi engendré pour chaque position de la source sont prises pour deux nombres de Reynolds : 10.4×10^3 et 22.8×10^3 ($Re = U_c h / \nu$: U_c est la vitesse au centre du canal et ν est la viscosité cinématique de l'air). L'anémométrie à température constante (fils chauds) et la thermométrie à courant constant (fils froids) sont utilisés pour mesurer les champs de vitesse et de température, respectivement.

Il est démontré que l'atténuation (en aval de la source) de l'augmentation moyenne de température est plus petite que dans le cas de la turbulence de grille ou de la turbulence homogène cisailée. L'écart type des fluctuations de température s'atténue aussi plus lentement. Pour les positions de sources près du mur, la crête du profil transversal de l'écart type de température se dirige vers le centre du canal en augmentant la distance en aval de la source. Aussi, pour des positions de sources près du mur, les fonctions de distribution de probabilité (FDP) sont presque Gaussiennes indiquant que le scalaire y est bien mélangé. En traversant le panache du mur vers le centre du tunnel, les FDPs évoluent vers une forme positivement asymétrique.

Une banque de données extensive du panache thermique est compilée. Elle consiste de profils de la moyenne, de l'écart type et du coefficient d'asymétrie du champ de température, ainsi que des FDPs et des corrélations vitesse-température. Cette banque de données peut être utilisée pour examiner

des modèles numériques et/ou théoriques en faisant ressortir leurs forces et faiblesses.

Acknowledgements

First, I would like to express my gratitude to my supervisor, Professor Mydlarski, for his assistance, guidance, and support in helping me complete this degree. He has been an excellent mentor.

A special thanks to Sébastien Beaulac, for translating the abstract and for assisting with the experimental set-up.

I would also like to extend my gratitude to Mathew McLeod for assisting with the experimental set-up.

Table of Contents

	Abstract.....	ii
	Resume.....	iii
	Acknowledgements.....	v
	Table of Contents.....	vi
	List of Figures.....	ix
	List of Tables.....	xi
	Nomenclature.....	xii
1	Introduction.....	1
	1.1 Objectives.....	1
	1.2 Background and Motivation.....	1
	1.3 Literature Review.....	7
	1.3.1 Channel Flow.....	7
	1.3.2 Turbulence Measurements.....	10
	1.3.3 Scalar Dispersion in Isotropic Grid-Generated Turbulence.....	12
	1.3.4 Scalar Dispersion in Homogeneous Turbulent Shear Flow.....	14
	1.3.5 Experimental Study of Scalar Dispersion In Inhomogeneous Flow Fields.....	16
	1.3.6 Role of Numerical Simulations in the Study of Scalar Dispersion.....	18
	1.4 Thesis Overview.....	19
2	Experimental Facility and Measurement Techniques.....	21
	2.1 Apparatus.....	21
	2.2.1 Channel Facility.....	21
	2.1.2 Injection of the Scalar.....	26
	2.2 Measurement Techniques.....	26

2.2.1	Calibration Procedure of Cold-Wires.....	27
2.2.2	Calibration Procedure of Hot-Wires for an Isothermal Flow.....	29
2.2.3	Calibration Procedure of Hot-Wires for Non-Isothermal Flows.....	31
2.2.4	Spatial and Temporal Probe Resolution.....	35
2.2.5	Analogue to Digital Conversion.....	36
2.2.6	Statistical Convergence of Data.....	37
3	Experimental Conditions and Flow Properties.....	41
3.1	Verification of the Experimental Conditions.....	41
3.1.1	Flow Verification.....	41
3.1.1.1	Low Reynolds Number.....	42
3.1.1.2	High Reynolds Number.....	44
3.1.2	Passivity of the Scalar.....	46
3.1.3	The Nature of the Thermal Wall Boundary Condition.....	48
3.1.4	Source Diameter Independence Test.....	50
3.1.5	Independence of z-direction.....	52
3.1.6	Fully Developed Test of the Passive Scalar.....	52
3.1.7	Symmetry Test.....	54
3.2	Flow Properties.....	55
4	Results.....	59
4.1	Mean Temperature Field.....	59
4.2	Fluctuating Temperature Field.....	65
4.3	Temperature PDFs.....	69
4.4	Temperature Skewness.....	73
4.5	Temperature-Velocity Correlations.....	77
4.5.1	Turbulent Heat Flux.....	77
4.5.2	Turbulent Variance Transport.....	80
4.5.3	Turbulent Heat Flux Transport.....	83

5	Conclusions.....	87
5.1	Review of the Present Work and the Contributions.....	87
5.2	Extensions of the Present Work.....	90
	References.....	92
Appendix I	PDF and Temperature-Velocity Correlation Database.....	97

List of Figures

1.1	Schematic of channel flow facility.....	8
2.1	Channel flow facility.....	21
2.2	Orientation of coordinate system.....	25
2.3	Cold-wire calibration curve.....	28
2.4	Single-normal-wire calibration curve.....	30
2.5	Calibration curve for non-isothermal flows.....	34
2.6	PDF convergence.....	40
3.1	Low Re mean velocity profiles.....	43
3.2	Low Re u_{RMS} profiles.....	43
3.3	Low Re log-law comparison.....	44
3.4	High Re mean velocity profiles.....	45
3.5	High Re u_{RMS} profiles.....	45
3.6	High Re log-law comparison.....	46
3.7	Source diameter independence test, θ_{RMS} profiles.....	51
3.8	Source diameter independence test, $S(\theta)$ profiles.....	51
3.9	Fully developed source test, θ_{RMS} profiles.....	53
3.10	Fully developed source test, $S(\theta)$ profiles.....	53
3.11	Symmetry test of U profile.....	54
3.12	Symmetry test of $P(\theta)$	55
4.1	Transverse mean temperature rise profiles.....	63
4.2	Downstream mean temperature decay.....	64
4.3	Mean temperature profile widths.....	64
4.4	Transverse θ_{RMS} profiles.....	67
4.5	Downstream decay of peak values of θ_{RMS} profiles.....	68
4.6	Widths of θ_{RMS} profiles.....	68
4.7	RMS peak drifts.....	69
4.8	PDFs for various transverse locations.....	72
4.9	PDFs for various downstream positions.....	73
4.10	Transverse $S(\theta)$ profiles.....	76

4.11	Turbulent heat fluxes.....	78
4.12	Turbulent heat fluxes.....	79
4.13	Turbulent variance transport.....	82
4.14	Turbulent variance transport.....	83
4.15	Turbulent heat flux transport.....	85
4.16	Turbulent heat flux transport.....	86
A-1	PDFs: $Re=10400$; $y_{source}=0.067$	98
A-2	Temperature-velocity correlations: $Re=10400$; $y_{source}=0.067$	99
A-3	PDFs: $Re=22800$; $y_{source}=0.067$	100
A-4	Temperature-velocity correlations: $Re=22800$; $y_{source}=0.067$	101
A-5	PDFs: $Re=10400$; $y_{source}=0.17$	102
A-6	Temperature-velocity correlations: $Re=10400$; $y_{source}=0.17$	103
A-7	PDFs: $Re=22800$; $y_{source}=0.17$	104
A-8	Temperature-velocity correlations: $Re=22800$; $y_{source}=0.17$	105
A-9	PDFs: $Re=10400$; $y_{source}=1.0$	106
A-10	Temperature-velocity correlations: $Re=10400$; $y_{source}=1.0$	107
A-11	PDFs: $Re=22800$; $y_{source}=1.0$	108
A-12	Temperature-velocity correlations: $Re=22800$; $y_{source}=1.0$	109

List of Tables

1.1	Different regions of flow field.....	10
2.1	Moment convergence table.....	39
3.1	Longitudinal variation of higher-order moments along the channel centerline for the low Re case.....	44
3.2	Longitudinal variation of higher-order moments along the channel centerline for the high Re case.....	45
3.3	Re_{source}	47
3.4	Low Re flow properties.....	57
3.5	High Re flow properties.....	58
4.1	Experimental conditions.....	59
4.2	Widths of θ_{RMS} profiles.....	69

Nomenclature

A	Hot-wire calibration constant for non-isothermal flows, and log-law constant
\bar{A}	Hot-wire calibration constant
B	Hot-wire calibration constant for non-isothermal flows
\bar{B}	Hot-wire calibration constant
Bi	Biot number
C	Cold-wire calibration constant
D	Cold-wire calibration constant, and wire diameter
d_{source}	Source diameter
E	Hot-wire output voltage
E_T	Cold-wire output voltage
$E(\bullet)$	Power spectrum
f	Frequency
g	Gravitational acceleration
h	Channel half width
h_{AV}	Average convective heat transfer coefficient
$K(a)$	Kurtosis of variable a
k	Longitudinal cooling constant (for a hot-wire)
L	Length of the test section, and wire length
n	Decay exponent or hot-wire calibration constant
Nu	Nusselt number
P	Mean pressure
\tilde{P}	Instantaneous pressure
p	Fluctuating pressure
P_{source}	Source power per unit length
\hat{P}	Non-dimensional pressure
$P(a)$	Probability of variable a
Pr	Prandtl number

q'	Heat transfer rate per unit length
Re	Reynolds number based on h , U_c , and ν
Re_{source}	Source Reynolds number at film temperature
$Re_{source-cold}$	Source Reynolds number at ambient temperature
Re_λ	Microscale Reynolds number
Re_τ	Reynolds number based on h , u^* , and ν
S_{ij}	Mean rate of strain
s_{ij}	Fluctuating rate of strain
$S(a)$	Skewness of variable a
T	Mean temperature
\tilde{T}	Instantaneous temperature
T_{film}	Film temperature
T_{wa}	X-wire calibration constant
T_{wb}	X-wire calibration constant
t	Time
t_L	Lagrangian integral time scale
t_{wall}	Plexiglas thickness
u, v, w	Components of fluctuating velocity
\hat{u}, \hat{v}	Non-dimensional velocity
u^*	Friction velocity
U, V, W	Components of mean velocity
\tilde{U}_i	Instantaneous velocity
U^+	Mean velocity non-dimensionalized by u^*
U_N	Equivalent normal velocity
U_c	Velocity at the channel centerline
\hat{U}	Non-dimensional velocity
\vec{V}	Velocity vector
w	Spanwise channel dimension
x, y, z	Cartesian co-ordinate axes

\hat{x}, \hat{y}	Non-dimensional Cartesian coordinates
y^+	Non-dimensional coordinate (in wall-units)
y_{source}	Location of line source w.r.t the y-axis
β	Angle between the velocity vector and the x-axis
γ	Thermal diffusivity
ε	Dissipation of turbulent kinetic energy
ε_0	Molecular dissipation of variance of the temperature fluctuation
η	Kolmogorov microscale
θ	Fluctuating temperature, and effective angle of an X-wire
l	Integral length scale
κ	Von Karman constant
κ_1	Longitudinal wavenumber
κ_{air}	Thermal conductivity of air
$\kappa_{\text{Plexiglas}}$	Thermal conductivity of Plexiglas
λ	Taylor microscale
ν	Kinematic viscosity
ρ	Density
ρ_{ab}	Correlation coefficient of variables a and b
σ	Standard deviation of a Gaussian profile
τ_w	Wall shear stress

Chapter 1

Introduction

1.1 Objectives

The main objective of this thesis is to experimentally study scalar dispersion in an inhomogeneous turbulent flow field. The flow under consideration is one of the simplest inhomogeneous turbulent flows, fully developed high-aspect-ratio channel flow. The flow inhomogeneity is only in one direction - the wall normal direction - thus isolating its effect on the scalar dispersion to one dimension. The scalar (temperature) is injected via a concentrated source, as in many practical situations, and detailed measurements of the resulting thermal plume are studied. Neither the physical size of the injection mechanism (the concentrated source) nor the resultant thermal plume affect the flow field, hence the scalar is passive.

1.2 Background and Motivation

The majority of flows, whether occurring in nature or manmade, are turbulent. One of the many characteristics of turbulent flows is their excellent ability to transport quantities such as momentum, energy, and contaminants. This highly diffusive nature of turbulence is sometimes an undesired phenomenon, as in the increased skin friction of an airfoil or the increased pressure drop in pipe flow (when compared to laminar flow). On the other hand, this diffusive nature is essential to many processes, such as combustion or the

dispersion of pollutants in the earth's atmosphere. It is therefore desirable to have a complete understanding of the mixing processes in a turbulent flow field.

Turbulent flows have been studied for well over a hundred years since the pioneering work of Reynolds in the late nineteenth century. Turbulent flows are described by the governing equations of fluid mechanics (Navier-Stokes equations)

$$\frac{\partial \tilde{U}_i}{\partial t} + \tilde{U}_j \frac{\partial \tilde{U}_i}{\partial x_j} = -\frac{1}{\rho} \frac{\partial \tilde{P}}{\partial x_i} + \nu \frac{\partial^2 \tilde{U}_i}{\partial x_j \partial x_j} . \quad (1-1)$$

However, a solution to these equations for turbulent flows is time dependent, three-dimensional, and extremely sensitive to initial and boundary conditions. It is common practice to decompose all variables into mean and fluctuating values and then average the equations of motion. This is known as "Reynolds averaging." However, this averaging introduces new variables, resulting in a set of unclosed equations where the number of independent variables is greater than the number of equations. Although progress has been made in understanding closure models for various classes of turbulent flows, no general model exists today for the complete description of turbulent flow fields. The desire to universally describe turbulent flows from their fundamental principles is ultimately the goal of turbulence research.

The first theoretical study of scalar dispersion from a concentrated source was by Taylor, in 1935. Since this time, much work has been done experimentally, numerically, and theoretically in an attempt to predict the dispersion of a passive scalar. Scalar mixing and dispersion is not only interesting from a practical viewpoint, as in the design of more efficient fuel

injectors or the accurate prediction of the concentration of contaminants released from a smoke stack, it lends insight into the study of the turbulent flow field itself. Scalar dispersion is completely governed by the advection-diffusion equation

$$\frac{\partial \tilde{T}}{\partial t} + \tilde{U}_i \frac{\partial \tilde{T}}{\partial x_i} = \gamma \frac{\partial^2 \tilde{T}}{\partial x_i \partial x_i} \quad (1-2)$$

which is considerably simpler than the Navier-Stokes equations (momentum equations), yet the manner in which turbulence mixes contaminants and momentum is remarkably similar. Undoubtedly, a complete understanding of the scalar mixing process would offer valuable insight into the governing physical mechanisms of the turbulent flows themselves.

To obtain the mean equations of motion for a statistically stationary turbulent flow of a constant density, constant viscosity, Newtonian fluid, the instantaneous velocity and pressure are decomposed into mean and fluctuating components (where uppercase denotes the mean component and lowercase denotes the fluctuating component), substituted into the Navier-Stokes equations, and averaged (where time averaging of fluctuating variables is denoted by $\langle \cdot \rangle$). This results in:

$$U_j \frac{\partial U_i}{\partial x_j} = -\frac{1}{\rho} \frac{\partial P}{\partial x_i} + \nu \frac{\partial^2 U_i}{\partial x_j \partial x_j} - \frac{\partial \langle u_i u_j \rangle}{\partial x_j} \quad (1-3)$$

The equation for the (statistically stationary) turbulent kinetic energy is obtained by multiplying the Navier-Stokes equations by the instantaneous velocity, Reynolds averaging all of the terms, and subtracting out the mean kinetic energy (not shown). This results in:

$$U_j \frac{\partial}{\partial x_j} \left(\frac{1}{2} \langle u_i u_i \rangle \right) = \left(-\frac{\partial}{\partial x_j} \left(\frac{1}{\rho} \langle u_j p \rangle + \frac{1}{2} \langle u_i u_i u_j \rangle - 2\nu \langle u_i s_{ij} \rangle \right) - \langle u_i u_j \rangle S_{ij} - 2\nu \langle s_{ij} s_{ij} \rangle \right) \quad (1-4)$$

where:

$$S_{ij} = \frac{1}{2} \left(\frac{\partial U_i}{\partial x_j} + \frac{\partial U_j}{\partial x_i} \right) \text{ is the mean rate of strain.}$$

$$s_{ij} = \frac{1}{2} \left(\frac{\partial u_i}{\partial x_j} + \frac{\partial u_j}{\partial x_i} \right) \text{ is the fluctuating rate of strain.}$$

$$U_j \frac{\partial}{\partial x_j} \left(\frac{1}{2} \langle u_i u_i \rangle \right) \text{ is the advection of turbulent kinetic energy by the mean flow.}$$

$$-\frac{\partial}{\partial x_j} \frac{1}{\rho} \langle u_j p \rangle \text{ is the pressure fluctuation gradient work.}$$

$$-\frac{\partial}{\partial x_j} \frac{1}{2} \langle u_i u_i u_j \rangle \text{ is the turbulent transport of turbulent kinetic energy.}$$

$$\frac{\partial}{\partial x_j} 2\nu \langle u_i s_{ij} \rangle \text{ is the molecular transport of turbulent kinetic energy.}$$

$$-\langle u_i u_j \rangle S_{ij} \text{ is the production of turbulent kinetic energy by a mean velocity gradient.}$$

$$2\nu \langle s_{ij} s_{ij} \rangle \text{ is the dissipation of turbulent kinetic energy into internal energy, } \varepsilon.$$

The equation for the statistically stationary mean temperature field for a turbulent flow of a constant property fluid is obtained by decomposing the instantaneous temperature and velocity into a mean and fluctuating component (T denotes the mean temperature and θ the fluctuating component), substituting

the decomposed temperature and velocity into the advection-diffusion equation, and averaging, which results in:

$$U_i \frac{\partial T}{\partial x_i} = \gamma \frac{\partial^2 T}{\partial x_i \partial x_i} - \frac{\partial \langle \theta u_i \rangle}{\partial x_i}. \quad (1-5)$$

The governing equation for the temperature variance ($\langle \theta^2 \rangle$) under the same conditions is obtained by subtracting equation 1-5 from the advection-diffusion equation, multiplying by θ , decomposing the instantaneous variables into mean and fluctuating values, and averaging, which results in:

$$U_i \frac{\partial \langle \theta^2 \rangle}{\partial x_i} = -2 \langle \theta u_i \rangle \frac{\partial T}{\partial x_i} - \frac{\partial \langle \theta^2 u_i \rangle}{\partial x_i} + \gamma \frac{\partial^2 \langle \theta^2 \rangle}{\partial x_i \partial x_i} - 2\gamma \langle \frac{\partial \theta}{\partial x_i} \frac{\partial \theta}{\partial x_i} \rangle \quad (1-6)$$

where:

$U_i \frac{\partial \langle \theta^2 \rangle}{\partial x_i}$ is the advection of temperature variance by the mean flow.

$-2 \langle \theta u_i \rangle \frac{\partial T}{\partial x_i}$ is the production of temperature variance by a mean temperature gradient.

$-\frac{\partial \langle \theta^2 u_i \rangle}{\partial x_i}$ is the turbulent transport of temperature variance.

$\gamma \frac{\partial^2 \langle \theta^2 \rangle}{\partial x_i \partial x_i}$ is the molecular transport of temperature variance.

$2\gamma \langle \frac{\partial \theta}{\partial x_i} \frac{\partial \theta}{\partial x_i} \rangle$ is the molecular "dissipation" or smearing rate of temperature variance, ϵ_θ .

Due to the resulting simplifications of the governing equations that can be made, and due to the importance of first understanding more fundamental

problems, much scalar dispersion work from concentrated sources has been done in homogeneous flows. A flow field is homogeneous if the statistical properties of the fluctuating variables are independent of coordinate system translations. If a turbulent flow field's statistical properties are also independent of coordinate system rotations and reflections, the flow field is isotropic. The mean and root-mean-square (RMS)¹ temperature profiles produced by a line source in isotropic grid-generated turbulence have been documented in detail by Warhaft (1984) and Stapountzis and al. (1986). As well, mean and RMS temperature profiles produced by a line source in homogenous turbulent shear flow have been documented in detail by Karnik and Tavoularis (1989) and Chung and Kyong (1989). Although these flows are not of immediate practical engineering importance, they are fundamental to the understanding of turbulence.

Some effort has been placed on scalar dispersion from concentrated sources in inhomogeneous turbulent flows, such as wakes, boundary layers, mixing layers, and jets. Examples of some of these studies are addressed in section 1.3.5. These flows are of engineering significance, however are inhomogeneous in more than one direction, making it more difficult to ascertain how the inhomogeneity affects the dispersion. The present work hopes to shed new light on the underlying physics of scalar dispersion in an inhomogeneous turbulent flow and to serve as a stepping stone between the extensive progress in fundamental flows and the newer results in more practical engineering flows.

¹ The RMS of a variable is the square root of its variance.

1.3 Literature Review

There exists many books and reviews that treat the subject of turbulence, fluid mechanics measurement techniques, and scalar dispersion. Some examples of texts that cover the theory of turbulence have been written by: Batchelor (1959), Monin and Yaglom (1971), Tennekes and Lumley (1972), Hinze (1975), Townsend (1976), Frisch (1995), Lesieur (1997), and Pope (2000). Works treating fluid mechanics measurements, with emphasis on the techniques used in this thesis, have been given by Brunn (1995), Paranthoen and Lecordier (1996), and Goldstein (1996). Reviews of passive scalar dispersion can be found in; Hinze (1975), Karnik and Tavoularis (1989), Sreenivasan (1991), and Warhaft (2000).

The remainder of this literature review focuses on topics directly related to this thesis. These topics include channel flow, turbulence measurement techniques, scalar dispersion in isotropic grid-generated turbulence, scalar dispersion in homogeneous turbulent shear flow, scalar dispersion in inhomogeneous turbulence, and numerically simulated scalar dispersion studies that complement experimental studies.

1.3.1 Channel Flow

As mentioned, the flow field is fully-developed high-aspect-ratio turbulent channel flow. Channel flow is one-dimensional, and the statistical properties of the turbulence vary in only one direction, the wall-normal direction. This fundamental flow has been studied extensively via theory, experimentation, and

numerical simulation. Overviews of channel flow theory can be found in Tennekes and Lumley (1972) and Pope (2000).

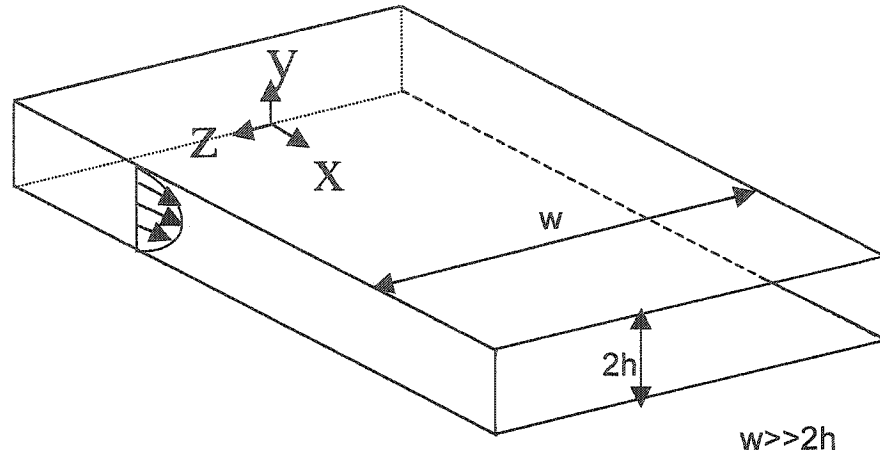


Figure 1.1 – Schematic of channel flow facility

The mean momentum equation for channel flow is:

$$0 = -\frac{1}{\rho} \frac{dP}{dx} - \frac{d \langle uv \rangle}{dy} + \nu \frac{d^2 U}{dy^2}. \quad (1.7)$$

Non-dimensionalization of this equation (where non-dimensional variables are formed from the density, ρ , the centerline velocity, U_c , and the channel half-width, h) results in:

$$0 = -\frac{d \hat{P}}{d \hat{x}} - \frac{d \langle \hat{u} \hat{v} \rangle}{d \hat{y}} + \frac{1}{Re} \frac{d^2 \hat{U}}{d \hat{y}^2}. \quad (1.8)$$

Equation 1.8 not only illustrates how the velocity field is dependent upon the Reynolds number ($Re = U_c h / \nu$), but also demonstrates how the governing equation is not closed. Describing this particular flow will therefore be non-trivial.

Of particular interest is the effect of the Reynolds number on the statistics of the velocity field (as the Reynolds number is one of the parameters in the current work). Also of interest are the various regions of the flow and their properties, proper non-dimensionalization schemes for the different regions, and a reliable benchmark with which to compare the present results for the purpose of verifying the flow field.

The existence of a wide range of scales proves to be a challenging aspect in finding universal non-dimensional flow parameters for wall-bounded flows like the one under consideration. Turbulent production occurs at the large scales (normally the characteristic scale of the flow, known as the integral scale). This large-scale turbulent energy is transferred down to the smallest scale (the Kolmogorov microscale) through a turbulent cascade, where it is dissipated (Tennekes and Lumley 1972). Experiments have verified that normalization of the mean velocity and wall-normal co-ordinate by inner variables (friction velocity, $u^* = (\tau_w/\rho)^{1/2}$ and kinematic viscosity) results in three distinct universal regions, independent of Reynolds number (Pope, 2000). These three regions are the viscous sublayer, the buffer region, and the log-law region (see Table 1.1). The non-dimensional velocity is $U^*(=U/u^*)$ and the non-dimensional distance is $y^+ (=yu^*/\nu)$ (where a superscript $+$ indicates non-dimensionalization by the inner variables). In the viscous sublayer, $U^+=y^+$. In the log-law region, $U^+=(1/\kappa) \ln(y^+) + A$, where κ (the Von Karman constant) and A are constants that vary slightly with Reynolds number (Shah, 1983).

Table 1.1: Different regions of flow field (Pope, 2000)

Region	Location	Defining Property
Viscous Sublayer	$y^+ < 5$	Reynolds shear is negligible
Buffer Layer	$5 < y^+ < 30$	Region between viscous sublayer and log-law region
Viscous Wall Region	$y^+ < 50$	Viscous contribution is significant
Log-law Region	$30 < y^+; y/h < 0.3$	Log-law holds
Overlap Region	$50 < y^+; y/h < 0.1$	Overlap region between sublayer and core region
Core Region	$50 < y^+$	Viscosity is negligible

The previous scaling method universally describes the mean velocity profile throughout all but the core region. No scaling method presently exists to universally describe the statistics of the velocity fluctuations, such as the RMS, skewness (defined in section 4.4), and kurtosis (defined in section 4.5.2). When normalized by inner variables, the RMS of the longitudinal velocity fluctuation (u_{RMS}) peaks at $y^+=15$, which corresponds to the maximum turbulence intensity ($=u_{RMS}/U$) and maximum turbulent kinetic energy. As Re_τ ($Re_\tau = u^*h/\nu$) is increased, the value of the peak u_{RMS} increases as well (Dinavahi et al., 1995). For v_{RMS} and w_{RMS} (normalized by inner variables), the location of the peak as well as the magnitude of the peak are both found to increase with increasing Re_τ (Dinavahi and al. 1995). Choosing a non-dimensional scheme to universally describe this simple flow proves to be a non-trivial task.

1.3.2 Turbulence Measurements

Hot-Wire Anemometry (HWA) and Cold-Wire Thermometry (CWT) are ideal methods for the measurement of the instantaneous velocity and temperature, respectively, in an air flow at a specified point as a function of time

(i.e. using an Eulerian frame of reference). They are both relatively low-cost, have a high frequency response, are compact, provide continuous signals, have good signal-to-noise-ratios, and have typical length scales on the order of the Kolmogorov scale for many flows (Bruun, 1995). In low speed flows of air (free of particles such as dust) at ambient temperature and turbulence intensities of less than 25%, HWA and CWT prove to be excellent measurement tools (Bruun, 1995).

A hot-wire is a fine cylindrical wire maintained at a constant temperature (or resistance) by Ohmic heating, and is used to measure components of the instantaneous velocity. The main source of heat transfer from the wire to the fluid is due to forced convection. Therefore the power input to the wire is a function of fluid velocity and temperature (Bruun, 1995). Due to the fact that a hot-wire is not a perfect cylinder in a cross flow, heat transfer occurs by conduction to the sensor's prongs, it has a finite length, it may have curvature, etc., each hot-wire is independently calibrated to account for these effects.

A cold-wire is a fine cylindrical wire used to measure the instantaneous temperature. By passing a low current through the cold-wire, as to not cause a significant temperature rise, the resistance of the cold-wire will change in a linear relationship with its temperature (Bruun, 1995).

In the present thesis, three probe configurations are employed, each with its unique method of calibration. To measure the instantaneous longitudinal velocity in an isothermal flow, a single-normal wire is used and calibrated by the procedure of Bruun (1995). To simultaneously measure the instantaneous

longitudinal and transverse velocities, two hot-wires are used in an X-configuration and are calibrated by the method of Browne et al. (1989). In the case of non-isothermal flows, an X-configuration of hot-wires is operated in conjunction with a cold-wire. This configuration is calibrated by the method of Lienhard (1988) in conjunction with that of Browne et al. (1989).

Particular considerations have to be taken into account while making measurements in this flow, due to the presence of the wall and also the anisotropy of the small scales. It has been shown that a wire must be less than twenty five viscous length units to make accurate near-wall measurements of RMS, skewness, and kurtosis of the velocity fluctuation (Khoo et al., 2000). In the region of $5 < y^+ < 35$, the small-scale measurements are dependent upon the wire length for wires ranging in length from two to eleven viscous lengths (Shah et al., 1983). Lastly, it should be noted, that in regions of increasing shear, the isotropy of the small scales is decreasing (Antonia et al., 1997). As many turbulent quantities are calculated from measured values, assuming small-scale isotropy, the validity of these measurements must be cautioned.

1.3.3 Scalar Dispersion in Isotropic Grid-Generated Turbulence

Isotropic grid-generated turbulence is the most fundamental turbulent flow and therefore the thermal plume from a concentrated line source has been studied in detail for this particular flow. Tennekes and Lumley (1972) show via an order of magnitude analysis that in isotropic grid-generated turbulence, the turbulent kinetic energy budget (equation 1-4) reduces to:

$$U_1 \frac{\partial}{\partial x_1} \left(\frac{3}{2} (u_{RMS})^2 \right) = -\varepsilon. \quad (1-9)$$

Taylor (1935), Uberoi and Corrsin (1953), and Townsend (1954) were among the first to carry out experiments studying the mean and fluctuating temperature field downstream of a line source in isotropic grid-generated turbulence.

Subsequent work has shown that the mean temperature profiles are Gaussian and that the development of the thermal plume in this flow can be divided into three stages: molecular diffusive, turbulent convective, and turbulent diffusive. In the molecular-diffusive range ($t \ll \kappa / \langle v^2 \rangle$), the growth of the mean temperature profile width, σ_{MEAN} , (where σ is the standard deviation of a Gaussian profile, which is a measure of its width) increases as $t^{1/2}$. The spreading of σ_{MEAN} is linear in time in the turbulent-convective range ($\kappa / \langle v^2 \rangle \ll t \ll t_L$, where t_L is the Lagrangian integral time-scale). In the final stage, where $t \gg t_L$, the spreading is proportional to $t^{1/2(2-n)}$, where n is the decay exponent of the velocity field and takes on values close to one (Stapountzis et al., 1986).

Though the mean temperature profiles are Gaussian, the RMS profiles of the temperature fluctuation are, however, non-Gaussian (Warhaft, 1984 and Stapountzis et al., 1986). Near the source, these RMS profiles exhibit double peaks, which result from the bulk flapping of the plume. These double peaks disappear further downstream at intermediate distances, reemerging far downstream in the turbulent diffusive region (Warhaft, 1984). The effect of downstream distance of the wire from the grid on the mean and RMS profiles has also been studied by Warhaft (1984). It was shown that the mean and RMS

profiles collapse when they are normalized by the turbulence integral scale at the source location.

The experimental results of scalar dispersion in this particular flow have also been numerically modeled by Stapountzis et al. (1986). This study allowed parameters such as viscosity and molecular diffusion to be varied. It was found that molecular diffusion and viscosity influence the development of the thermal plume in all stages, not just in the molecular-diffusive range. In all stages, these properties influenced both the magnitude and intensity of the temperature fluctuations. Where applicable, the results were found to be in agreement with those of Warhaft (1984).

Anand and Pope (1983) have also studied scalar dispersion in this flow. They developed a quantitative relation for all three stages of development of the thermal plume. This relation is based on a probability-density-function method.

1.3.4 Scalar Dispersion in Homogeneous Turbulent Shear Flow

A line source placed in a homogeneous turbulent shear flow isolates the effect of shear (an anisotropy) on the scalar dispersion. Detailed measurements of the resultant thermal plume in this flow field have been undertaken by Karnik and Tavoularis (1989) and Chung and Kyong. (1989). The mean and RMS temperature profiles have been documented in detail. Additionally, quantities such as velocity-temperature correlations, temperature PDFs, and joint velocity-temperature PDFs have been compiled to compare with and help develop theory, models, and numerical simulations.

The mean temperature profile is found to be Gaussian near the source, as in isotropic grid-generated turbulence. However, further downstream in the turbulent-diffusive range, the peak shifts toward the region of lower velocity (Karnik and Tavoularis, 1989). Karnik and Tavoularis (1989) found that the centerline mean temperature decay rate was similar to that of isotropic turbulence. However, the centerline RMS decayed at a higher rate. Chung and Kyong (1989) normalized the peak temperature rise, the mean dispersion of the temperature field, and the downstream distance by respective Lagrangian scales, finding the data to be well-correlated with dispersion from a line source in a turbulent boundary layer.

The re-emergence of double peaks in the RMS temperature profiles far downstream from the source is also observed in the measurements of Karnik and Tavoularis (1989), for which they have provided an explanation. When the width of the thermal plume far exceeds the integral length scale (i.e., the ratio of the large-scale eddy size to plume width approaches zero), the double peaks will re-emerge. In this region, temperature fluctuations are dominated by local production, since turbulent transport by the large-scale eddies is ineffective over this range. The local production term is proportional to the transverse mean temperature gradient (assuming the streamwise gradient to be negligible). Therefore, this term is zero at the mean temperature peaks and takes on the largest values in regions of highest temperature gradient. In bounded flows, such as channel flow, the size of both the large-scale eddies and the plume width limit themselves to the width of the flow. As the width of the plume approaches

the channel width, the ratio of large-scale eddies to plume width approaches its minimum value of unity. It is therefore expected that double peaks in the RMS profiles will not occur in bounded flows.

1.3.5 Experimental Study of Scalar Dispersion in Inhomogeneous Flow Fields

As mentioned, most "real world" engineering flows are inhomogeneous. Therefore studies of scalar dispersion in inhomogeneous flows such as jets, wakes, boundary layers, and mixing layers have been performed. Applications of scalar mixing and dispersion in these flows include combustion chambers, industrial mixers, and atmospheric dispersion. These flows are all inhomogeneous in at least two dimensions, therefore the effect of the inhomogeneity on the scalar dispersion is not isolated.

The thermal plume behind a line source in a turbulent boundary layer has received significant attention. Over a narrow range in the streamwise direction (such that this direction can be effectively considered homogeneous), boundary layer flow and fully developed channel flow are similar and therefore these experiments can serve to validate the data contained within this thesis. However, the (two-sided) bounded nature of channel flow is fundamentally different than the (one-sided) bounded nature of the flow in a boundary layer. If the scalar is injected between the wall and the end of the log-law region, the scalar plume will be similar until it extends to end of the log-law region. Once the scalar plume extends beyond this region, it will be completely different due to the aforementioned differences of the two flow fields.

The mean temperature profile downstream of a line source placed in a boundary layer was studied by Shlien and Corrsin (1976). They found that the normalized mean temperature profile approaches an asymptotic form, independent of source position from the wall, and that an appropriately defined turbulent Prandtl number was approximately unity. Paranthoen et al. (1988) measured the mean and fluctuating temperature field downstream of a line source placed in a turbulent boundary layer and in a plane jet. They deduced a rescaling scheme based on the temporal integral Lagrangian scale of the vertical velocity fluctuation. This scheme satisfactorily collapsed the mean profiles onto a simple curve. Further measurements of scalar dispersion from a line source in a boundary layer were undertaken by Kabiri et al. (1998) to assess various first and second-order closure models.

Although a more complicated dispersion problem, the dispersion from a point source located in a turbulent boundary layer leads to more practical applications (e.g. dispersion from a smoke-stack). Measurements of the variance, intermittency, peak concentration values, PDFs, and spectra of the scalar have been made for a ground level and an elevated point source located in a turbulent boundary layer (Fackrell and Robins, 1982). This study examined in detail the balance of terms for the temperature fluctuations, illustrating that the production term is dominant in the region near the source. As the fluctuation decays, the decay is in accordance with the balance of advection and dissipation. Bara et al. (1992) verified a numerical model (i.e., an isotropic meandering plume model combined with a clipped normal concentration probability distribution) with

dispersion measurements of the vertical and crosswind (scalar) profiles of mean, variance, intermittency, and conditional intensity of non-zero fluctuations for a ground level point source located in a simulated neutrally stable atmospheric boundary layer.

Additional work involving the experimental study of scalar dispersion in inhomogeneous flow fields have been performed by Raupach and Legg (1983), Legg et al. (1986), Incropera et al. (1986), Veeravalli and Warhaft (1990), Tong and Warhaft (1995), and Vincont et al. (2000).

Lastly, it should be noted that the mean concentration of scalar dispersion in a long pipe can be accurately predicted using Taylor shear flow dispersion theory (Taylor, 1953). This method can be extended to other turbulent shear flows, however is valid only for very large diffusion times (i.e., times greater than the Lagrangian integral time scale). Since the present work concentrates on the early stages of diffusion (i.e., the turbulent convective stage), this method is not applicable to the results presented herein.

1.3.6 Role of Numerical Simulation in the Study of Scalar Dispersion

Recent advances in computing power and storage have allowed for turbulent flows and scalar dispersion to be numerically studied via Direct Numerical Simulation (DNS). Although DNS of practical engineering flows is still limited by the massive amounts of storage and processing power needed, simple flows, such as channel flow at a low Reynolds number, can be efficiently studied. Virtual experiments permit changes that are not feasible experimentally, such as easy modification of fluid properties, boundary conditions, and experimental

parameters. In addition, they permit the quantification of any variable of interest. DNS is an attractive technique for the study of turbulence, however will still be hampered by computing limitations for the near future.

Scalar dispersion in low Reynolds number channel flow has been simulated by Lyons et al. (1991), Papavassiliou and Hanratty (1997), and Na and Hanratty (2000). Kontomaris and Hanratty (1994) studied the effects of molecular diffusivity on a point source located at the centerline of a turbulent channel flow. Other numerical simulations of dispersion in inhomogeneous turbulent flows have been performed by Bernard and Rovelstad (1994) and Iliopoulos and Hanratty (1999).

1.4 Thesis Overview

The previous sections have provided an overview and motivation of this particular study as well as a summary of the relevant literature. In this section, the remainder of the thesis is described.

First, a detailed description of the channel flow facility is given and the measurement techniques are presented. The measurement of turbulent quantities focuses on the calibration procedures of the HWA and the CWT, resolution of the probes, analogue to digital conversion, and the convergence of statistical quantities.

Next, the experimental conditions are verified. These conditions are that: the flow field is fully developed channel flow, the scalar is passive, the walls are adiabatic, the temperature field is independent of the source size, and the

temperature field is 2-D. Various turbulent flow properties are also tabulated for the two Reynolds numbers under consideration.

Results of downstream dispersion of a passive scalar from a concentrated source are then presented. The distance of the source from the wall and the Reynolds number of the flow are the varied parameters. Detailed statistical measurements of the thermal plume are taken using hot-wire anemometry and cold-wire thermometry. The measured statistical quantities of the passive scalar are: mean profiles, Root-Mean-Square (RMS) profiles, skewness profiles, Probability Density Functions (PDFs), and velocity-temperature correlations.

Finally, a complete database of results is compiled to compare with and influence the development of numerical simulations and theoretical models.

As the results are presented, they will also be compared to those of scalar dispersion in isotropic grid-generated turbulence and homogeneous turbulent shear flow, where significant progress has been made, both theoretically and experimentally.

Chapter 2

Experimental Facility and Measurement Techniques

2.1 Apparatus

2.2.1 Channel Facility

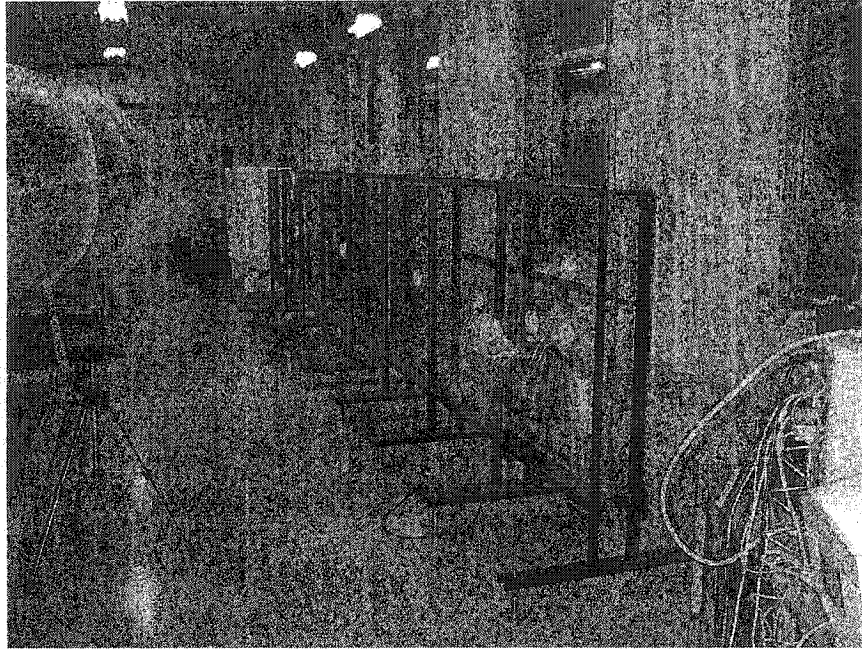


Figure 2.1 – Channel flow facility

The open-circuit, high-aspect-ratio channel was designed specifically for scalar mixing experiments. For a detailed description of the channel design, construction, and related references, see McLeod (2000). The dimensions of the channel cross-section are 1.1 m (height) x 0.06 m (width). Refer to figure 2.1 for the orientation of the channel. These dimensions provide an aspect ratio of 18, which ensures that away from the top and bottom walls the flow field will be two-dimensional.

The air flow is supplied by a centrifugal blower (Hudson Buffalo ACL size 330 cl2), capable of efficiently operating over the range of specified velocities. The blower is powered by a 7.5 horsepower electric motor, which is mounted on high-density rubber footpads to damp vibrations. Precise control of the motor rpm (and hence flow rate) is accomplished by an ABB ACS 600 controller. A filter box located at the blower intake prevents particles greater than 3 μm from entering the test-section and potentially interfering with the measurement instrumentation. A perforated plate located at the blower exit serves as a preliminary flow-conditioning measure. In order to minimize the transmission of blower vibrations to the flow conditioner, a flexible rubber coupling joins the blower output to the entrance of the flow conditioner.

The flow conditioner consists of a wide-angle diffuser, a settling chamber, and a contraction. The purpose of the wide-angle diffuser is to reduce the speed of the flow before it enters the settling chamber. This allows the flow to remain in the settling chamber for a longer period of time, and also reduces the local Reynolds number of the flow through the screens and the honeycomb. The area ratio of the diffuser is 3.55, which is a design constraint established by the fixed dimensions of the blower exit area, contraction ratio, and cross-sectional channel dimensions. To minimize the diffuser length, a wall-angle of 45 degrees is chosen. This large wall-angle normally results in a strong adverse pressure gradient, which would result in flow separation. However, separation in the diffuser is inhibited by the use of four appropriately located screens, which

balance the pressure rise (due to the decrease in velocity) with the pressure drop (resulting from the screens).

The settling chamber eliminates any transverse velocity fluctuations and swirl. The cross-sectional area of the settling chamber is constant. An aluminum honeycomb section and six screens are appropriately located to maximize the efficiency of the settling chamber. The honeycomb section is 76 mm long and the opposing hexagonal cell walls are 6.35 mm apart, providing the desired length to diameter ratio and cell density. The mesh size of the screens is chosen to be 1 mm, based on the necessary honeycomb cell diameter to screen mesh size ratio.

The flow conditioner height is the same as the channel (as intended), and therefore the contraction is 2-D. A contraction ratio of eight is chosen, based on recommended design criteria. To satisfy all the mathematical properties of the constraints, the contraction shape is based on a fifth-order polynomial. After exiting the contraction, the flow enters the channel as a uniform, low-turbulence-intensity (0.25%) velocity field.

The channel dimensions are 8m x 1.1m x 0.06m. The side-walls of the channel each consist of 8 mated one-inch thick Plexiglas sheets of dimensions 1.1 m x 1 m. The top and bottom walls each consist of four Plexiglas caps of dimensions 0.06 m x 2 m. To ensure that the joints of the side-wall sheets do not interfere with the flow field, "biscuits" and adjustable tightening screws are used along the joints in the spanwise direction to keep the height between mating ridges less than 5 viscous lengths. This height is dependent upon the flow

Reynolds number (see section 3.1.1). This maximum allowable height is within the limits of which the channel walls can be considered to be perfectly smooth (Tennekes and Lumley, 1972).

To establish fully developed flow as early on as possible, boundary layer tripping rods are placed near the entrance of the channel. Along each wall in the spanwise direction, a 3.2 mm diameter rod is located 3 mm from the wall. These rods are located 60 mm downstream of the entrance, to allow for some boundary layer growth before it is tripped. To maintain fully developed flow throughout the test section, a honeycomb (the same type as used in the settling chamber) is located at the channel exit.

The test section extends from 7.00 to 7.67 m downstream of the channel entrance. Custom machined ports are located at 7.33 m (Port 8-1) and 7.67 m (Port 8-2) from the channel entrance along the spanwise centerline, where all the measurements in this work are taken. The thermal plume and flow field were scanned by a linear traversing mechanism driven by a precision stepping motor (0.01mm per step).

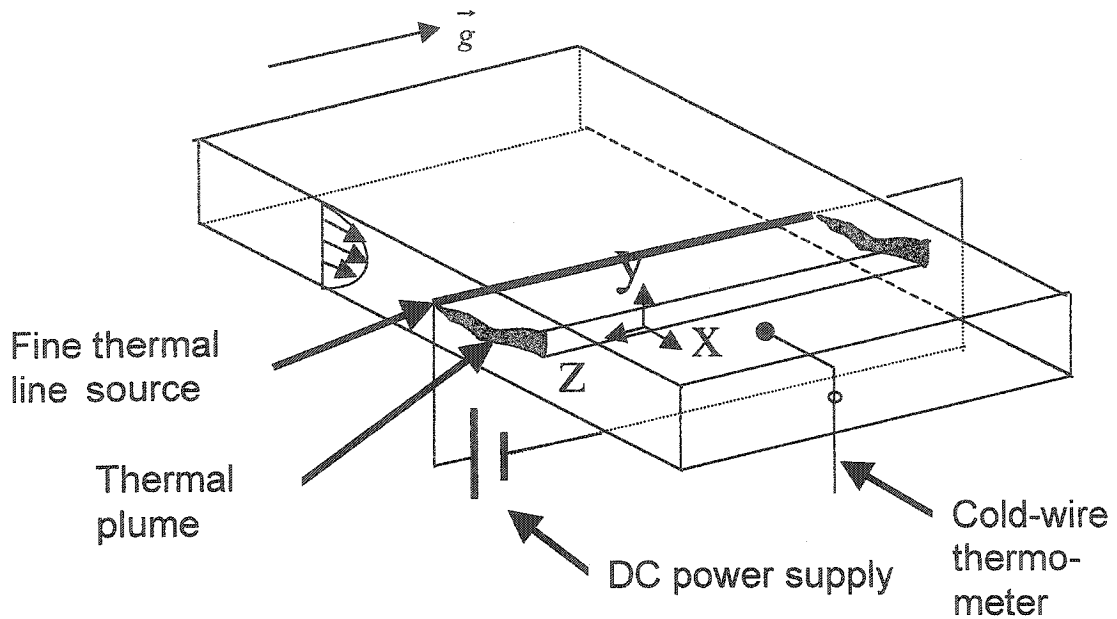


Figure 2.2 – Orientation of coordinate system

Figure 2.2 illustrates the orientation of the coordinate system used herein. The y-axis is situated in the wall-normal direction and originates at the wall. The x-axis is parallel to the streamwise direction and is taken to be zero at the location of the source, which is always in the fully developed section of the channel. Therefore, the x-coordinate is a measure of downstream distance from the source and is not an absolute measure of channel location. The z-axis is parallel to the spanwise direction and originates at the channel centerline. Gravitational acceleration is oriented along the z-axis, as can be seen in figure 2.1.

2.1.2 Injection of the Scalar

Injection of the scalar is accomplished by means of a fine Nichrome-wire line source, threaded in the spanwise direction through small holes located on the top and bottom caps. The source is kept taught by hanging a weight off of it. For measurements close to the source ($x/h \leq 10.8$), the source diameter is 0.127 mm. Further downstream, a greater power input is required to produce an acceptable signal to noise ratio. Therefore, a source diameter of 0.254 mm is employed for these locations. The source is heated via a DC power supply, which provides 45 W/m and 100 W/m for the small and large diameter source, respectively. Port 8-1 is used in conjunction with an appropriately located source (diameter = 0.127mm) for measurements at $x/h = 4, 7.4,$ and 10.8. Port 8-2 is used in conjunction with an appropriately located source (diameter = 0.254mm) for measurements at $x/h = 15.2, 18.6,$ and 22. The effect of the source on the flow field is discussed in section 3.1.2.

2.2 Measurement Techniques

This section discusses the methods and calibration procedures used to measure the velocity and thermal fields. Attention is focused on the calibration procedures of HWA and CWT, temporal and spatial resolution of the probes, analogue to digital conversion, the sampling frequency and number of points taken to ensure the convergence of statistical quantities.

It should be noted that all the calibration procedures and associated curve fits are deduced from idealized physical models. While this theory does not

provide the exact calibration constants because of unaccounted secondary effects, the form of the calibrations on the dependent variable is obtained from first-order models.

2.2.1 Calibration Procedure of a Cold-Wire

A platinum cold-wire of diameter 0.63 μm is used to directly measure the instantaneous fluid temperature in conjunction with a TSI 1240 single-wire probe. The low thermal inertia of the cold-wire allows a rapid response to changes in fluid temperature (see section 2.2.4). Since the cold-wire resistance is a linear function of temperature, passing a low (constant) current through this wire results in an output voltage that is linear in temperature:

$$T = CE_T + D. \quad (2-1)$$

This constant current is supplied to the wire by a Constant Current Anemometer circuit built at Laval University, Ste. Foy, Quebec.

Ohmic losses result in heat transfer from the cold-wire to the flow, slightly elevating the cold-wire temperature above that of the flow. This heat transfer is dominated by convection cooling, making the rise in temperature a function of the fluid velocity. Minimization of this heat transfer is achieved by passing the smallest possible current through the cold-wire, allowing for the temperature rise to be neglected. Thus the output voltage is only a function of the fluid temperature. There is a constant trade off between the strength of the cold-wire signal and the minimization of the effect of velocity on cold-wire output. A current

of 0.1 mA results in a balance between the competing effects of the signal to noise ratio and velocity sensitivity of the wire.

The cold-wire calibration takes place in a TSI calibration jet (TSI 1127). The air jet is maintained at a constant velocity (of the order of that experienced by the wire in the experiment) as the temperature of the air jet is varied. The air jet is heated by electric coils located between the air supply and the calibrator. After the desired maximum temperature is reached, the power to the coils is cut off and the jet is allowed to cool. A reference thermocouple records the temperature as the output voltage is recorded. An example cold-wire calibration is shown in figure 2.3.

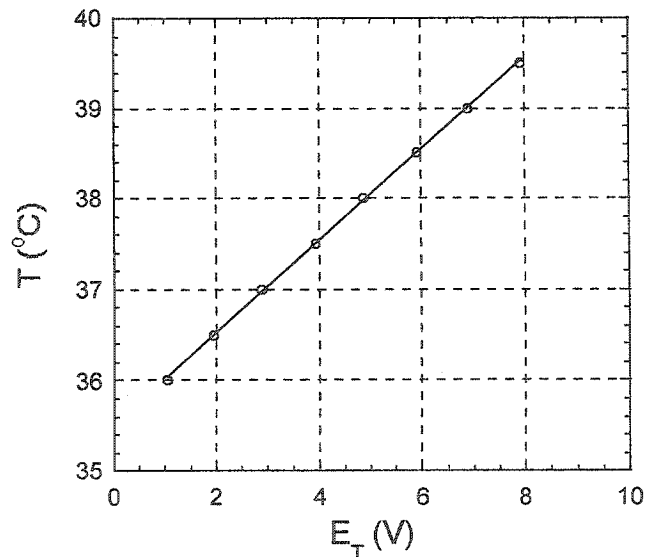


Figure 2.3 – Cold-wire calibration curve

2.2.2 Calibration Procedure of Hot-Wires for an Isothermal Flow

For measurements of (solely) the longitudinal component in an isothermal flow, a single-normal, tungsten hot-wire probe of 3 μm diameter is selected. A TSI boundary layer probe (TSI 1218) is used in conjunction with a TSI IFA 300 Constant Temperature Anemometer. The probe is oriented normal to the mean flow direction and parallel to the spanwise direction. The probe is calibrated in the calibration jet over the complete range of velocities encountered in the experiment. The probe operating temperature (and therefore resistance) was determined by selecting an overheat ratio of 1.8, which corresponds to a temperature of approximately 250°C (Brunn, 1995). Modifying King's Law ($E^2 = \bar{A} + \bar{B} U^{0.5}$), equation 2-2 was used to fit the calibration data (Brunn, 1995), which relates the output voltage of a hot-wire to the instantaneous velocity of the flow:

$$E^2 = \bar{A} + \bar{B} U^n. \quad (2-2)$$

The constants were obtained using a least-squares curve fit (see figure 2.4).

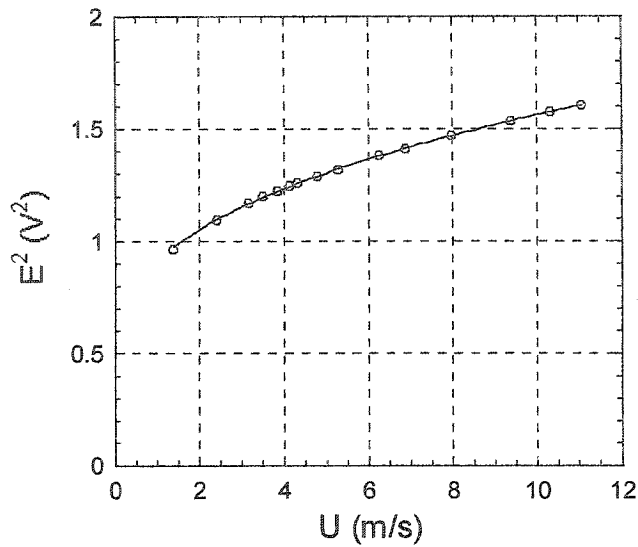


Figure 2-4 – Single-normal-wire calibration curve

Typically, the calibration jet temperature differed from that of the experiment. To compensate for this temperature change, the operating temperature of the hot-wire was chosen such that the temperature difference between the hot-wire and the flow was the same in both the calibration and the experiment (Jorgensen, 2002). The convective heat transfer coefficient is a function of both fluid velocity and temperature. Assuming that this small change in wire operating temperature does not change the convective heat transfer coefficient dependence on velocity, the constants of equation 2-2 will hold from calibration to experiment, using this procedure. At the start of both the experiment and the calibration, the wire resistance is measured and then the operating resistance (or temperature) is set using an overheat ratio of 1.8. The dependence of resistance on temperature is linear over this range, therefore the

use of a constant overheat ratio suffices for this task. Brunn (1995) mentions that this method may overcompensate for the ambient temperature drift.

2.2.3 Calibration Procedure of Hot-Wires for Non-isothermal Flows

The heat transfer from a hot-wire to the flow is dependent on the instantaneous value of the fluid velocity and temperature. Measurement of the resultant thermal plume and associated velocity-temperature correlations require that the hot-wire calibration account for not only the fluctuating velocity, but also the fluctuating temperature field. An assembly of a cold-wire with two hot-wires in an X-configuration (TSI 1241 probe) is used to simultaneously measure the temperature and (two components of) velocity.

Direct measurement of the temperature using a cold-wire allows for the measurement of the velocity field given an appropriately calibrated hot-wire. To measure both the u and v components of the fluctuation velocity, two hot-wires are used in an X-configuration (to be discussed). Alignment of the probe with the mean flow, which occurs in the x -direction and is denoted U , results in approximately a 45° angle between the mean flow and each hot-wire. Both wires lie in the x - y plane. When an inclined wire is calibrated using the procedure of 2.2.2, equation 2-2, which assumes that the flow is normal to the wire, fits the data. Although the angle of the wire could be measured, the three dimensional curvature and other secondary effects require that an effective angle between the mean flow and hot-wire relate U to an equivalent normal velocity, U_N . The equivalent normal velocity, U_N , is the magnitude of the velocity normal to the hot-

wire that results in the same output voltage as a velocity, U . This effective angle is found using the procedure of Browne et al. (1989). The relationship between U and U_N is:

$$Uf(\theta) = U_N \quad (2-3)$$

where θ is the effective angle. To account for longitudinal cooling, Hinze (1975) recommends:

$$f(\theta) = (\sin^2 \theta + k^2 \cos^2 \theta)^{1/2} \quad (2-4)$$

where k^2 varies between 0.01 and 0.04. A standard value of 0.03 is chosen for the measurements contained herein.

The previous relationships can be used to relate an instantaneous velocity, \vec{V} , to the U and V components, using two inclined hot-wires. Although \vec{V} will in general not lie in the x - y plane, Perry (1982) shows that an inclined wire in the x - y plane is not sensitive to a velocity fluctuation in the z -direction (for a low turbulence intensity flow). From equation 2-2, the output voltage of the instantaneous velocity can be related to an equivalent mean velocity, U , that would result in the same output voltage of the inclined hot-wire. A combination of two inclined hot-wires that each experience the same velocity of magnitude S at an angle β to the x -axis, results in the following relationship:

$$U_1 f(\theta_1) = S f(\theta_1 + \beta) \quad (2-5)$$

$$U_2 f(\theta_2) = S f(\theta_2 + \beta) \quad (2-6)$$

where the subscripts denote the two different hot-wires.

This section has explained how the output voltage of two hot-wires in an X -configuration can be employed to measure two components of a fluctuating

velocity field in an isothermal flow. It is now necessary to account for variable temperature.

Lienhard (1988) shows that both \bar{A} and \bar{B} can be related to the instantaneous temperature:

$$\bar{A} = AT_f^{0.84}(T_{wa} - T) \quad (2-7)$$

$$\bar{B} = B(T_{wb} - T). \quad (2-8)$$

Here \bar{A} and \bar{B} are slightly modified from Lienhard (1988), where $T_{wa} = T_{wb}$:

The calibration of the X-probe takes place in the calibration jet, with the probe aligned in the direction of the mean flow. A large reservoir of air is first heated. As it slowly cools, five different U versus E calibrations are performed at five distinct temperatures. Equation 2-2 is used to fit the data for each distinct temperature using a least-squares method. An iterative method is used to determine the constant n, which best fits all the five E versus T curves for the two channels. Lienhard (1988) recommends $n=0.45$, however the iterative method proves to better fit the curves. The previous steps result in a data set of \bar{A} and \bar{B} versus temperature. A least-squares curve fit is used to find the constants A, B, T_{wa} , and T_{wb} , for each hot-wire (see figure 2.5). During the calibration, the effective angle is also calculated for the two lowest temperatures, which approach the temperature range encountered in the experiment. An average effective angle is chosen.

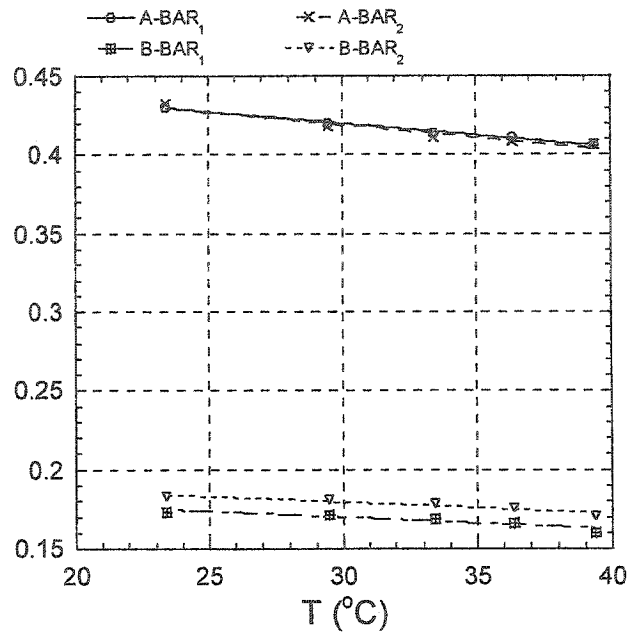


Figure 2.5 – Calibration curve for non-isothermal flows

Once the calibration constants are known, the following steps illustrate how the two hot-wire signals and the one cold-wire signal are converted to the variables of interest.

1. The measured value of E_T determines the temperature from equation 2-1.
2. The temperature permits the calculation of \bar{A} and \bar{B} using equation 2-7 and 2-8.
3. The measured values of E_1 and E_2 determine U_1 and U_2 using equation 2-2.
4. S and β can now be calculated using equations 2-5 and 2-6, and a Newton-Raphson method, which give the instantaneous longitudinal and transverse components of velocity, U and V .

2.2.4 Spatial and Temporal Probe Resolution

Both the velocity and temperature field of a turbulent flow consist of a wide range of scales and frequencies, which must all be measured. As the turbulent eddies are convected past the measurement instruments, small length-scales correspond to rapid time-scales. It is necessary that the time constants of the probes be smaller than the fastest time-scales of the measured quantities and that the length of the probes be smaller than the smallest length scales in order to resolve the small scales.

Lemay (2001) shows that a 0.63 μm Pt-10%Rh cold-wire is able to resolve frequencies up to 7.3 kHz and 8.7 kHz for flows of 5 m/s and 10 m/s, respectively. The frequencies encountered in the experiment are just within the limit of those for the probe. HWA has a much greater frequency response (on the order of 100 kHz) than CWT. The TSI 300 system with a 3.8 μm diameter probe has a frequency response of 260 kHz in a jet of 100 m/s and encountered frequencies are therefore within the limits of the probe resolution.

The smallest length scale of the turbulent velocity fluctuations is the Kolmogorov scale, which is defined as:

$$\eta \equiv (v^3 / \varepsilon)^{\frac{1}{4}}. \quad (2-9)$$

Molecular diffusion is responsible for the dissipation of both small-scale temperature and velocity fluctuations. Since the Prandtl number of air is of the order one, the smallest temperature fluctuation will be of similar size as the smallest velocity fluctuation. To resolve these small scales, it is necessary that

the length of both the hot-wire and cold-wire be comparable to the smallest scales. The active length of the hot-wire and cold-wire are each etched to a length of approximately 0.5 mm, which corresponds to an L/D ratio of 166 and 800 respectively. As shown in Chapter 3, the measured Kolmogorov scales for the low and high Re are 0.2 mm and 0.1 mm, respectively. Since the probe lengths are larger than the small scales, it is necessary to compensate for small-scale measurements. This will be discussed in section 3.2.

The corresponding viscous-lengths of the wires are 9 and 17 for the low and high Reynolds number (see section 3.1), respectively. As discussed in section 1.3, these viscous-lengths are appropriate for near wall measurements of large-scale quantities, however will result in wire dependence for small-scale quantities.

2.2.5 Analogue to Digital Conversion

The analogue signals were converted to digital data using a National Instruments PCI E Series Analogue to Digital Conversion (A/D) Board. Custom-made data acquisition software and real-time spectrum analyzers were programmed with LabVIEW. The total signal was directly input to the A/D board, where the fluctuating quantity of the signal was first high-pass filtered, then a sufficient gain was applied, and was finally low-pass filtered before being digitized.

The A/D board is a 12-bit board, which divides the sampling window into 2^{12} values. Each sample is truncated to the closest value. When separate

signals are simultaneously sampled, the A/D board requires that the sampling window for each channel be the same. To avoid both clipping and truncation error, the gain of each signal is set such that the signal occupies approximately 80% of the sampling window (typically +/- 5 volts).

Although each sample point is considered an exact point in time, the sample is an average over a finite time span. Each signal is averaged over a period of 4 μ s, which corresponds to the maximum A/D board sampling frequency of 250 kHz. It should also be noted that simultaneous sampling is not feasible with this A/D board. The A/D board samples each of the three signals in sequence for a total sampling period of 12 μ s, which is considered to be one point in time. The largest frequency of any of the measurements taken in the results section is 12 khz. The sampling time of 12 μ s corresponds to 83 khz, and can therefore be considered a specific point in time for the measurements herein.

The digital values of the voltages are converted to the variables of interest (and related statistical quantities) using custom made FORTRAN 90 software developed at Cornell University, Ithaca, NY and McGill University, Montreal, QC.

2.2.6 Statistical Convergence of Data

Four separate types of data sets are used to convert the measured signals into the variables of interest. These data sets consist of mean value, higher-order moments, PDF, and spectral data sets. Although each variable is a function of time, each variable is statistically stationary implying that measured statistical values converge. The mean values are sampled directly from the

output signal of the probe. The measured fluctuating quantities are high-pass and low-pass filtered before the signal is recorded, subtracting out the mean signal and high frequency noise. This section discusses the methods used to choose the sampling frequency and number of data points, which provide converged quantities.

The mean values of the output voltages were measured by integrating the unfiltered output voltages over a specific time period. This integrated value was then divided by the time period. The time period was heuristically chosen at the start of the experiment and periodically verified throughout. A sampling period of 15 seconds was found to agree to within three decimal places compared to a sampling period of 30 seconds. This convergence of three decimal places for the output signal falls within the limit of experimental error for all the measured variables (a typical convergence in temperature signal would be 0.0005°C).

The higher-order moments presented in the results section consist of measured moments up to the fourth order. The moment data sets are used for computing the moments of a single variable and also for correlations of two different variables. For this data set, 10 blocks of data are taken, each block containing 4096 points sampled at 200 Hz. The chosen sampling frequency corresponds to the order of the integral time scale for all the measured quantities, so that all the points are statistically independent of each other (Tennekes and Lumley, 1972). The integral time scale was determined from the peak of the real-time spectrum multiplied by the frequency (Lumley and Panofsky, 1964).

Table 2.1 illustrates the typical convergence of the moments up to the fourth order, where one block is 4096 data points.

Table 2.1: Moment convergence table

# blocks	θ_{RMS}	S(θ)	K(θ)
1	0.120	-0.473	3.520
9	0.121	-0.479	3.456
10	0.121	-0.487	3.477

The PDF is, in principle, a complete description of all the moments. Hence convergence of the PDF is rather slow in comparison to that of the lower-order moments. Equation 2-10 shows the relationship between the nth order moment of a variable a and its PDF,

$$\langle a^n \rangle = \int_{-\infty}^{\infty} a^n P(a) da. \quad (2-10)$$

PDFs are sampled for 100 blocks, each block containing 4096 points sampled at 200 Hz. The sampling frequency is once again chosen such that all the points are statistically independent of each other. Figure 2.6 illustrates the convergence of a PDF for a temperature fluctuation.

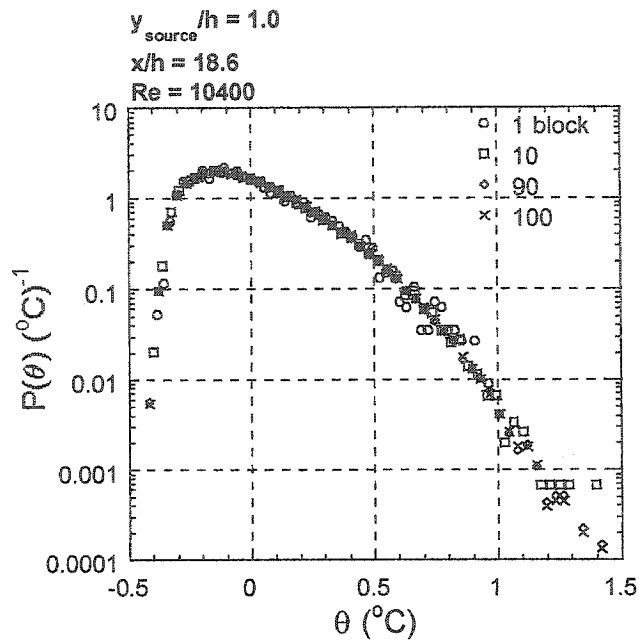


Figure 2.6 – PDF convergence

Spectral data sets are used for computing spectra and also for all quantities that require a time derivative, such as the dissipation. One hundred blocks of data, each containing 4096 points sampled at twice the Kolmogorov frequency, are recorded for spectral data sets. This sampling frequency is chosen in order to avoid aliasing. The levels of convergence of the spectra, not shown here, is similar to that of the PDFs.

Chapter 3

Experimental Conditions and Flow Properties

3.1 Verification of the Experimental Conditions

To meet the objectives of this thesis, the experiment should meet the following conditions:

1. The flow should be fully developed (1-D) channel flow.
2. The injected scalar should be passive.
3. The walls should be adiabatic.
4. The temperature field should be independent of the source diameter.
5. The temperature field should be two-dimensional (independent of the z-direction).

This chapter examines the experimental conditions and determines whether or not they meet the desired criteria.

3.1.1 Flow Verification

This section verifies that fully developed channel flow has been established in the test section for both the low and high Re. McLeod (2000) has established that the pressure gradient is constant, which is a rudimentary test to establish fully developed flow (Shah et al., 1983). It will be shown that the mean and RMS velocity profiles at both measurement stations (Port 8-1 and 8-2) collapse, as do the higher-order moments along the channel centerline. Though

not explicitly a test of fully developed flow, this data will then be compared to the log-law and shown to be in good agreement.

3.1.1.1 Low Reynolds Number

Results are presented for two Reynolds numbers, where the lower one is 10400. Figures 3.1 and 3.2 show the mean and RMS velocity profiles at Port 8-1 and Port 8-2 (located 7.33 m and 7.67 m downstream of the channel entrance, respectively). The maximum difference is 1.7% for the mean profile and 3.2% for the RMS profile. (Note that data cannot be obtained for $y > 50$ mm due to interference of the probes with the channel wall.) Table 3.1 compares the higher-order moments at the channel centerline, which is a more rigorous test of fully developed flow (Shah et al., 1983). The difference in skewness at the centerline from Port 8-1 to Port 8-2 is 6.5%. This (relatively) larger error results from the fact that the value of the skewness approaches zero. (As the value tends to zero, any finite error will result in a continuously larger percentage error.) The difference in the kurtosis is 1.46%. This data confirms that fully developed flow has been achieved in the test section at the low Re.

Figure 3.3 compares the experimental data to the log-law (discussed in section 1.3.1) and is shown to be in good agreement. The log-law is valid in the range where $y^+ > 30$ and $y/h < 0.3$. The friction velocity, u^* , is determined from the measured pressure drop, dP/dx (Tennekes and Lumley, 1972):

$$u^* = \sqrt{\frac{dP}{dx} \frac{h}{\rho}} \quad (3-1)$$

The friction velocity is found to be 0.26 m/s, which results in a viscous length-scale (ν/u^*) of the flow of 5.77×10^{-2} mm.

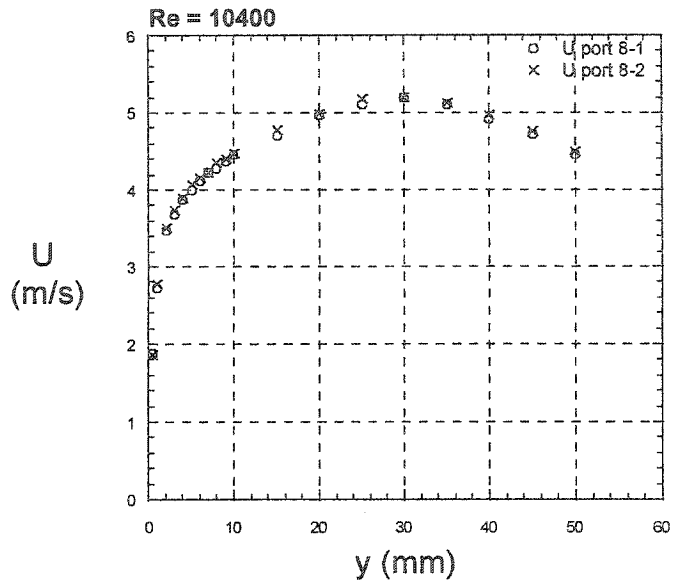


Figure 3.1 – Low Re mean velocity profiles

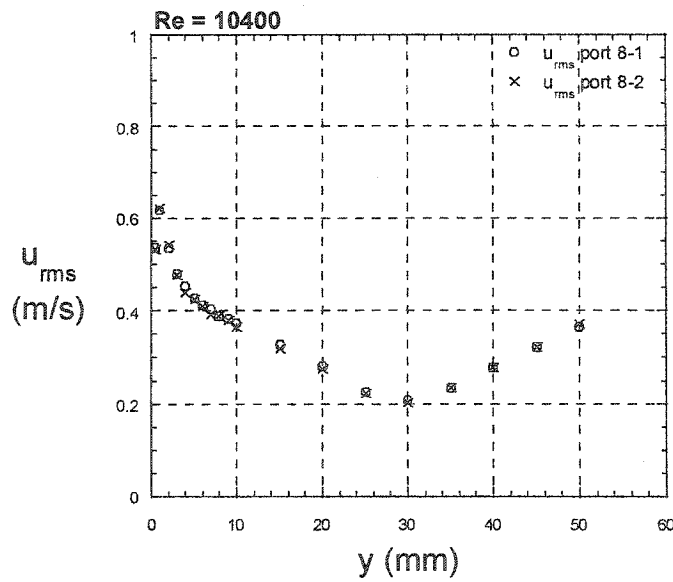


Figure 3.2 – Low Re u_{RMS} profiles

	Port 8-1	Port 8-2	% Difference
S(u)	-0.45	-0.48	6.45
K(u)	3.45	3.40	1.46

Table 3.1: Longitudinal variation of higher-order moments along the channel centerline for the low Re case

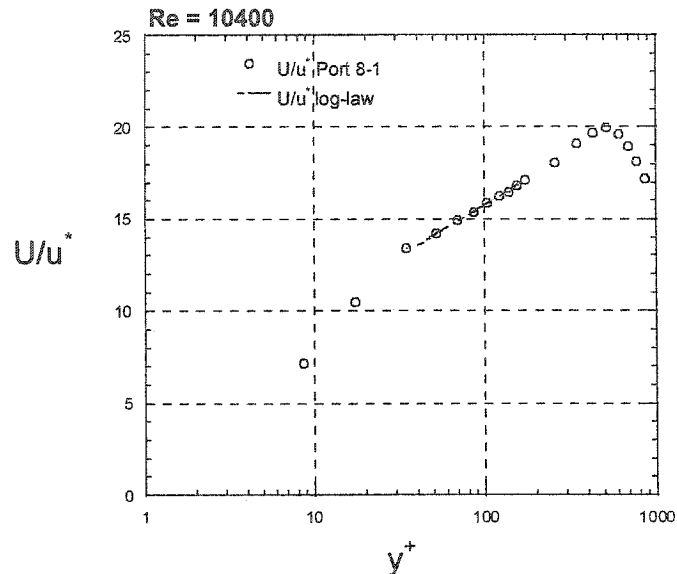


Figure 3.3 – Low Re log-law comparison

3.1.1.2 High Reynolds Number

The high Reynolds number is 22800. Figures 3.4 and 3.5 show the collapse of the mean and RMS velocity profiles at Port 8-1 and Port 8-2. The maximum difference is 0.9% for the mean profile and 3.7% for the RMS profile. The difference in skewness at the centerline from Port 8-1 to Port 8-2 is 0% and 0.3% for the kurtosis. This data verifies that fully developed flow has been achieved in the test section at the high Reynolds number.

Figure 3.6 compares the experimental data to the log-law, which are in good agreement. The friction velocity is found to be 0.54 m/s, which implies that the viscous length-scale (ν/u^*) of this flow is 2.88×10^{-2} mm.

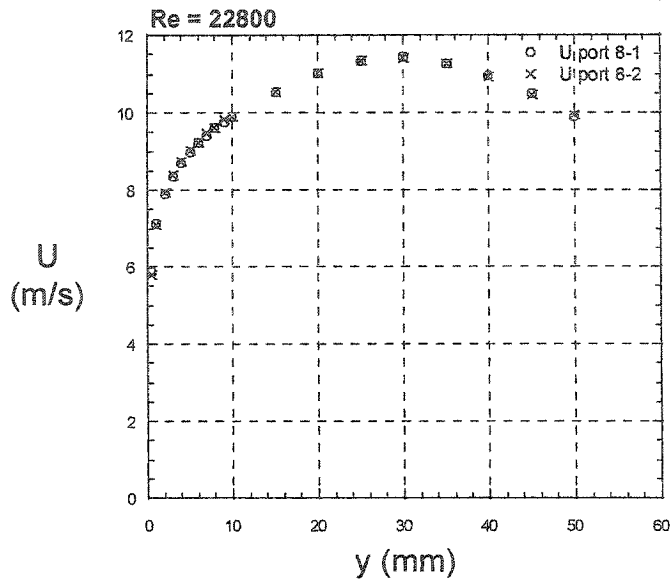


Figure 3.4 – High Re mean velocity profiles

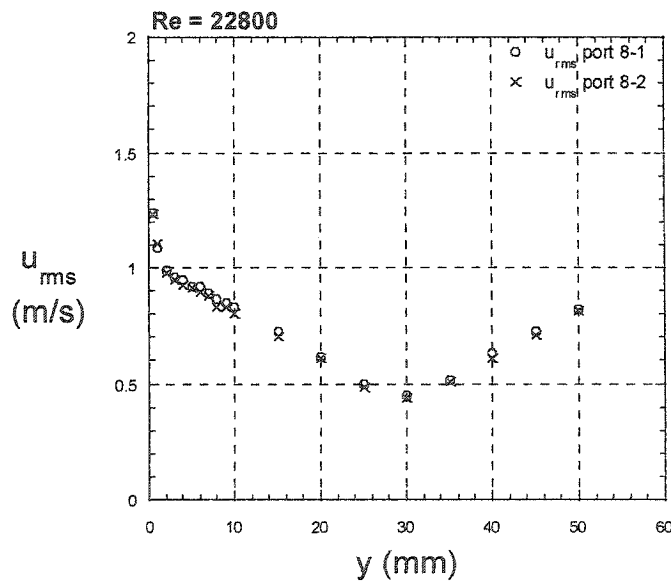


Figure 3.5 – High Re u_{RMS} profiles

	Port 8-1	Port 8-2	% Difference
Skewness	-0.52	-0.52	0.00
Kurtosis	3.50	3.51	0.29

Table 3.2: Longitudinal variation of higher-order moments along the channel centerline for the high Re case

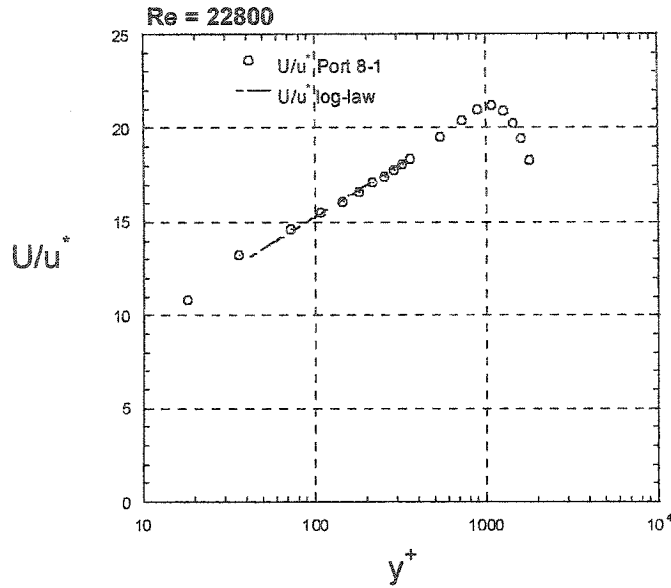


Figure 3.6 – High Re log-law comparison

3.1.2 Passivity of the Scalar

Injection of the scalar has two effects on the flow field. One is the obstruction caused by the physical presence of the line source. The second is the possible presence of buoyancy effects.

Two different line source diameters are used: 0.127 mm and 0.254 mm. The larger source is used for measurements where $x/h \geq 15.2$, and therefore where a higher power input is required to produce an acceptable signal to noise ratio far downstream. For the high Re flow, the source Reynolds number ($Re_{\text{source-cold}}$), based on wire diameter (d_{source}) and kinematic viscosity of air at the ambient temperature, is 97 and 193 for the small and large diameter sources, respectively. These are above the critical value of 40, where vortex shedding begins to occur (Blevins, 1990).

However, the elevated source temperature heats the fluid in the vicinity of the source, which consequently raises the viscosity of the fluid and in turn lowers the Reynolds number. Basing the viscosity on the film temperature, $T_{\text{film}} = \frac{1}{2}(T_{\text{source}} + T_{\infty})$, a source Reynolds number can be defined as: $Re_{\text{source}} = U d_{\text{source}} / \nu_{\text{film}}$. The source temperature can be calculated by estimating the average convection heat transfer coefficient using the Zhukauskas correlation for a cylinder in a cross-flow:

$$Nu_d = \frac{h_{AV} d_{\text{source}}}{k_{\text{air}}} = 0.51 Re_{\text{source-cold}}^{0.5} Pr^{0.37} \left(\frac{Pr}{Pr_{\text{source}}} \right)^{0.25} \quad (3-2)$$

which is valid for $Re_{\text{source-cold}}$ from 40 to 1000 and Pr from 0.7 to 10. The temperature of the source can then be found from an energy balance, which results in:

$$T_{\text{source}} = \frac{P_{\text{source}}}{\pi d_{\text{source}} h_{AV}} + T_{\infty} \quad (3-3)$$

where P_{source} is the source power per unit length. Given that the ambient temperature is approximately 20°C, Re_{source} can then be calculated.

The Re_{source} is listed in table 3.3:

Table 3.3: Re_{source}

	low speed	high speed
small d_{source}	25	70
large d_{source}	51	111

Since Re_{source} is above the critical value of 40, vortex shedding can occur in this experiment and therefore the possibility exists that the presence of the source slightly affects the flow field. No effects, however, are observed in the experiment. None of the measured velocity spectra are observed to have any

spikes, which would indicate vortex shedding. It can therefore be assumed that if vortex shedding is present, as expected from the Re_{source} , the turbulence intensity is large enough to mask any effect that it might have on the flow field.

The effect of buoyancy can be examined by comparing the buoyant production of turbulent kinetic energy to the dissipation of turbulent kinetic energy. The exact effect of buoyancy in the flow under consideration is difficult to estimate given that the temperature field is statistically homogeneous in the direction of the gravitational acceleration vector. As a “worst-case” estimate, one can “rotate” the channel 90° and assume that the direction of gravitational acceleration is in the transverse direction. In this case, the above-mentioned buoyancy ratio is:

$$\frac{g\langle u_2\theta \rangle}{\frac{T}{\varepsilon}} \quad (3-4)$$

A typical value is 1.7% (for $y_{source}/h = 0.067$, $x/h = 4.0$, $Re = 22800$), which shows that buoyancy has a small effect on the flow field and the scalar can be considered passive.

3.1.3 The Nature of the Thermal Wall Boundary Condition

The channel was designed such that the walls could be considered adiabatic. Measurements of the mean profile, chapter 4, show that the mean temperature rise is always less than 0.4°C. Assuming a worst-case scenario, the average inside wall temperature will be at most 0.4°C above the ambient temperature (T_∞) throughout the measured section of the thermal plume, for the

small diameter source. Note that the outside wall temperature will be approximately T_{∞} . Hence the following calculation is done with a generous factor of safety, which includes the neglected convective resistance between the wall and the fluid. Treating the wall as an infinite slab, the heat flux per unit length in the z-direction through the wall is (at steady state):

$$q' = \kappa_{plexiglas} L \left(\frac{\Delta T_{wall}}{t_{wall}} \right) \quad (3-5)$$

where L is the length of the measured thermal plume in the x-direction and ΔT_{wall} is the difference between the inside and the outside wall temperatures. Equation 3-5 results in $q' = 2 \text{ W/m}$. This value is 5% of the total power input. Given that the temperature rise is linear with power input, the maximum heat lost through the wall for the large diameter source will also be 5% of the total input. Although there could be some heat loss through the wall as shown, its effect on the scalar dispersion is minimal and the wall can be considered adiabatic.

The nature of the wall boundary condition can also be considered from another perspective. The Biot number is the ratio of the conductive to the convective resistance. Using the Seider-Tate correlation:

$$Nu_{AV} = 0.027 Re^{0.8} Pr^{0.33} \quad (3-6)$$

(where the Reynolds number is based on the hydraulic diameter of the channel and the mean flow rate) the convective heat transfer coefficient can be estimated. The Biot number ($=h_{av} \kappa_{plexiglas} / t_{wall}$) is approximately 25 for the low Reynolds number and 42 for the high Re. (This implies that the temperature drop across the wall will be at most 1/25 of the temperature drop between the bulk mean temperature of the fluid and the inner wall temperature.) For the

purpose of this experiment, having $Bi \geq 25 \gg 1$ sufficiently approximates an adiabatic wall.

3.1.4 Source Diameter Independence Test

Three distinct regions of the thermal plume (molecular diffusive, turbulent-convective, and turbulent-diffusive) are evident if the source size is smaller than the Kolmogorov scale (Veeravalli and Warhaft, 1990). It is desired that the resultant thermal plume be independent of d_{source} , and exhibit these regions. Figures 3.7 and 3.8 plot the RMS and skewness profiles of the temperature for two separate source diameters. These figures illustrate that the measured moments of the plume are independent of the source diameter. For this test, $d_{\text{source}}/\eta = 0.85$ and 1.7 for the small and large diameter source, respectively. The Re_{source} is 25 and 51 for the small and large diameter source, respectively. These two chosen source sizes examine the effect of the ratio d_{source}/η for values less than and greater than unity. The thermal plume close to the source was not examined and it is possible that the plume close to the source is dependent on the source size. However, it can be seen that both the RMS and skewness profiles of the scalar at $x/h = 15.2$ with $y_{\text{source}}/h = 0.067$ collapse at the low Re .

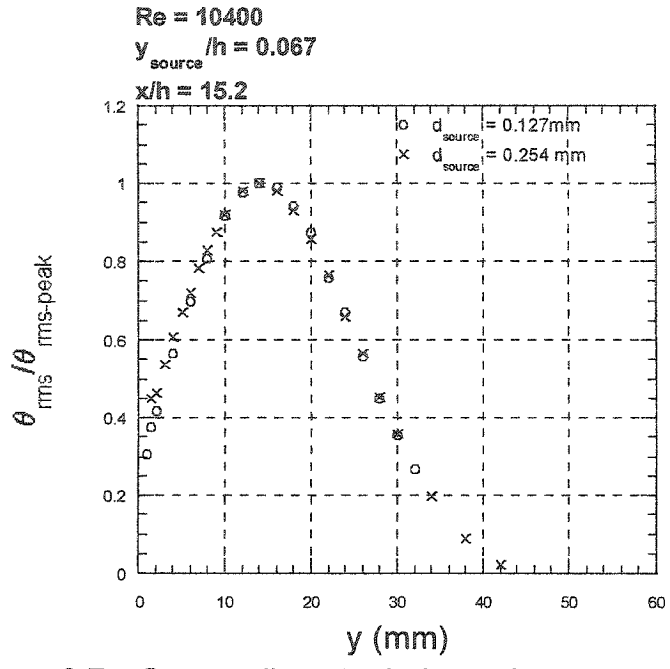


Figure 3.7 – Source diameter independence test, θ_{RMS} profiles

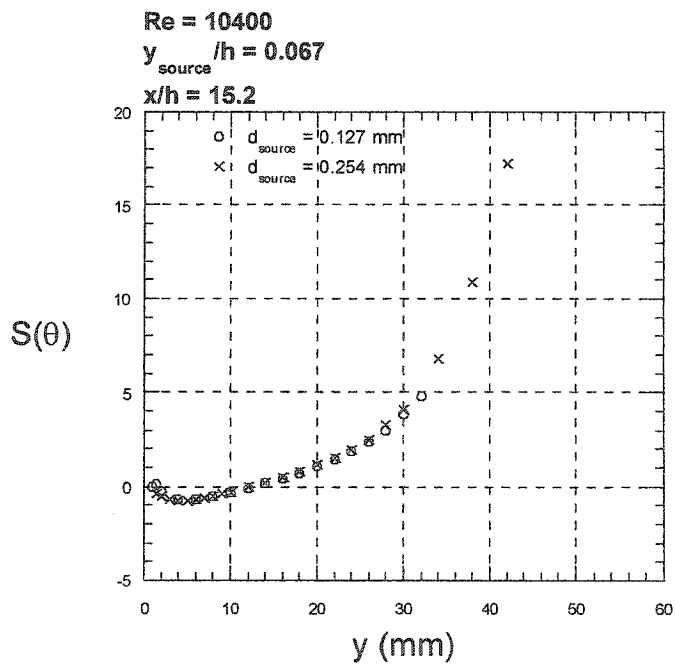


Figure 3.8 – Source diameter independence test, $S(\theta)$ profiles

3.1.5 Independence of z-direction

McLeod (2000) has experimentally shown that the channel flow is independent of the z-axis from $z = 0.25$ m to $z = -0.25$ m. It is therefore assumed that the thermal plume will also be independent of the z-axis in the center region of the channel.

3.1.6 Fully Developed Test of the Passive Scalar

Section 3.1.1 indicated that the flow field was fully-developed. A fully-developed test that examines the scalar field (rather than the velocity field) is to inject the scalar into the flow at i) two separate downstream positions from the entrance (which are both located in the fully-developed part of the flow) and ii) the same y_{source}/h location, and examine the resultant thermal plume at corresponding downstream positions. This test eliminates any possibility that the field under consideration in the present work (i.e. the scalar field) is not fully developed. To this end, the small diameter source was located at $y/h = 0.66$ for two separate downstream positions from the entrance, which correspond to $x/h = 10.8$ at Port 8-1 and Port 8-2, respectively. The transverse RMS and skewness profiles of temperature, shown in figures 3.9 and 3.10, collapse for corresponding x/h and y_{source} locations.

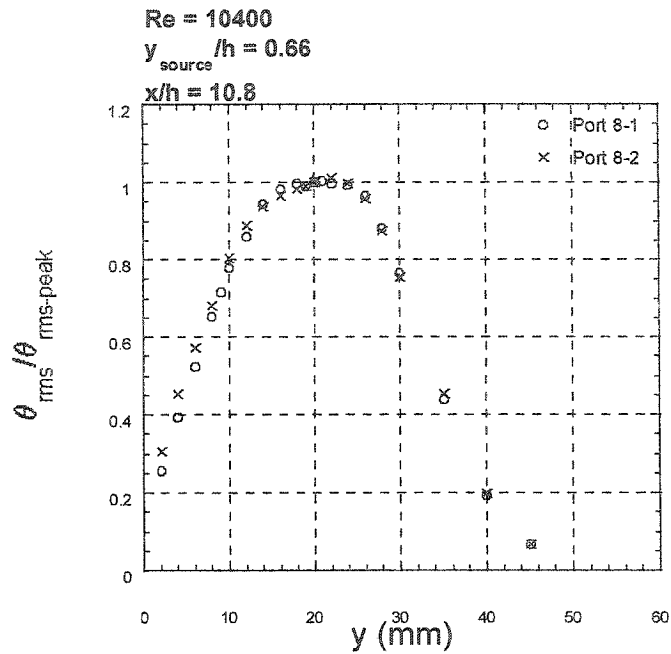


Figure 3.9 – Fully developed source test, θ_{RMS} profiles

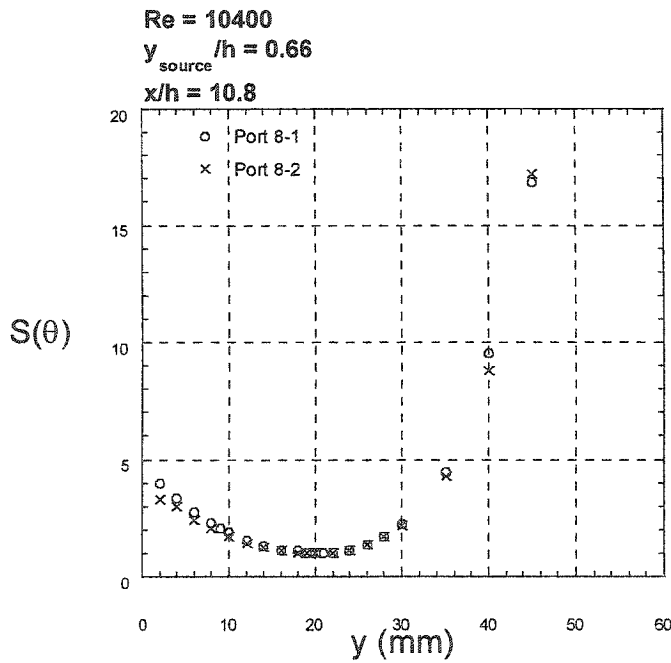


Figure 3.10 – Fully developed source test, $S(\theta)$ profiles

3.1.7 Symmetry Test

The flow field should be symmetrical about a plane of symmetry that is parallel to the x-z plane and passes through $y = 30\text{mm}$ (i.e. $y/h=1$). The symmetry of the mean flow at the low Reynolds number is illustrated in figure 3.11, where the mean flow is plotted versus the absolute value of $(y-30\text{ mm})$ for $y>30\text{mm}$ and $y<30\text{mm}$. As well, when $y_{\text{source}}/h = 1$, the thermal plume should be symmetric about this plane. Figure 3.12 demonstrates the collapse of the PDF of the temperature fluctuation for two locations, $y/h = 0.83$ and 1.17 , which correspond to equal and opposite distances about the plane of symmetry. This test was done at the low Reynolds number at a downstream location of $x/h = 15.2$.

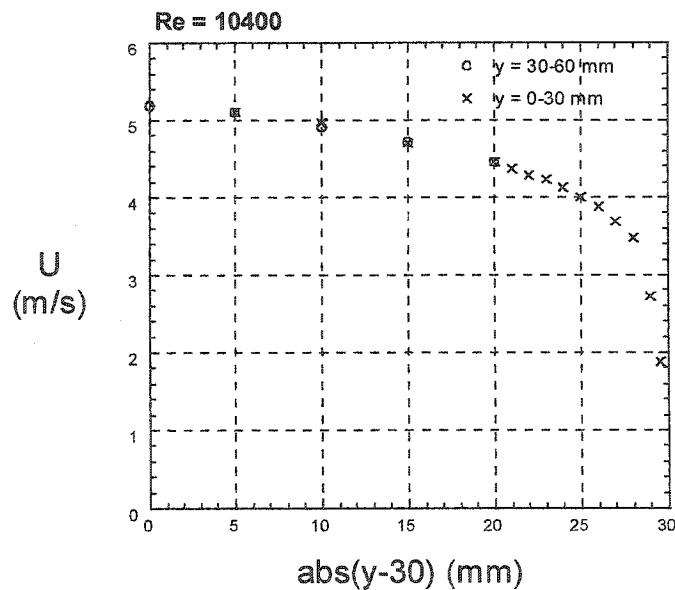


Figure 3.11 – Symmetry test of U profile

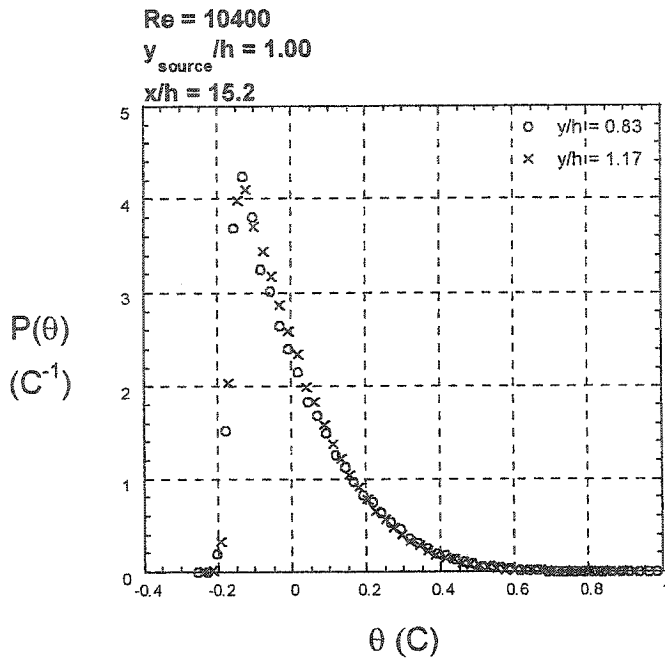


Figure 3.12 – Symmetry test of $P(\theta)$

3.2 Flow Properties

Tables 3.4 and 3.5 list various properties of the turbulent flow fields at the low and high Re . This section discusses how the flow properties were calculated.

The rate of dissipation of turbulent kinetic energy, ε , can be estimated from small-scale statistics of the velocity field, which, following the notions of Kolmogorov (1941) are assumed to be isotropic. The following equation relates the dissipation to the power spectrum of the longitudinal velocity fluctuation ($E_{11}(\kappa_1)$) in isotropic turbulence, where κ_1 is the longitudinal wavenumber (Tennekes and Lumley, 1972):

$$\varepsilon = 15\nu \int_0^{\infty} \kappa_1^2 E_{11}(\kappa_1) d\kappa_1. \quad (3-7)$$

Equation 3-7 requires first that the directly measured frequency spectrum ($E_{11}(f)$) be converted to a wavenumber spectrum. This task is accomplished by invoking Taylor's Hypothesis, which requires that the flow field have a constant mean velocity in the x-direction (Hinze, 1975). Taylor's hypothesis results in the following relations:

$$\kappa_1 = \frac{2\pi f}{U} \quad (3-8)$$

$$E_{11}(\kappa_1) = \frac{U}{2\pi} E_{11}(f). \quad (3-9)$$

The spectrum is then corrected to compensate for the finite spatial resolution of the hot-wire anemometer (due to the finite length of the sensor), using the procedure of Wyngaard (1968). Given the corrected spectra, equation 3-7 is then employed to calculate the dissipation of turbulent kinetic energy. Given the dissipation, the Kolmogorov scale, η , is calculated using equation 2-9.

One of the many ways the integral scale, ℓ , can be estimated is (Tennekes and Lumley, 1972):

$$\ell = \frac{u_{RMS}^3}{\varepsilon} \quad (3-10)$$

which approximates the size of the largest eddies.

Taylor microscale, λ , is defined by:

$$\frac{(u_{RMS})^2}{\lambda^2} \equiv \left\langle \left(\frac{\partial u}{\partial x} \right)^2 \right\rangle. \quad (3-11)$$

The microscale Reynolds number, Re_λ , defined as:

$$Re_\lambda \equiv \frac{u_{RMS} \lambda}{\nu} \quad (3.12)$$

is the ratio of the large-eddy time scale to the time scale of the strain-rate fluctuations (Tennekes and Lumley, 1972).

Table 3.4 lists various properties of the flow field at the low Re .

Table 3.4: Low Re flow properties

y (mm)	ε	ℓ (mm)	λ (mm)	η (mm)	Re_λ
1.0	6.96	33.8	3.36	0.148	138.2
2.0	6.17	25.0	3.11	0.153	111.2
3.0	5.59	19.9	3.09	0.157	98.8
4.0	4.73	19.7	3.17	0.163	95.8
5.0	4.05	19.2	3.29	0.170	93.7
6.0	3.48	20.3	3.45	0.177	94.9
7.0	3.11	21.3	3.56	0.181	95.9
8.0	2.73	21.5	3.67	0.187	95.1
9.0	2.44	23.2	3.80	0.193	97.1
10.0	2.15	24.7	3.91	0.199	97.9
15.0	1.32	26.9	4.26	0.225	93.3
20.0	0.88	25.6	4.54	0.249	85.3
25.0	0.62	18.5	4.38	0.271	66.0
30.0	0.56	16.0	4.19	0.278	58.1

Table 3.5 lists various properties of the flow field at the high Re.

Table 3.5: High Re flow properties

y (mm)	ε	ℓ (mm)	λ (mm)	η (mm)	Re_λ
1.0	74.08	17.5	1.99	0.082	144.8
2.0	56.86	17.1	2.08	0.088	137.3
3.0	52.71	16.9	2.25	0.089	144.3
4.0	37.42	22.7	2.50	0.097	157.9
5.0	31.00	25.1	2.64	0.102	161.8
6.0	26.86	28.8	2.82	0.106	172.5
7.0	23.88	29.7	2.91	0.109	173.0
8.0	21.63	30.0	3.00	0.112	173.1
9.0	19.57	31.3	3.10	0.115	175.5
10.0	19.38	29.8	3.16	0.115	175.4
15.0	12.35	30.8	3.45	0.129	166.7
20.0	8.62	27.2	3.62	0.141	148.9
25.0	6.67	18.6	3.48	0.150	115.7
30.0	4.70	19.7	3.32	0.164	100.2

Chapter 4

Results

This chapter presents results for the mean and fluctuating temperature field, with emphasis on the statistical behavior of the temperature fluctuations and their transport by the turbulent velocity field. Experiments were performed at two different Reynolds numbers, with the source located at three positions from the wall. Table 4.1 summarizes the flow properties for the six experimental conditions studied in this thesis.

Table 4.1: Experimental conditions

		low Re	high Re
Velocities	$U_{\text{centerline}}$	5.2 m/s	11.4 m/s
	u^*	0.26 m/s	0.54 m/s
Reynolds numbers	Re	10400	22800
	Re_{τ}	520	1080
	$Re_{\lambda(y/h=1)}$	58.1	100.2
3 Source Positions	$y/h=0.067$	$y^+=35$	$y^+=72$
	$y/h=0.17$	$y^+=87$	$y^+=180$
	$y/h=1.0$	$y^+=520$	$y^+=1080$

4.1 Mean Temperature Field

This section presents the results for the mean temperature field. A cold-wire is used to measure the mean temperature. To compensate for drifts in room temperature, the unheated “cold” ambient air temperature is subtracted from the

mean temperature measurements. The cold temperature is measured by a mini-bead thermistor, located upstream of the source. A typical error in these measurements is 0.05 K and the peak mean temperature rise is on the order of 0.5 K (see figure 4.2, to be discussed). This small temperature rise subjects these measurements to a rather large source of error. More emphasis is therefore placed on the qualitative behavior of the mean temperature profiles. The temperature profile is not shown for $x/h = 22.0$ due to the weakness of the mean temperature signal at that furthest downstream location. Also note that the mean temperature profiles for the source located at the channel centerline were not measured.

In isotropic grid-generated turbulence (Warhaft, 1984), a Gaussian profile describes the transverse mean temperature profiles. Gaussian profiles also initially describe the mean temperature profiles behind a concentrated source in homogeneous turbulent shear flow. Further downstream, the profiles become asymmetric, and their peaks shift to the region of lower velocity (Karnik and Tavoularis, 1989). In this work, the mean profiles (normalized by the peak mean temperature) are studied. A best-fit Gaussian curve of the form:

$$\frac{\Delta T}{\Delta T_{PEAK}} = \exp \left(\frac{- \left(\frac{y}{h} - \frac{y_{peak}}{h} \right)^2}{2 \left(\frac{\sigma_{MEAN}}{h} \right)^2} \right) \quad (4-1)$$

is used to fit the data. (σ_{MEAN} is the standard deviation of the Gaussian distribution and quantifies the width of the profile.)

Figure 4.1 plots the transverse mean temperature rise profiles normalized by the peak mean temperature. These profiles indicate that the temperature profile is more uniform near the wall, for the source locations close to the wall, as expected. The peaks of the mean profiles are relatively fixed behind the source and do not appear to be drifting to the region of lower velocity (over the range of downstream locations measured) as is seen in homogeneous turbulent shear flow (Karnik and Tavoularis, 1989) and in boundary layers (Kabiri et al., 1998). However, the lack of near-wall data, due to the interference of the probes with the wall, makes it difficult to determine the exact location of the peak concentration. In addition, the drift of the peak of the mean temperature profiles observed in homogeneous turbulent shear flow only occurred for downstream distances much larger than those measured herein.

In isotropic grid-generated turbulence, as well in homogeneous turbulent shear flow, the decay rate of the peak mean temperature is well-described by a power law decay:

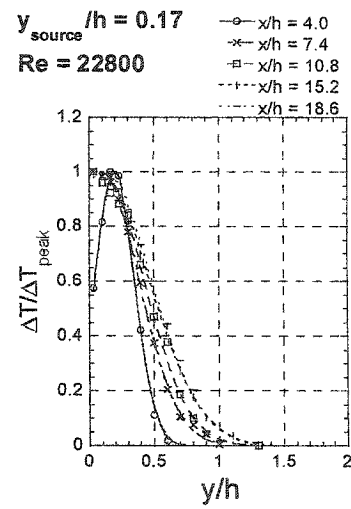
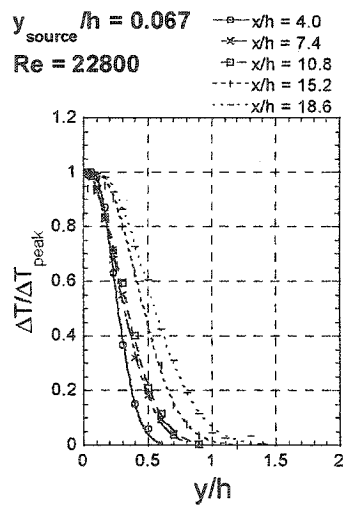
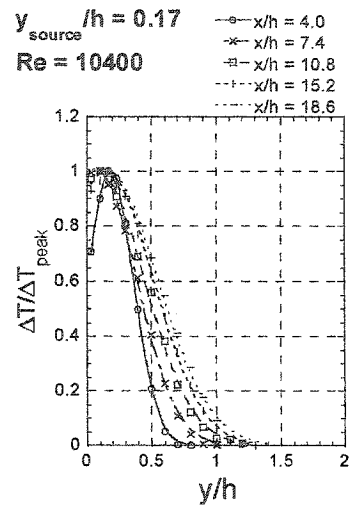
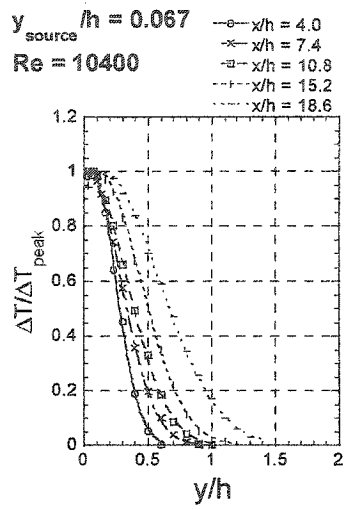
$$\Delta T \propto (x/h)^{-n} \quad (4-2)$$

where n is the decay exponent. Figure 4.2 plots the peak temperature excess as a function of downstream distance. It shows that this exponent does not obey a strict power law decay. At the far downstream locations, where the plume width is largest, the decay of the peak temperature appears to accelerate. Nevertheless, fitting a power law to this decay results in a decay exponent of 0.5, which is less than the values obtained in isotropic grid-generated turbulence

(approximately 1) and homogeneous turbulent shear flow (approximately 1) (Karnik and Tavoularis, 1989).

The width of the mean temperature excess profiles is plotted in figure 4.3 as a function of downstream distance. These profiles are approximately linear, which correspond to the observations in the turbulent-convective range of isotropic grid generated turbulence (Warhaft, 1984) and homogeneous turbulent shear flow (Karnik and Tavoularis, 1989). For the high Re , the profiles are observed to be thinner, which is a result of the increased advection associated with the larger mean flow rate.

For a relatively small distance in the streamwise direction, a turbulent boundary layer can be considered homogeneous in the streamwise direction and the equation of motion is similar to turbulent channel flow. Turbulent channel flow and a turbulent boundary layer are therefore almost identical between the wall and the end of the log-law region. The mean temperature rise profiles for the near-wall source locations ($y_{source}/h = 0.067$ and 0.17) exhibited similar qualitative behavior to dispersion from a line source placed in a turbulent boundary layer (Kabiri et al., 1998) in the initial stage of the plume development, before the plume reached the end of the log-law region.



Re



y_{source}/h →

Figure 4.1 – Transverse mean temperature rise profiles

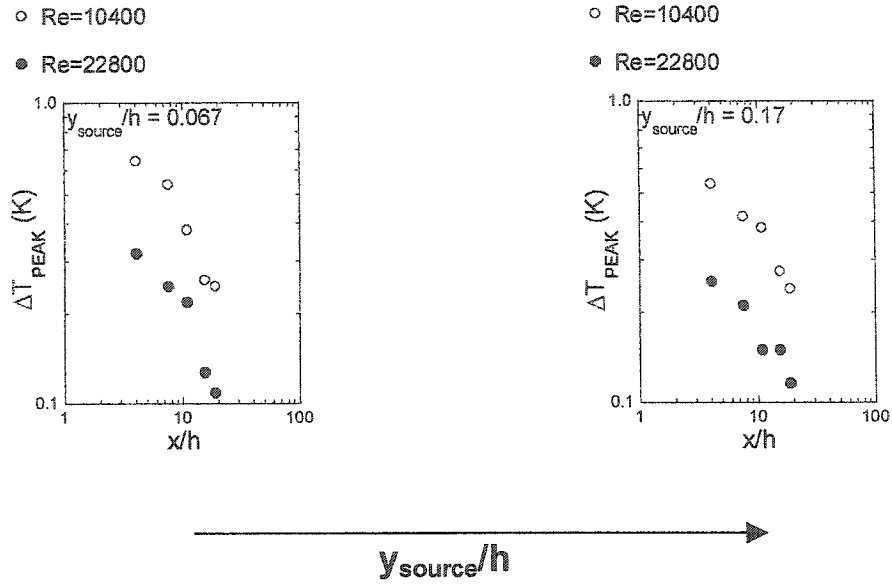


Figure 4.2 – Downstream mean temperature decay

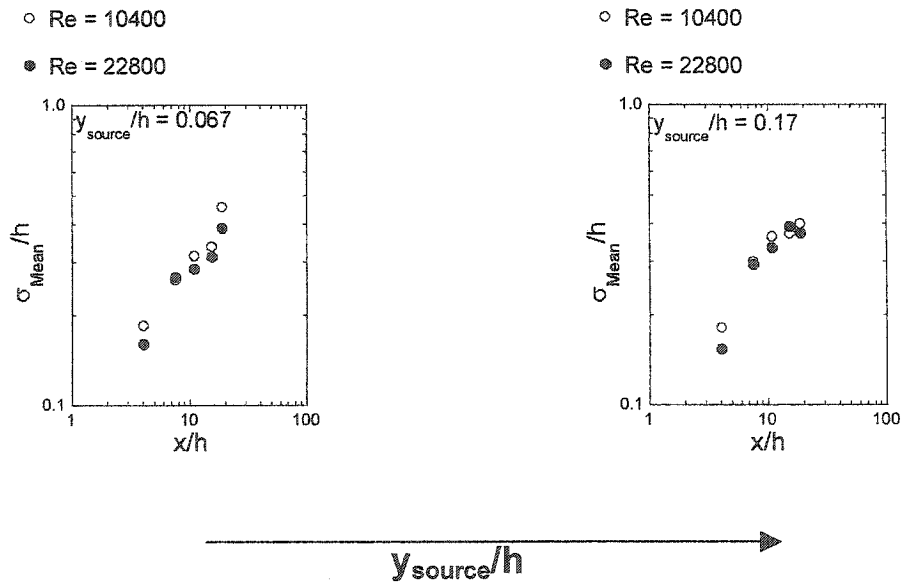


Figure 4.3 – Mean temperature profile widths

4.2 Fluctuating Temperature Field

Before being digitized, the fluctuating temperature signal is high-pass filtered. This filtering eliminates any error from drifts in the room temperature because such drifts occur at frequencies smaller than the high-pass frequency (0.1 Hz). Therefore, the error in the mean temperature field discussed in section 4.1 is not present in any of the measurements involving the fluctuating temperature signal.

Figure 4.4 shows the transverse profiles of θ_{RMS} normalized by their peak values. Throughout the region examined, best-fit Gaussian curves of the form:

$$\frac{\theta_{RMS}}{\theta_{RMS-peak}} = \exp\left(\frac{-\left(\frac{y}{h} - \frac{y_{peak}}{h}\right)^2}{2\left(\frac{\sigma_{RMS}}{h}\right)^2}\right) \quad (4-3)$$

well describe this data. (σ_{RMS} is the standard deviation of a Gaussian distribution and quantifies the width of the profile.)

The decrease in the downstream peak of the RMS has been described by a power law decay of the form:

$$\theta_{RMS-peak} \propto (x/h)^{-n} \quad (4-4)$$

where n is the decay exponent (Karnik and Tavoularis, 1989). Figure 4.5 shows that the decay exponent is approximately 1, for all source locations and Reynolds numbers. In homogeneous turbulent shear flow, Karnik and Tavoularis (1989) found that two distinct regions of decay exist for homogeneous turbulent shear flow, where n is initially 0.85 and further downstream of the source is 1.6.

Figure 4.6 shows the growth of the θ_{RMS} profile widths. The curve fits to the profile widths are tabulated in table 4.2. The lower Re always has a slightly larger width, due to the slower advection. For the source located on the channel centerline, the profile growth is the largest. The θ_{RMS} profile growth for the source located at $y_{\text{source}}/h = 0.067$ grows at a slightly larger rate than the $y_{\text{source}}/h = 0.17$ location. The ratio of σ_{RMS} to σ_{MEAN} is approximately 1 for the source located at $y_{\text{source}}/h = 0.067$ and 0.17. Warhaft (1984) found that the ratio of σ_{RMS} to σ_{MEAN} is approximately 1.5 in isotropic grid generated turbulence.

It is observed that the peaks of the RMS profiles drift toward the center of the channel for the off-center source locations ($y_{\text{source}}/h = 0.067$ and 0.17). This drift is slightly more pronounced for the lower Reynolds number, as shown in figure 4.7, which plots the location of the RMS peak versus x/h . Off-centerline RMS peaks are observed in isotropic grid-generated turbulence and homogeneous turbulent shear flow in the form of double peaks, which are the result of the plume width far exceeding the integral length scale of the turbulence (as discussed in section 1.3.4). In bounded flows like the present one, the plume cannot exceed the integral length scale, implying that the RMS drift occurs for reasons other than that of the double peaks. These drifts are further examined in section 4.3.

The RMS temperature profiles also exhibited similar behavior to the RMS temperature profiles of dispersion from a line source placed in a turbulent boundary layer (Kabiri et al., 1998), throughout the studied region.

Finally, it should be noted that $\sigma_{RMS}/\Delta T$ profiles are not constructed due to the relatively large error of the mean temperature rise profiles.

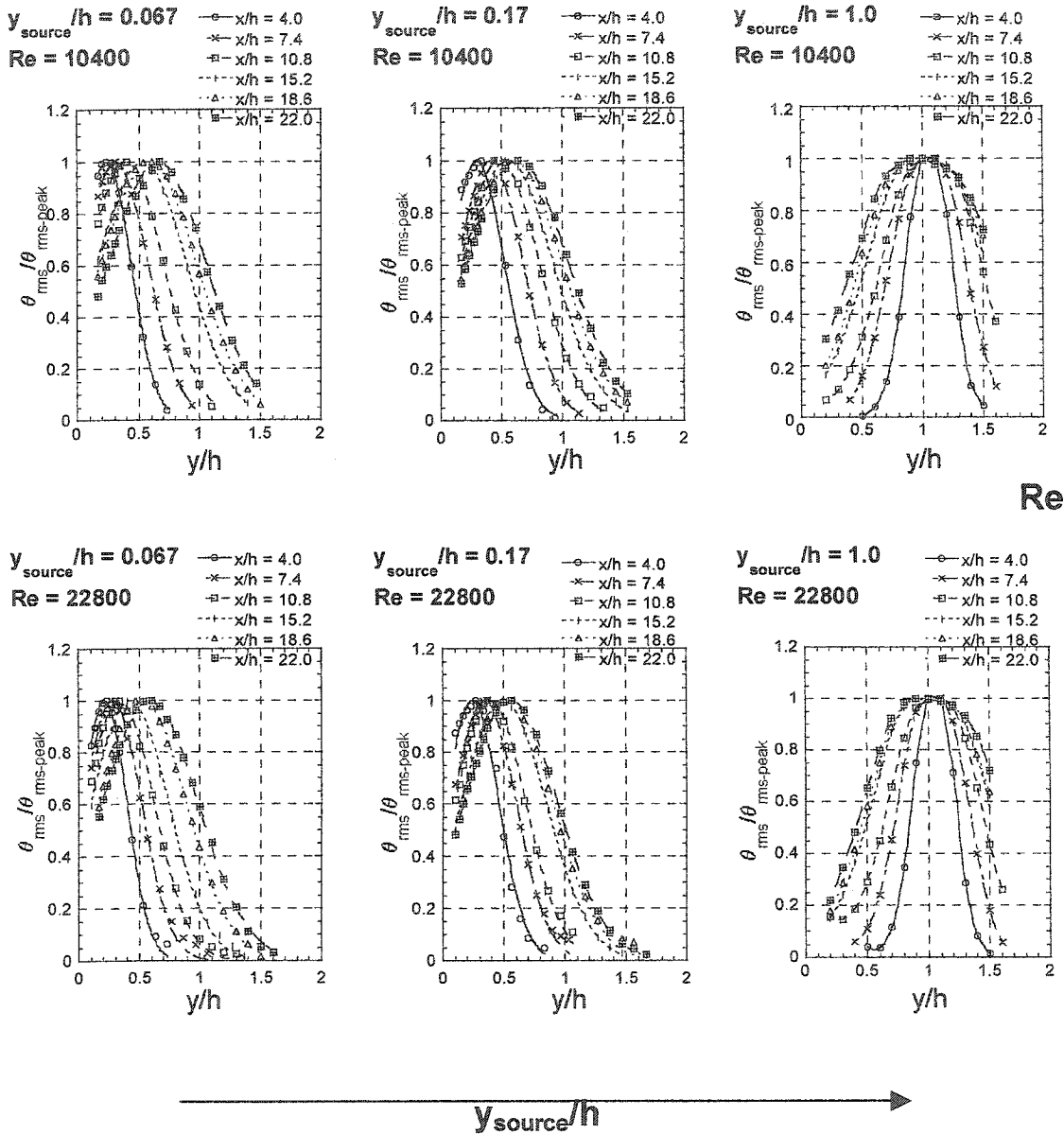


Figure 4.4 – Transverse θ_{RMS} profiles

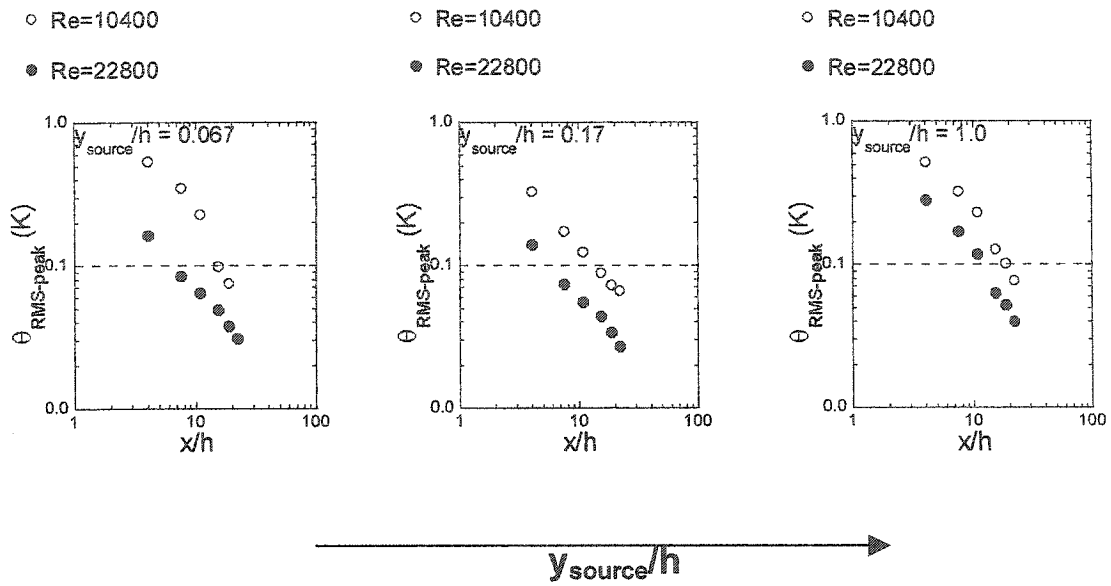


Figure 4.5 – Downstream decay of peak values of θ_{RMS} profiles

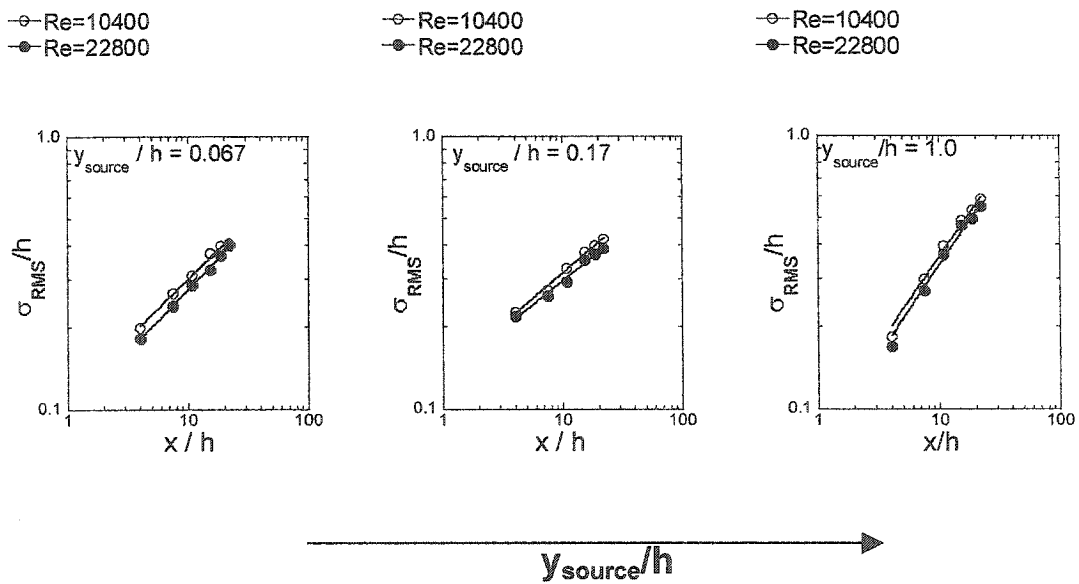


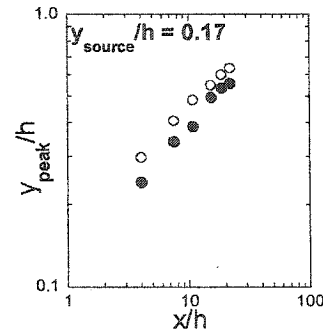
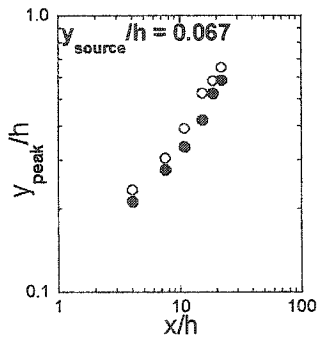
Figure 4.6 – Widths of θ_{RMS} profiles

Table 4.2: Widths of θ_{RMS} profiles

$\sigma_{RMS} = Ax^m$			
y_{source}/h	Re	A	m
0.067	10400	0.111	0.431
	22800	0.096	0.454
0.17	10400	0.134	0.372
	22800	0.132	0.348
1	10400	0.075	0.679
	22800	0.067	0.697

○ Re = 10400
● Re = 22800

○ Re = 10400
● Re = 22800



→ y_{source}/h

Figure 4.7 – RMS peak drifts

4.3 Temperature PDFs

The PDF is a description of how a fluctuating variable is distributed (in the statistical sense). In theory, it contains information on the statistical moments of all orders. This section examines the behavior of the PDFs of the fluctuating temperature, which highlights some of the physical processes that govern the scalar dispersion. A complete PDF database can be found in Appendix I.

If a scalar is introduced into a turbulent flow at a small scale, as in this case, the temperature fluctuations are produced by two mechanisms. One is the internal structure of the thermal plume itself. The second is the bulk flapping of the plume, where the instantaneous plume is moved from side to side by the large eddies. The bulk flapping results in an instantaneous meandering plume profile downstream of the source (for the downstream locations where the plume width is smaller than the largest eddies). As the plume meanders back and forth, given points are exposed to both the thermal plume and the cold fluid. This is known as external intermittency, which is apparent in the PDF, where a spike is seen at the cold fluid temperature for certain sets of measurements.

Figure 4.8 shows the PDFs at different transverse locations, source locations, and Reynolds numbers for the position $x/h = 7.4$. The near-wall PDF indicates that the scalar distribution is better mixed as the Re is increased for the source locations of $y_{source}/h = 0.067$ and 0.17 . This is exhibited by PDFs which have a form that more closely resembles a Gaussian distribution as the Re is increased. As the plume is traversed in the direction of increasing y , the PDF evolves into a very positively skewed shape with a spike at the cold fluid temperature. For the source located at the channel centerline, the entire transverse PDF field is positively skewed, with a spike at the cold fluid location, implying that for this downstream position, the flapping of the thermal plume plays a dominant role in the dispersion of the scalar field. Note that the location of the cold fluid spike changes in figure 4.8. This change is due to the change in

mean temperature. If the PDFs are plotted dimensionally versus the total temperature, the locations of the cold spikes will align themselves at T_w .

The downstream evolution of the PDFs, figure 4.9, demonstrates similar behavior. For all source locations and Re , the PDFs illustrate that the fluid is better mixed further downstream. As the source is located further from the wall, the PDF is more positively skewed, indicating that the near-wall source location better mixes the scalar in the initial plume stage. This result is expected, due to the relatively high turbulence intensity as the wall is approached.

Further examination of the peaks of the transverse RMS profiles indicates that the PDF exhibits a similar shape at these locations. This shape has two spikes, one at the location of the cold fluid, the second is in the region of the hot fluid. These spikes imply that the peak of the RMS is dominated by the bulk flapping of the thermal plume, and does not exclusively result from the internal structure of the plume itself.

Lastly, it should be noted that the PDF in the signal-to-noise ratio in the outer region of the thermal plume is rather poor and could strongly influence the shape of the PDFs (as the noise can not be subtracted out the PDF).

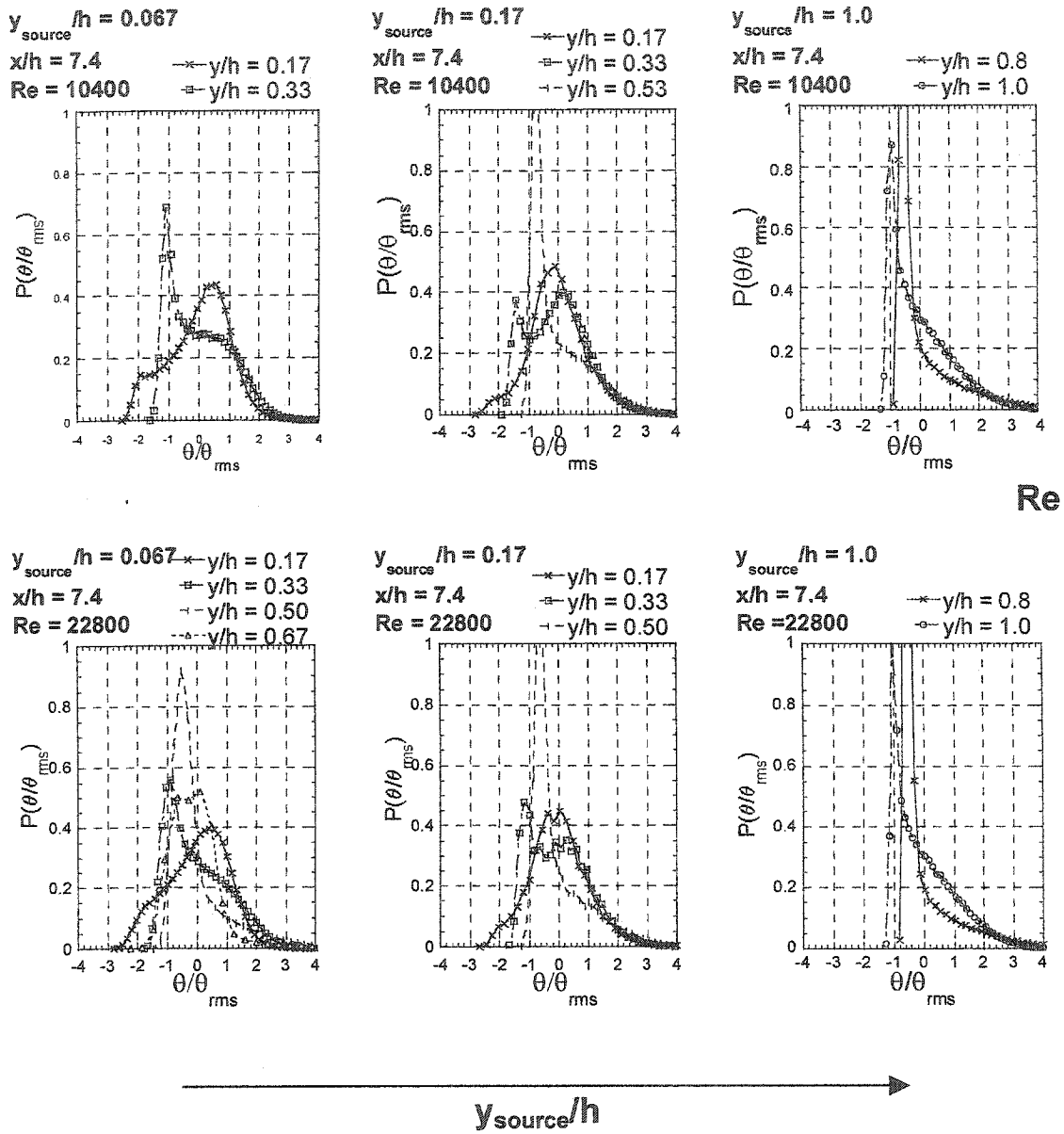


Figure 4.8 – PDFs for various transverse locations

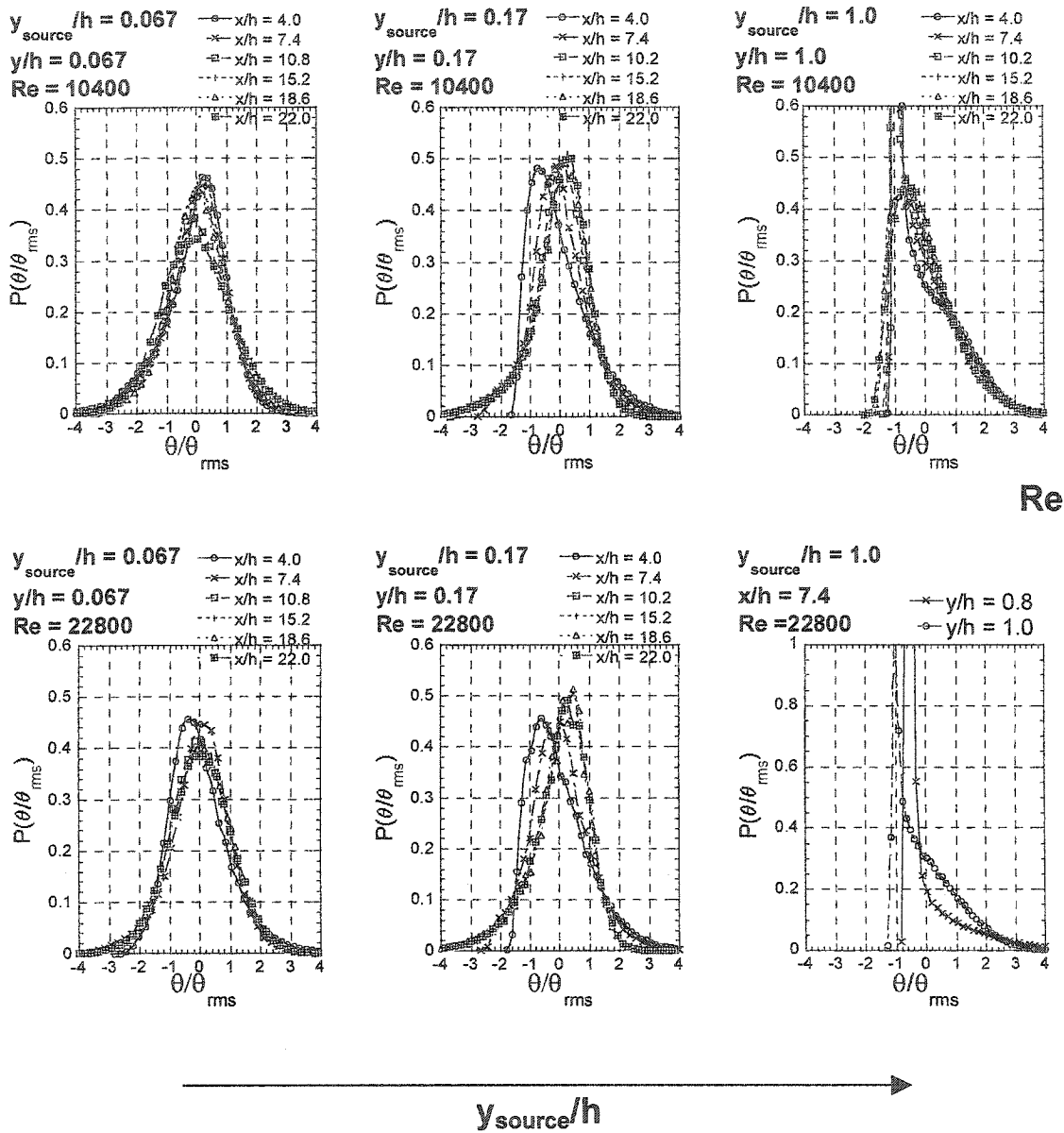


Figure 4.9 – PDFs for various downstream locations

4.4 Temperature Skewness

The skewness of the temperature fluctuations is defined as:

$$S(\theta) = \frac{\langle \theta^3 \rangle}{(\theta_{RMS})^3} = \frac{1}{(\theta_{RMS})^3} \int_{-\infty}^{\infty} \theta^3 P(\theta) d\theta. \quad (4-5)$$

It is a measure of the asymmetry of the PDF. Since the fluctuating temperature is bounded between that of the source and the cold fluid, the relative value of mean temperature strongly influences the skewness. As the mean temperature approaches the hot or cold value, only large one-sided fluctuations are possible, which affect the symmetry of the PDF and hence the skewness. Although the upper limit of the fluctuating temperature is that of the source, these hot fluctuations are quickly smeared out.

Figure 4.10 shows the transverse profiles of $S(\theta)$. For the source located at the channel centerline, the skewness is a minimum at transverse locations corresponding to $y = y_{\text{source}}$. This value tends to increase away from the y_{source} location until it obtains its maximum in the outer region of the thermal plume, then returns to zero when outside of the plume. The increasing skewness in the outer region of the thermal plume (with a return to zero outside of the plume) is also observed for the near-wall source locations. This trend is expected because the mean temperature approaches that of the cold fluid, limiting the “large” fluctuations to positive values only.

For the near-wall source locations ($y_{\text{source}}/h = 0.067$ and 0.17), the skewness decreases directly downstream of the source. The skewness is initially positive, decreasing until it takes on negative values. This trend is the result of the well-mixed temperature fluctuations near the wall as the thermal plume evolves, which are occasionally exposed to large negative temperature fluctuations from the cold fluid. Note that for the source located at the channel

centerline, the skewness directly downstream of the source tends to remain relatively constant.

With increasing Reynolds number, the values of the skewness in the outer region of the thermal plume tends to peak at lower values. The skewness profiles are also thinner as the Re is increased. These observations are due to the faster advection at the high Re .

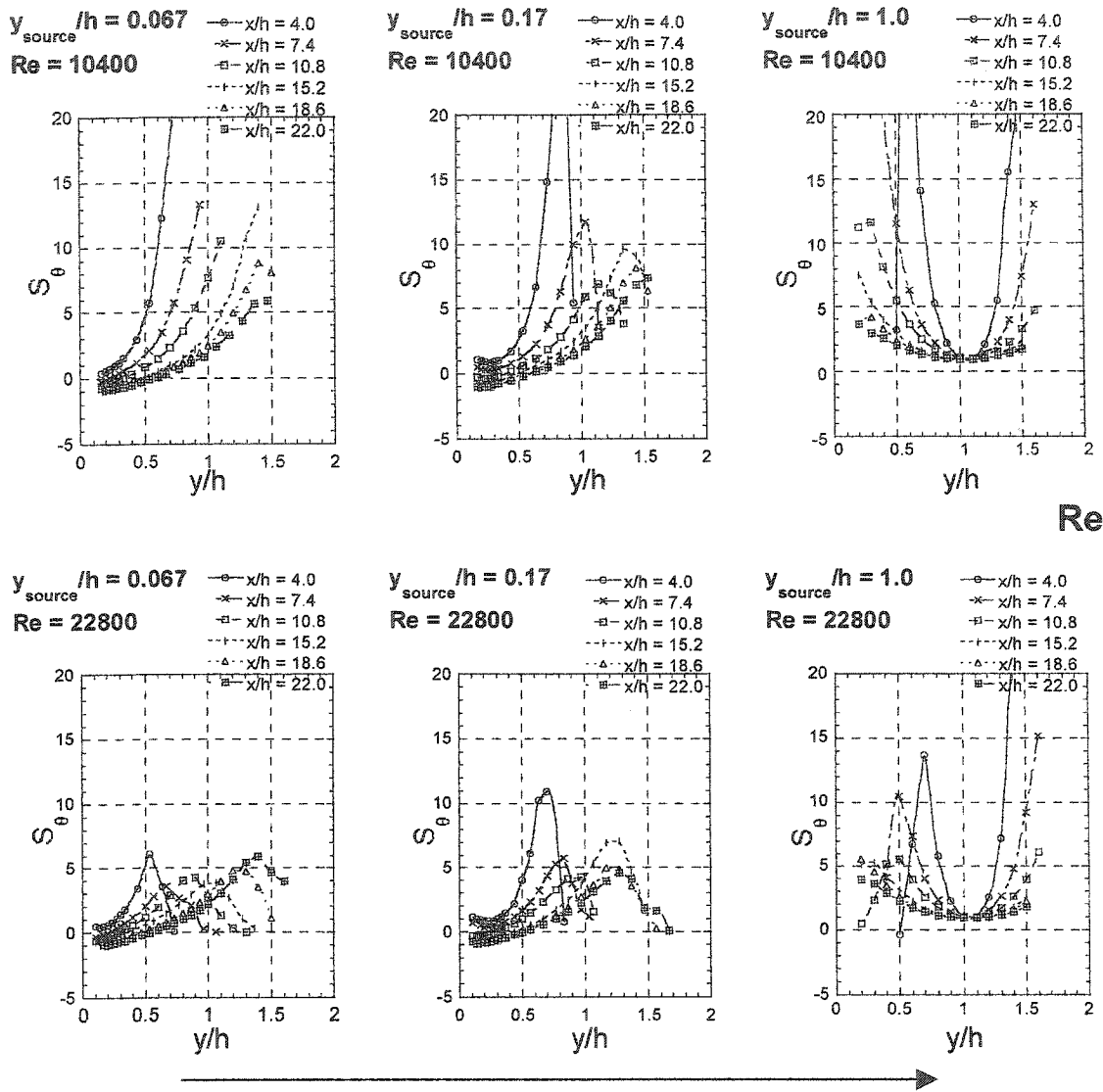


Figure 4.10 – Transverse S_θ profiles

4.5 Temperature-Velocity Correlations

This section presents measurements of some temperature-velocity correlations. A complete compilation of the temperature-velocity correlations can be found in Appendix I.

4.5.1 Turbulent Heat Flux

The correlation coefficient of two fluctuating quantities is defined as:

$$\rho_{ab} = \frac{\langle ab \rangle}{a_{RMS} b_{RMS}} \quad (4-6)$$

where a and b are the variables of interest.

Figures 4.11 and 4.12 show the correlation coefficients of $u-\theta$ and $v-\theta$, which are the non-dimensional (longitudinal and transverse) turbulent heat fluxes. For the source located at $y_{source}/h = 0.067$ and 0.17 , $\rho_{u\theta}$ and $\rho_{v\theta}$ are opposite in sign, due to the negative $u-v$ correlation in this region of the flow. (A negative $u-v$ correlation implies that when u is positive, v will tend to be negative and vice-versa.) The centerline source location shows that $\rho_{v\theta}$ is odd about $y/h = 1.0$ and $\rho_{u\theta}$ is (approximately) even about $y/h=1.0$, as expected.

The Re and the downstream distance from the source appear to have little effect on the overall shape of these profiles. With increasing Re , the profile shapes are observed to be slightly thinner, which corresponds to the θ_{RMS} and $S(\theta)$ profiles. As expected, the profile is wider with downstream distance, with no other significant change in shape.

These profiles are most influenced by the source location. The near-wall source locations exhibit similar behavior, however are quite different than the centerline source location.

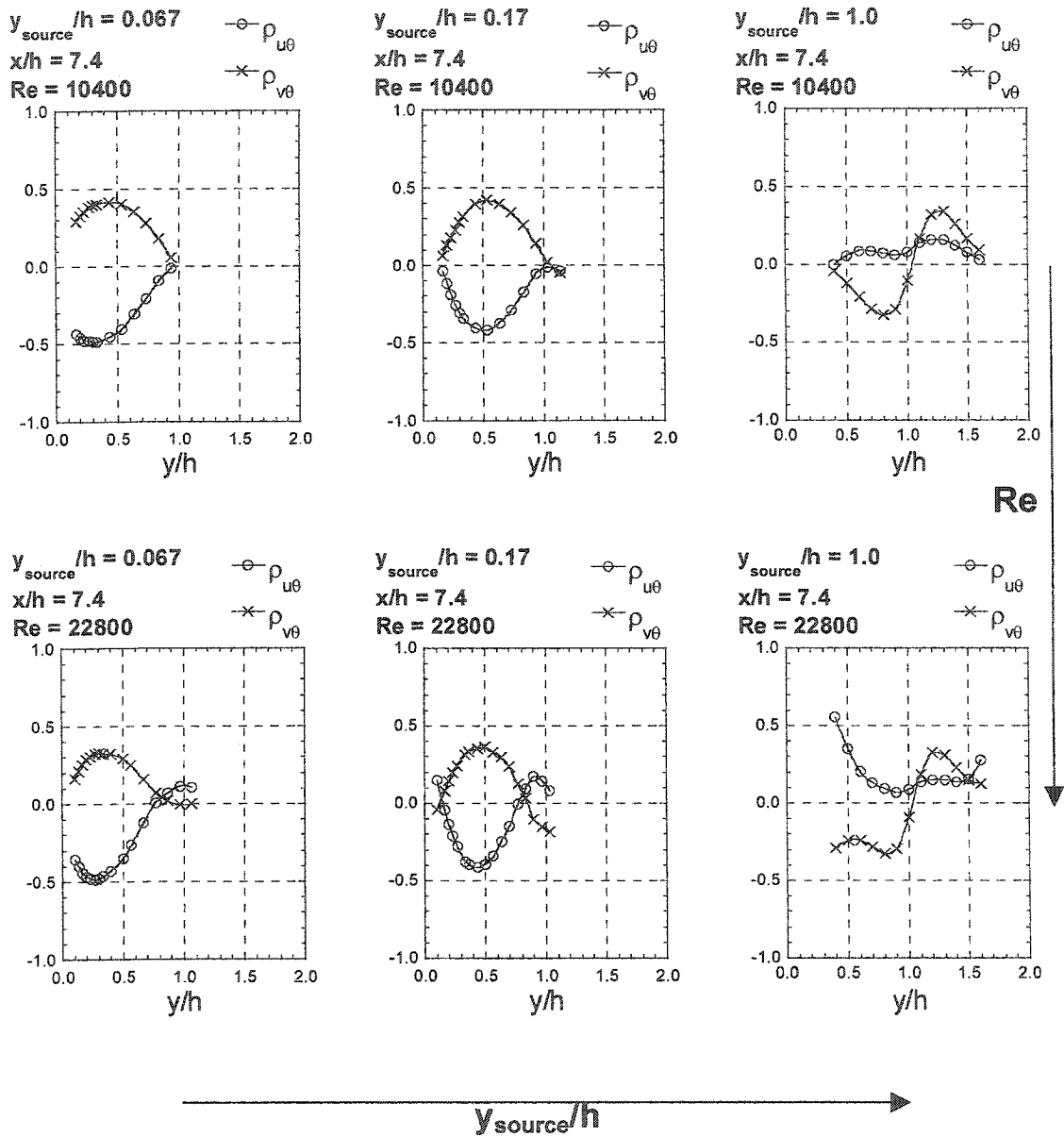
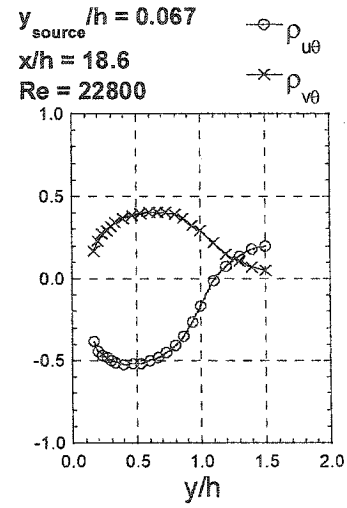
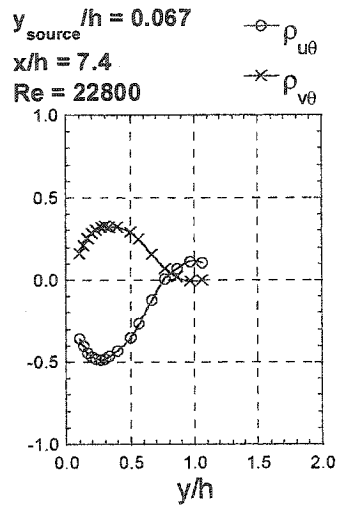
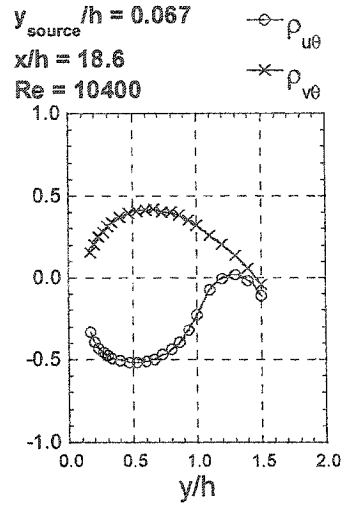
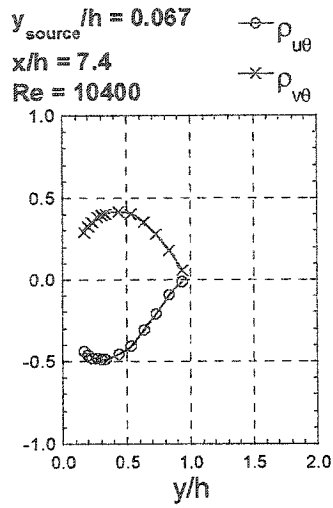


Figure 4.11 – Turbulent heat fluxes



Re

x/h

Figure 4.12 – Turbulent heat fluxes

4.5.2 Turbulent Variance Transport

The non-dimensional transport of scalar variance by turbulent velocity fluctuations is shown in figures 4.13 and 4.14. These quantities are non-dimensionalized as follows:

$$\langle \theta^2 u \rangle_{ND} = \frac{\langle \theta^2 u \rangle}{\langle \theta^2 \rangle u_{RMS}} \quad (4-7)$$

$$\langle \theta^2 v \rangle_{ND} = \frac{\langle \theta^2 v \rangle}{\langle \theta^2 \rangle v_{RMS}} \quad (4-8)$$

The Re affects the magnitude of the turbulent variance transport for the near-wall source locations, however not for the source location at the centerline. As the Re is increased, the peaks of the non-dimensional variance transport decreases, however the shapes of the profiles remain similar. This decrease is primarily due to the non-dimensionalization. If θ^2 is considered a variable in and of itself, a correlation coefficient can be defined as follows:

$$\rho_{\theta^2 v} = \frac{\langle \theta^2 v \rangle}{(\theta^2)_{RMS} v_{RMS}} = \frac{\langle \theta^2 v \rangle}{(\sqrt{K(\theta)-1}) \langle \theta^2 \rangle v_{RMS}} \quad (4-9)$$

where the kurtosis is defined as:

$$K(\theta) = \frac{\langle \theta^4 \rangle}{(\theta_{RMS})^4} \quad (4-10)$$

and $(K(\theta)-1)^{1/2} \langle \theta^2 \rangle$ is equal to the RMS of θ^2 . The ratio of the peaks of $\langle \theta^2 v \rangle_{ND}$ ($y_{source}/h=0.067$, $x/h=7.4$) is 2.2, while the ratio of $(K(\theta)-1)^{1/2}$ (not shown) is 2.2, implying that the difference in peaks arises from the non-dimensionalization. An alternative non-dimensionalization of the correlation coefficient could be employed, but is not since it would not follow the standard convention. What this

shows, however, is the effect of the PDF shape and its Reynolds number dependence on turbulent transport of θ^2 .

The downstream location from the source does not significantly affect the shape of the turbulent variance transport profiles (for $y_{\text{source}}/h=0.067$). As expected, the profile widths increase with increasing downstream distance. The peak of both $\langle\theta^2u\rangle_{\text{ND}}$ and $\langle\theta^2v\rangle_{\text{ND}}$ decrease in magnitude with downstream distance for each Re. Initially (at $x/h = 7.4$) the peaks of both profiles are at the same y location, and although the width of the profiles are the same at $x/h = 18.6$, the peak of $\langle\theta^2u\rangle_{\text{ND}}$ does not drift as much as the peak of $\langle\theta^2v\rangle_{\text{ND}}$.

Consistent with previous results, the source location is observed to have the most influence on the turbulent variance transport profiles. The near-wall source locations exhibit similar behavior, which is different from that at the centerline location. Regardless of source location, as the Re is increased, the widths of the profiles are observed to be thinner, in agreement with all previous measurements.

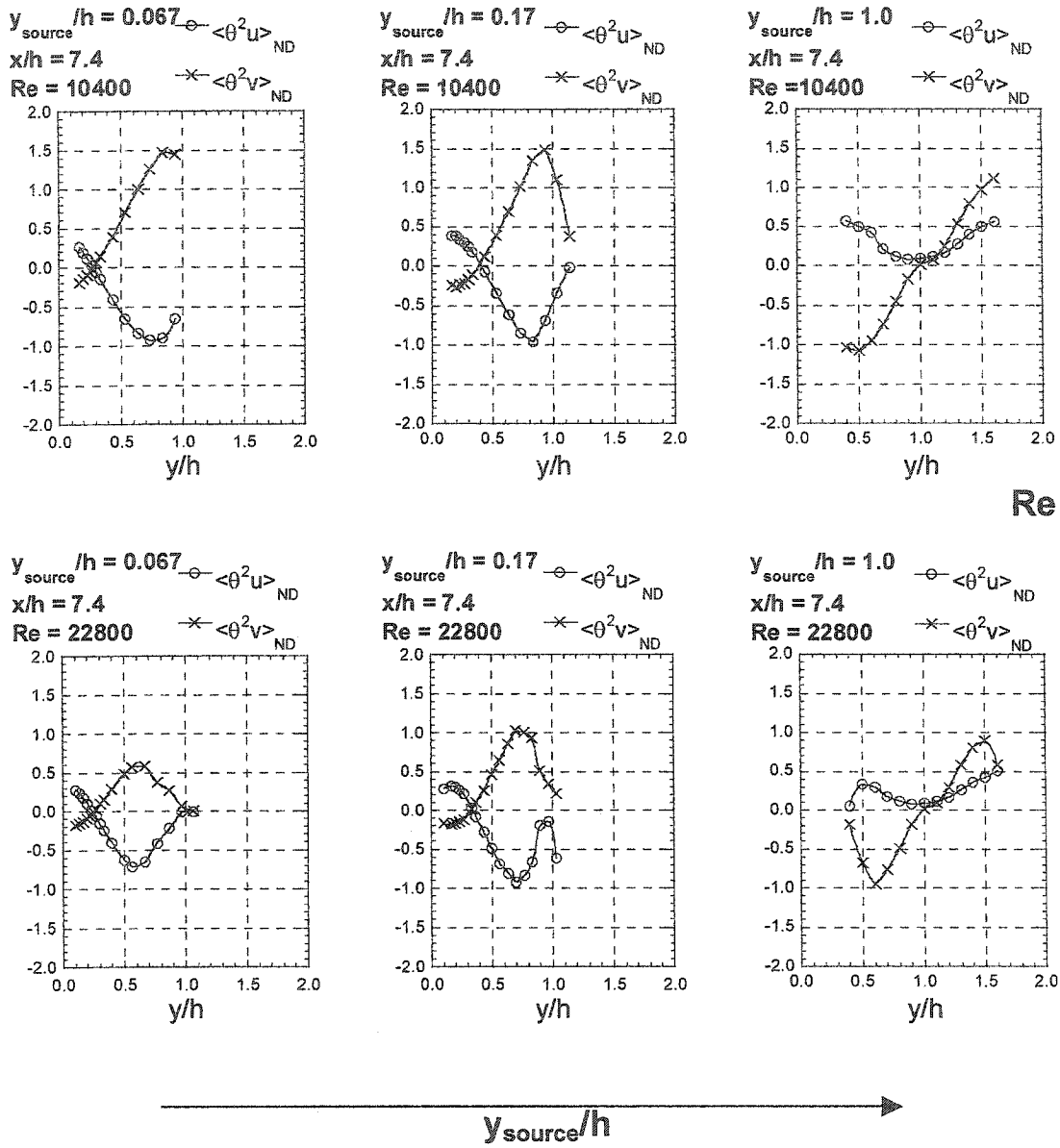


Figure 4.13 – Turbulent variance transport

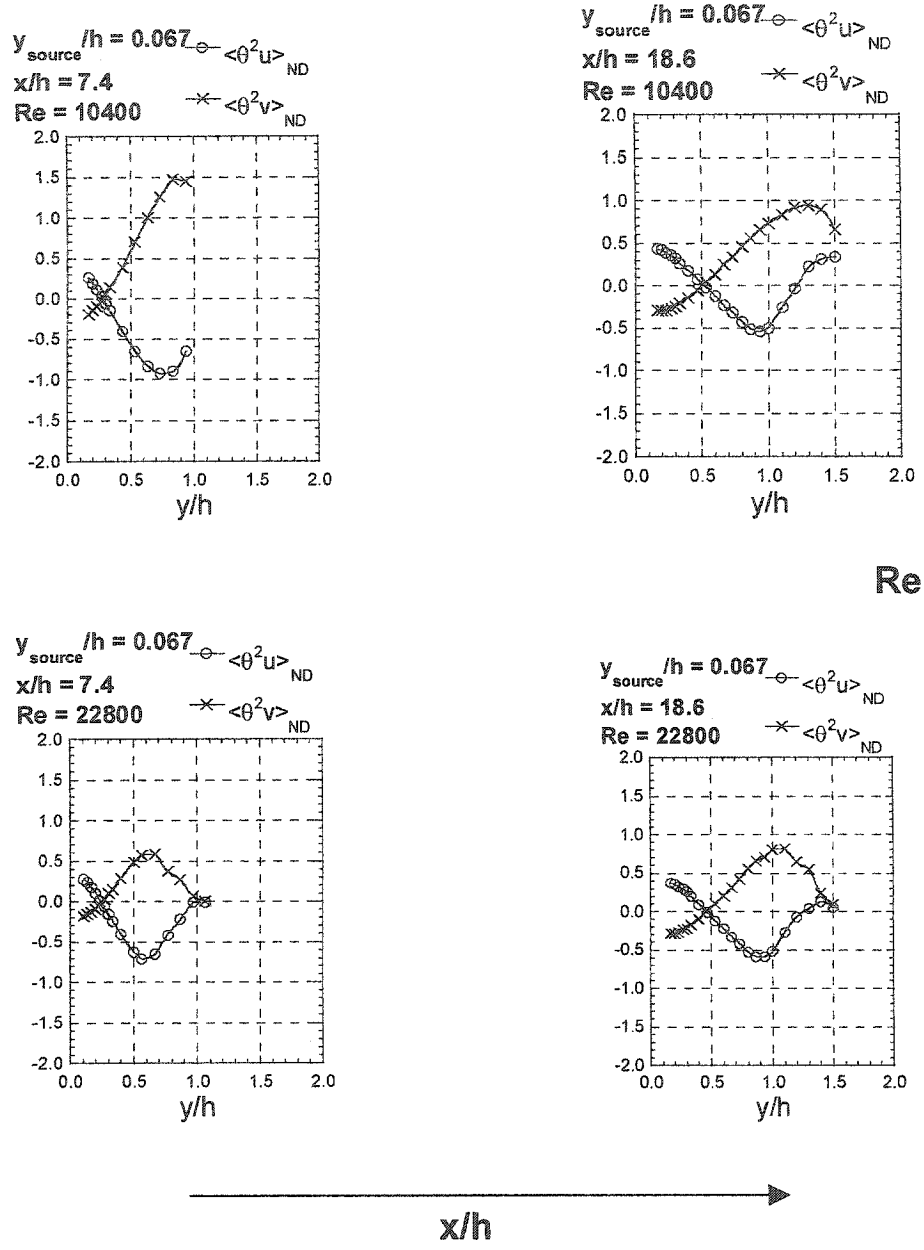


Figure 4.14 – Turbulent variance transport

4.5.3 Turbulent Heat Flux Transport

A non-dimensionalization similar to section 4.5.2 is employed with respect to the turbulent heat fluxes:

$$\langle u^2 \theta \rangle_{ND} = \frac{\langle u^2 \theta \rangle}{\langle u^2 \rangle \theta_{RMS}} \quad (4-11)$$

$$\langle v^2 \theta \rangle_{ND} = \frac{\langle v^2 \theta \rangle}{\langle v^2 \rangle \theta_{RMS}} \quad (4-12)$$

The non-dimensional turbulent heat flux transport is shown in figures 4.15 and 4.16. For all the y_{source} locations, the Reynolds number has little effect on these profiles, except that the profiles are thinner as the Re is increased.

For $y_{source} = 0.067$, the downstream location is seen to have little effect on these profiles, except that as the downstream distance is increased, the profile width also increases.

As with the previous velocity-temperature correlations, the source location is observed to have the greatest effect on these profiles. The near-wall y_{source} locations exhibit behavior similar to each other, however are quite different for the centerline source location. For the near-wall y_{source} locations, the $\langle u^2 \theta \rangle_{ND}$ and $\langle v^2 \theta \rangle_{ND}$ profiles are very similar, but are observed to differ for the centerline source location. Such a result is expected given the underlying symmetries of the flow.

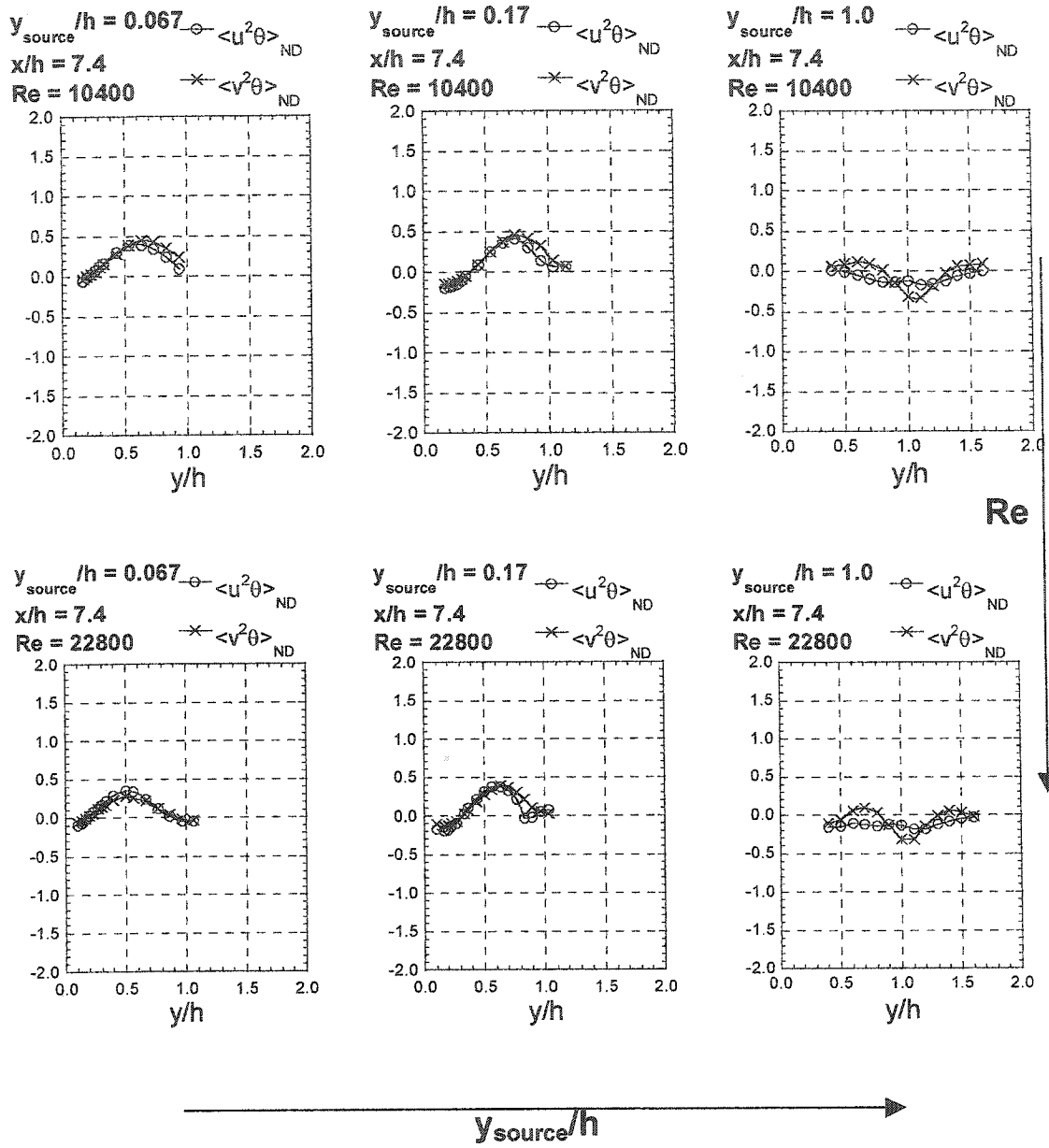
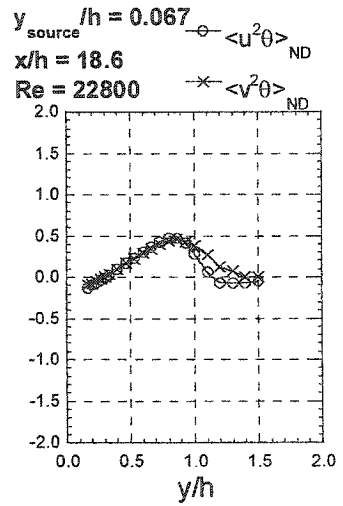
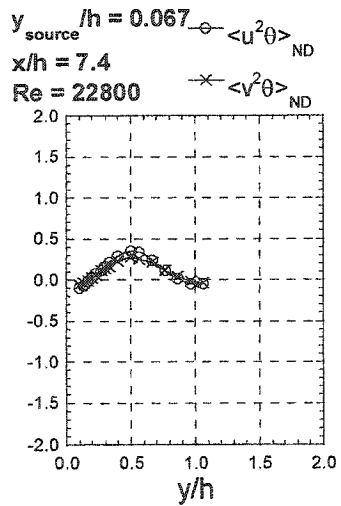
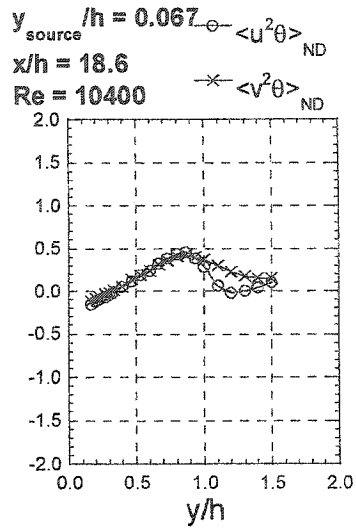
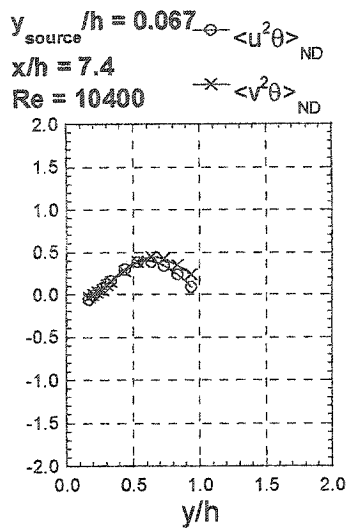


Figure 4.15 – Turbulent heat flux transport



Re

x/h →

Figure 4.16 – Turbulent heat flux transport

Chapter 5

Conclusions

5.1 Review of the Present Work and the Contributions

In Chapter 1, the objective of the thesis was stated. It was to experimentally study scalar dispersion from a concentrated source in one of the simplest inhomogeneous turbulent flows, fully developed turbulent channel flow. Next, the background and motivation leading to the present work were presented. Finally, the relevant literature was reviewed, which included the subjects of turbulent channel flow, turbulence measurement techniques, scalar dispersion in isotropic grid-generated turbulence, scalar dispersion in homogeneous turbulent shear flow, dispersion in inhomogeneous turbulence, and studies of numerically simulated scalar dispersion that complement experimental studies.

Chapter 2 presented the experimental facility and the techniques used to measure the turbulent velocity and scalar (temperature) fields. First, a detailed description of the channel flow facility and the scalar injection method was given. Next, the measurement methods were discussed. The temperature was injected via a fine line-source (spanning the spanwise direction of the channel), such that it would be passive (i.e., not affect the flow field). The resultant thermal plume was measured using hot-wire anemometry and cold-wire thermometry techniques, which were discussed in detail. Then, the resolution of the probes was discussed. Finally, the method of data acquisition was presented, which

included analogue to digital conversion and the convergence of the measured statistical values.

In Chapter 3, the experimental conditions were examined and the flow field was studied. To meet the objective of the thesis, the experiment had to meet the following conditions: the velocity field had to be fully developed channel flow, the scalar had to be passive, the walls had to be adiabatic, the temperature field had to be independent of the source size, and the temperature field had to be 2-D. Each of these criteria was examined by experimental and/or theoretical means. Various turbulent velocity field properties were also tabulated and discussed for the two Reynolds numbers used herein.

In Chapter 4, detailed measurements of the thermal plume were presented. The scalar was injected at 3 different locations with respect to the wall (in the fully developed region) for two Reynolds numbers. The mean and RMS temperature fields were presented and the results were compared with those of scalar dispersion from a line source in isotropic grid-generated turbulence and homogeneous turbulent shear flow. Next, the PDFs of the temperature field were presented. Then the transverse skewness profiles of the temperature field were examined. Finally, temperature-velocity correlations were presented.

It was found that:

1. Gaussian profiles (with reflection) fit the transverse mean temperature profiles well.

2. The peak of the transverse mean temperature profile was relatively fixed behind the source for the downstream positions under consideration.
3. The downstream decay of the peak mean temperature was proportional to $(x/h)^{-0.5}$, which is less than that of isotropic grid-generated turbulence and homogeneous turbulent shear flow.
4. The width of the transverse mean temperature profile was thinner at the higher Reynolds number, due to the increased advection. This trend was also observed in the measurements of the other statistical quantities.
5. Truncated Gaussian profiles fit the transverse RMS temperature profiles well.
6. The decrease in the downstream peak of the RMS temperature profiles was proportional to $(x/h)^{-1}$, which is less rapid than that in isotropic grid-generated turbulence and homogeneous turbulent shear flow.
7. The peak of the transverse RMS temperature profiles drifted toward the channel centerline for the near-wall source locations.
8. With increasing distance from the wall, the PDFs of the near-wall source location evolved from quasi-Gaussian to very positively skewed PDFs.
9. The PDF directly downstream of the source approached a Gaussian shape for all source locations, implying that the plume was better mixed with downstream distance.

10. The near-wall PDFs indicate the scalar distribution is better mixed at the higher Reynolds number even though they have been mixing for less time.
11. For the near-wall source locations, the skewness was initially positive, decreasing with downstream distance, and eventually becoming negative.
12. The Reynolds number had little effect on the overall shape of the transverse velocity -temperature correlation profiles.
13. Non-dimensionalized turbulent variance transport correlations showed a strong Reynolds number dependence. This was attributed to the dependence of the non-dimensionalization on the shape of the scalar PDF (in particular, its kurtosis) at a given measured position.
14. Near-wall source locations ($y_{\text{source}}/h = 0.067$ and 0.17) exhibit similar behavior to dispersion from a line source placed in a turbulent boundary layer (in the studied region).

5.2 Extensions of the Present Work

An immediate extension of this work would be to acquire near-wall data of the temperature field. A cold-wire boundary layer probe should be used to take these measurements.

The work herein focused on scalar dispersion in the direction of the flow inhomogeneity. If the line source was perpendicular to the wall (in the y-direction), the scalar dispersion occurs in one of the homogeneous directions (the z-

direction). A detailed measurement set of this source orientation would be beneficial in highlighting the effect of the flow inhomogeneity on dispersion that is occurring in a direction perpendicular to the inhomogeneity.

Finally, this work can be extended to the interference of thermal plumes from two (or more) line sources as did Warhaft (1984) (in isotropic grid-generated turbulence). Two line sources can be simultaneously placed in the channel, and the evolution of the correlation coefficient of scalar concentration from the interfering plumes can be studied and compared to the existing data obtained in isotropic grid-generated turbulence. Experiments of this kind study how two contaminants mix in a separate medium, where dispersion and mixing are intimately connected.

References

- Anand, M.S. and Pope, S.B. 1983 Diffusion behind a line source in grid turbulence. *Proc. 4th Symp. on Turbulent Shear Flows*.
- Antonia, R.A., Zhou, T., and Romano, G.P. 1997 Second- and third-order longitudinal velocity structure functions in a fully developed turbulent channel flow. *Phys. Fluids* 9 (11), 3465-3471.
- Bara, B.M., Wilson, D.J., and Zelt, B.W. 1992 Concentration fluctuation profiles from a water channel simulation of a ground-level release. *Atm. Env.* 26A, 1053-1062.
- Batchelor, G.K. 1953 *The Theory of Homogeneous Turbulence*, Cambridge University Press.
- Bernard, P. S. and Rovelstad, A. L. 1994 On the physical accuracy of scalar transport modeling in inhomogeneous turbulence. *Phys. Fluids* 6 No. 9, 3093-3108.
- Blevins, R.D. 1990 *Flow-Induced Vibrations*, Second Edition; Krieger.
- Brown, L.W.B., Antonia, R.A., and Chua, L.P. 1989 Calibration of X-probes for turbulent flow measurements. *Exp. Fluids* 7, 201-208.
- Brunn, H.H. 1995 *Hot-Wire Anemometry*, Oxford University Press.
- Chung, M. K., and Kyong, N. H. 1989 Measurement of turbulent dispersion behind a fine cylindrical heat source in a weakly sheared flow. *J. Fluid Mech.* 205, 171-193.
- Cremer, M.A., McMurtry, P.A., and Kerstein, A.R. 1994 Effects of turbulence length-scale distribution on scalar mixing in homogeneous turbulent flow. *Phys. Fluids* 6 No. 6, 2143-2153.
- Dinavahi, S. P.G., Breuer, K. S., and Sirovich, L. 1995 Universality of probability density functions in turbulent channel flow. *Phys. Fluids* 7 (5), 1122-1129.
- Fackrell, J.E. and Robins, A.G. 1982 Concentration fluctuations and fluxes in plumes from point source in a turbulent boundary layer. *J. Fluid Mech.* 117, 1-26.
- Frisch, U. 1995 *Turbulence: The Legacy of A.N. Kolmogorov*, Cambridge, U.K.: Cambridge Univ. Press.
- Goldstein, R. J. 1996 *Fluid Mechanics Measurements*, Taylor and Francis.

Gunther, A., Papavassiliou, D.V., Warholic, M.D., and Hanratty, T.J. 1998 Turbulent flow in a channel at a low Reynolds number. *Exp. Fluids* **25**, 503-511.

Hinze, J.O. 1975 *Turbulence*, McGraw-Hill.

Ilipoulos, I., and Hanratty, T. J. 1999 Turbulent dispersion in a non-homogenous field. *J. Fluid Mech.* **392**, 45-71.

Incropera, F.P., Kerby, J.S., Moffatt, D.F., and Famadhyani, S. 1986 Convection heat transfer from discrete heat sources in a rectangular channel. *Int. J. Heat Mass Transfer* **29**, 1051-1058.

Jorgensen, F. E. 2002 How to measure turbulence with hot-wire anemometers-a practical guide. *Dantec Dynamics*.

Kabiri, M.E., Paranthoen, P., Rosset, L., and Lecordier, J.C. 1998 Fluctuations de température et flux de chaleur en aval d'une source lineaire placee dans une couche limite turbulente. *Rev. Gen. Therm* **37**, 181-194.

Karnik, U. and Tavoularis, S. 1989 Measurements of heat diffusion from a continuous line source in a uniformly sheared turbulent flow. *J. Fluid Mech.* **202**, 233-261.

Khoo, B.C. 2000 On near-wall hot-wire measurements. *Exp. Fluids* **29**, 448-460.

Kolmogorov, A.N. 1941 The local structure of turbulence in incompressible viscous fluid for very large Reynolds number, *Dokl. Akad. Nauk SSSR* **30**, 9-13.

Kontomaris, K. and Hanratty, T.J. 1994 Effect of a molecular diffusivity on point source diffusion in the center of a numerically simulated turbulent channel flow. *Int. J. Heat Mass Transfer* **37** No. 13, 1817-1828.

Legg, B.J., Raupach, M.R., and Coppin, P.A. 1986 Experiments on scalar dispersion within a model plant canopy Part III: An elevated line source. *Boundary-Layer Meteorology* **35**, 277-302.

Lemay, J. 2001 Constant current anemometer utilization guide. University Laval, Quebec, Canada.

Lesieur, M. 1997 *Turbulence in Fluids*, Dor-drecht: Kluwer.

Lienhard, J.H. 1988 The decay of turbulence in thermally stratified flow. Ph.D. Thesis, University of California, San Diego.

Lumley, J.L. and Panofsky, H.A. 1964 *The structure of atmospheric turbulence*, Interscience Publishers.

Lyons, S.L. and Hanratty, T.J. 1991 Direct numerical simulation of passive heat transfer in a turbulent channel flow. *Int. J. Heat Mass Transfer* **34** No. 4/5, 1149-1161.

Mathieu, J. and Scott, J. 2000 *An Introduction to Turbulent Flow*, Cambridge Univ. Press.

Monin, A.S. and Yaglom, A.M. 1975 *Statistical Fluid Mechanics*, MIT Press.

McLeod, M. S. 2000 On the design and testing of a high-aspect ratio channel for turbulent flow measurements. McGill University, Honours Thesis.

Onorato, M., Camussi, R., and Iuso, G. 2000 Small scale intermittency and bursting in a turbulent channel flow. *The American Physical Society* **61** No. 2, 1447-1454.

Na, Y. and Hanratty, T.J. 2000 Limiting behavior of turbulent scalar transport close to a wall. *Int. J. Heat Mass Transfer* **43**, 1749-1758.

Papavassiliou, D. V., and Hanratty, T. J. 1997 Transport of a passive scalar in a turbulent channel flow. *Int. J. Heat Mass Transfer* **40** No. 6, 1303-1311.

Paranthoen, P. and Lecordier, J.C. 1996 Mesures de température dans les écoulements turbulents. *Rev. Gen. Therm.* **35**, 282-308.

Paranthoen, P., Fouari, A., Dupont, A., and Lecordier, J.C. 1988 Dispersion measurements in turbulent flows (boundary layer and plane jet). *Int. J. Heat Mass Transfer* **31**, 153-165.

Perry, A.E. 1982 *Hot-Wire Anemometry*, Clarendon Press.

Pope, S.B. 2000 *Turbulent Flows*, Cambridge Univ. Press.

Rajaei, M., Karisoon, S., and Sirovich, L. 1995 On the streak spacing and vortex roll size in a turbulent channel flow. *Phys. Fluids* **7** (10), 2439-2443.

Raupach, M.R., Coppin, P.A., and Legg, B.J. 1986 Experiments on scalar dispersion within a model plant canopy Part I: The turbulent structure. *Boundary-Layer Meteorology* **35**, 21-52.

Raupach, M.R. and Legg, B.J. 1983 Turbulent dispersion from an elevated line source: measurements of wind-concentration moments and budgets. *J. Fluid Mech.* **136**, 111-137.

- Sawford, B.L. and Hunt, J.C. 1986 Effects of turbulence structure, molecular diffusion and source size on scalar fluctuations in homogeneous turbulence. *J. Fluid Mech.* **165**, 373-400.
- Shah, D.A., Chambers, A.J., and Antonia, R.A. 1983 Reynolds number dependence of a fully developed turbulent duct flow. Eighth Australian Fluid Mechanics Conference, University of New Castle.
- Shlien, D.J. and Corrsin, S. 1976 Dispersion measurements in a turbulent boundary layer. *Int. J. Heat Mass Transfer* **19**, 285-295.
- Sreenivasan, K.R. 1991 On local isotropy of passive scalars in turbulent shear flows. *Proc. R. Soc. London. Ser. A* **434**, 165-182.
- Stapountzis, H., Sawford, B.L., Hunt, J.C.R., and Britter, R.E. 1986 Structure of the temperature field downwind of a line source in grid turbulence. *J. Fluid Mech.* **165**, 401-424.
- Taylor, G.I. 1935 Statistical theory of turbulence. IV-Diffusion in a turbulent air stream. *Proc. R. Soc. Lond. A* **151**, 465-478.
- Taylor, G.I. 1953 Dispersion of soluble matter in solvent flowing slowly through a tube. *Proc. R. Soc. London Ser. A* **219**, 186-203.
- Tennekes, H. and Lumley, J.L. 1972 *A First Course in Turbulence*, MIT Press.
- Tong, C. and Warhaft, Z. 1995 Passive scalar dispersion and mixing in a turbulent jet. *J. Fluid Mech.* **292**, 1-38.
- Townsend, A.A. 1976 *The Structure of Turbulent Shear Flow*, Cambridge Univ. Press.
- Townsend, A.A. 1954 The diffusion behind a line source in homogeneous turbulence. *Proc. R. Soc. Lond. A* **224**, 487.
- Uberoi, M.S. and Corrsin, S. 1952 Diffusion from a line source in isotropic turbulence. *NACA Tech. Note* 2710 (also *NACA Rep.* 1142).
- Veeravalli, S. and Warhaft, Z. 1990 Thermal dispersion from a line source in the shearless turbulence mixing layer. *J. Fluid Mech.* **216**, 35-70.
- Villermaux, E., Innocenti, C., and Duplat, J. 2001 Short circuits in the Corrsin-Obukhov cascade. *Phys. Fluids* **13** No. 1, 284-289.

Vincont, J.Y., Simoens, S., Ayrault, M., and Wallace, J.M. 2000 Passive scalar dispersion in a turbulent boundary layer from a line source at the wall and downstream of an obstacle. *J. Fluid Mech.* **424**, 127-167.

Warhaft, Z. 1981 The use of dual heat injection to infer scalar covariance decay in grid turbulence. *J. Fluid Mech.* **104**, 93-109.

Warhaft, Z. 1984 The interference of thermal fields from line sources in grid turbulence. *J. Fluid Mech.* **144**, 363-387.

Warhaft, Z. 2000 Passive scalars in turbulent flows. *Annu. Rev. Fluid Mech.* **32**, 203-240.

Wark, K. and Warner, C. F. 1981 *Air Pollution: Its Origin and Control*, Second Edition, Harper Collins Publishers.

Wilson, J.D., Flesch, T.K., and Swaters, G.E. 1993 Dispersion in sheared Gaussian homogeneous turbulence. *Boundary-Layer Meteorology* **62**, 281-290.

Wyngaard, J.C. 1968 Measurements of small-scale turbulence structure with hot wires. *J. Sci. Instr. Series 2* **1**, 1105-1108.

Appendix I

PDF and Temperature-Velocity Correlation Database

The following figures are a comprehensive database of PDFs and temperature-velocity correlations, that were measured but not necessarily presented in Chapter 4. For each Re and source location, there is a PDF figure and a temperature-velocity correlation figure. The PDF figure shows the transverse PDFs at the various downstream locations. The temperature-velocity correlation figure shows the different transverse correlation profiles at the various downstream locations.

The figures are presented as follows:

Figure A-1 – PDFs: $Re=10400$; $y_{source}=0.067$

Figure A-2 – Temperature-velocity correlations:
 $Re=10400$; $y_{source}=0.067$

Figure A-3 – PDFs: $Re=22800$; $y_{source}=0.067$

Figure A-4 – Temperature-velocity correlations:
 $Re=22800$; $y_{source}=0.067$

Figure A-5 – PDFs: $Re=10400$; $y_{source}=0.17$

Figure A-6 – Temperature-velocity correlations:
 $Re=10400$; $y_{source}=0.17$

Figure A-7 – PDFs: $Re=22800$; $y_{source}=0.17$

Figure A-8 – Temperature-velocity correlations:
 $Re=22800$; $y_{source}=0.17$

Figure A-9 – PDFs: $Re=10400$; $y_{source}=1.0$

Figure A-10 – Temperature-velocity correlations:
 $Re=10400$; $y_{source}=1.0$

Figure A-11 – PDFs: $Re=22800$; $y_{source}=1.0$

Figure A-12 – Temperature-velocity correlations:
 $Re=22800$; $y_{source}=1.0$

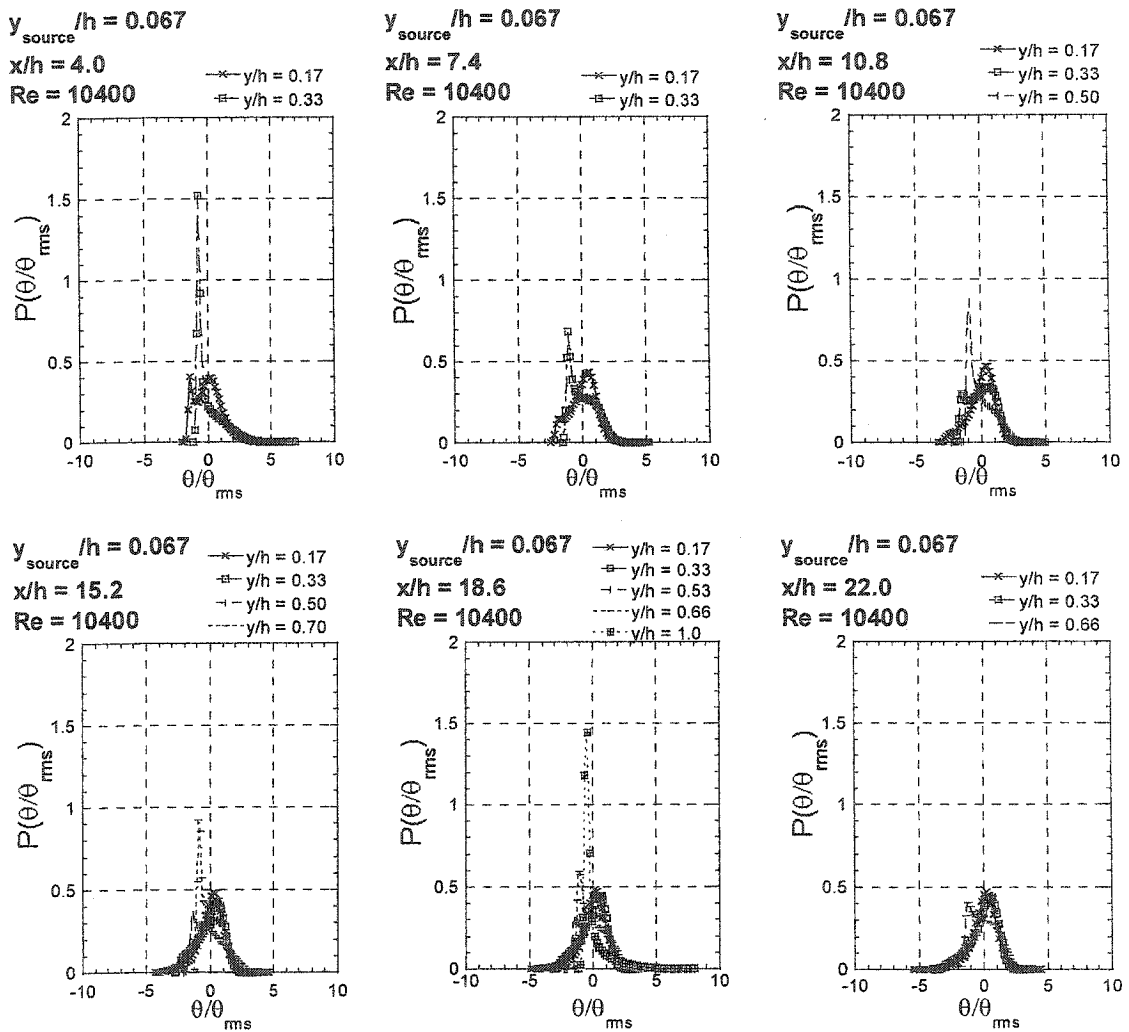


Figure A-1 – PDFs: $Re=10400$; $y_{source}=0.067$

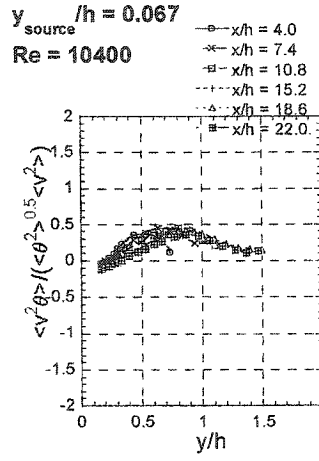
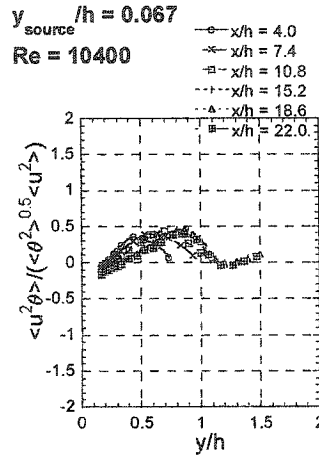
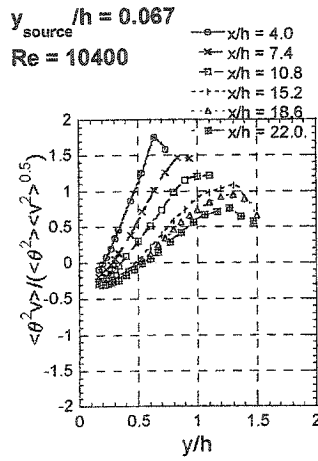
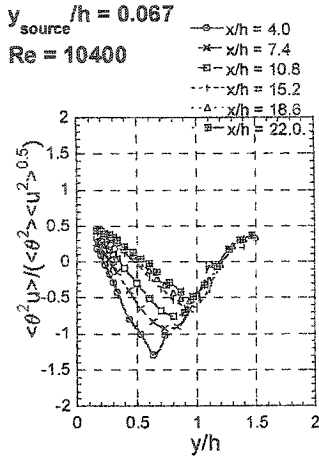
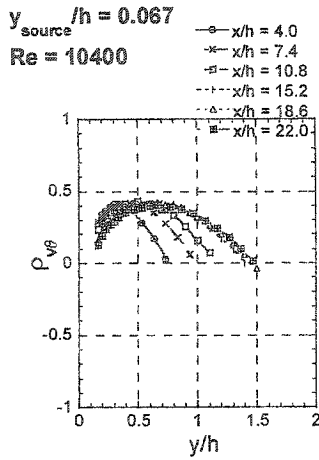
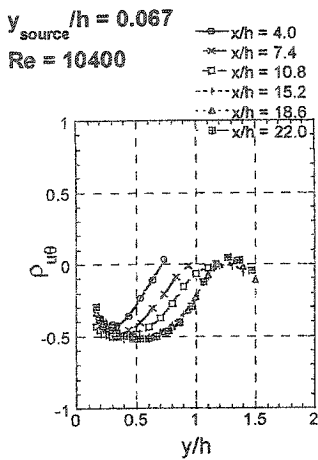


Figure A-2 – Temperature-velocity correlations: $Re=10400$; $y_{source}=0.067$

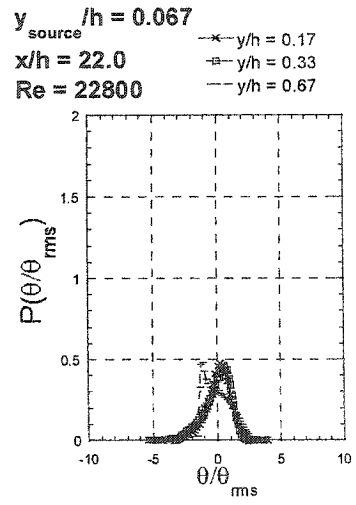
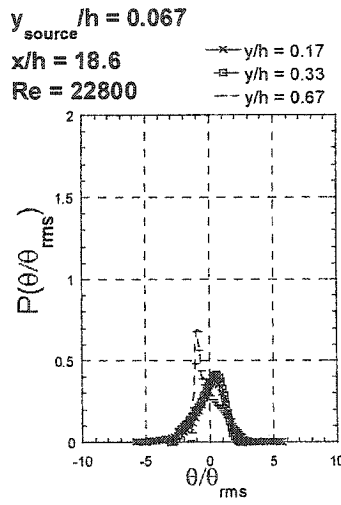
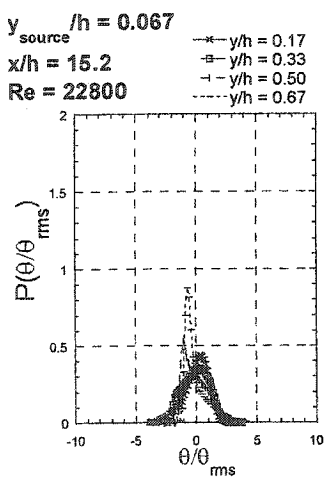
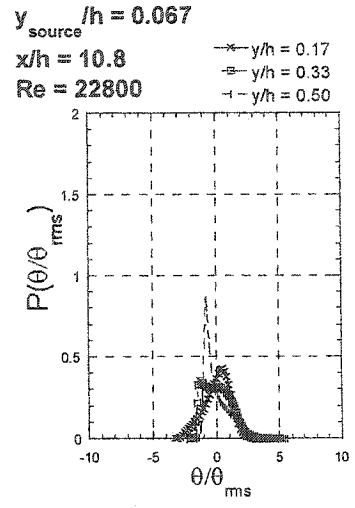
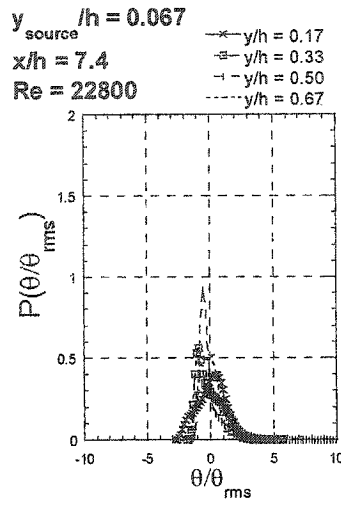
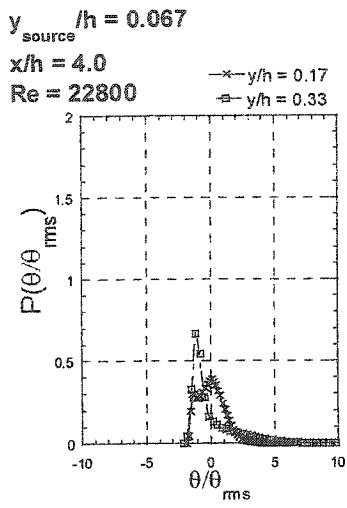


Figure A-3 – PDFs: $Re=22800$; $y_{source}=0.067$

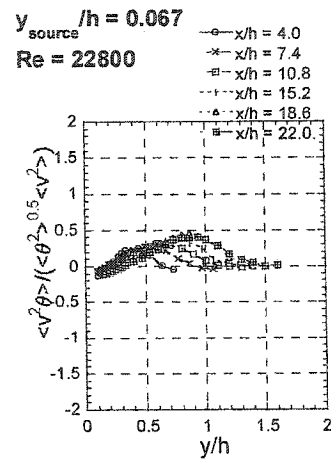
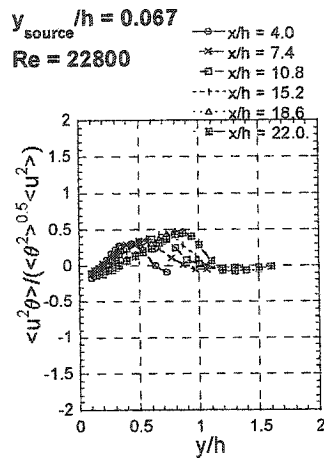
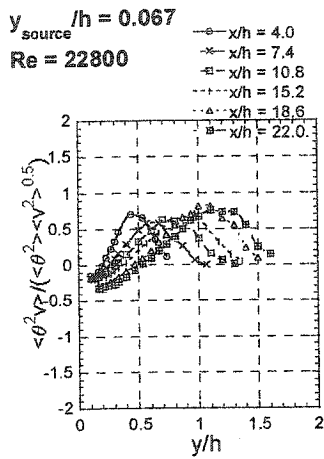
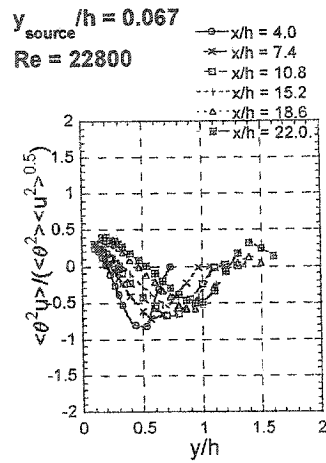
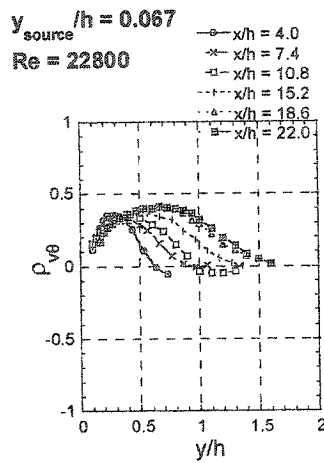
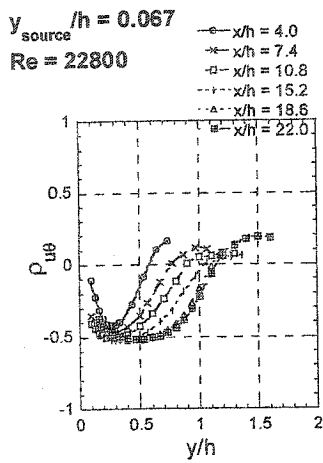


Figure A-4 – Temperature-velocity correlations: $Re=22800$; $y_{source}=0.067$

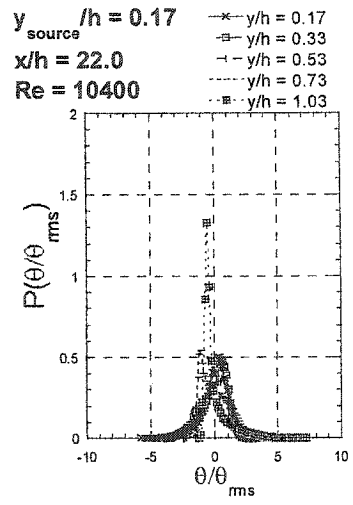
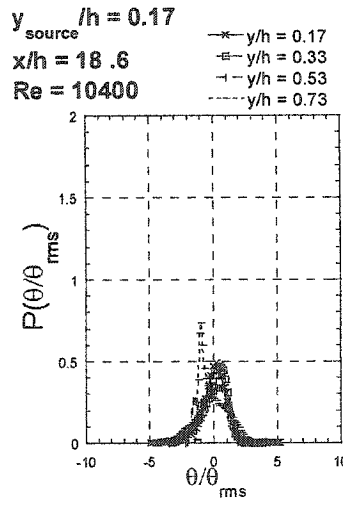
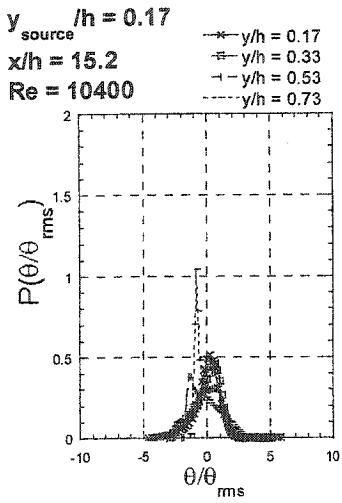
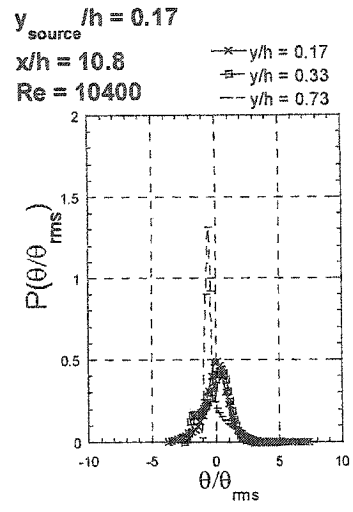
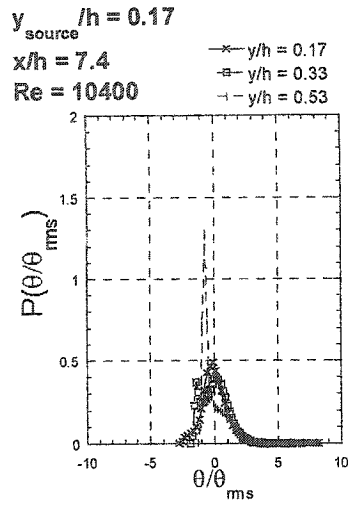
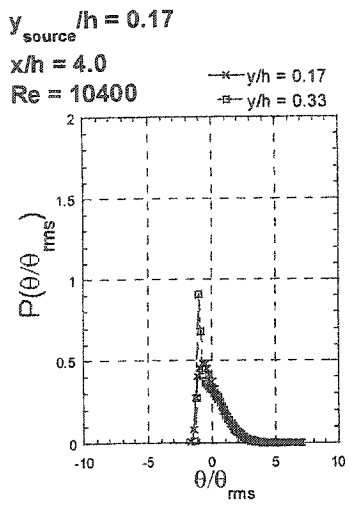


Figure A-5 – PDFs: $Re=10400$; $y_{source}=0.17$

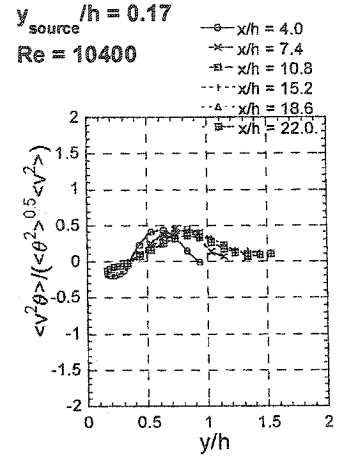
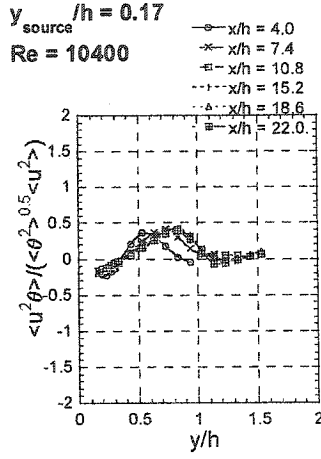
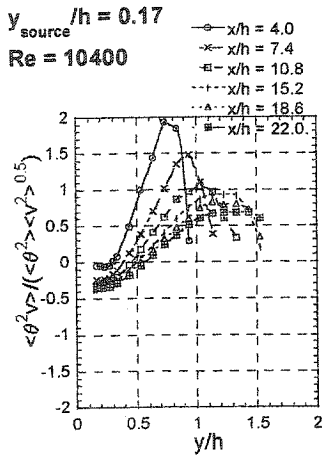
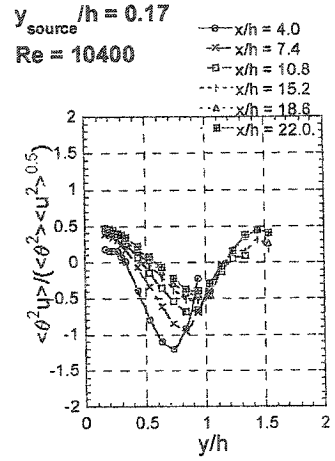
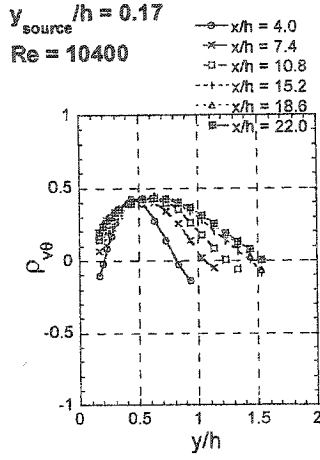
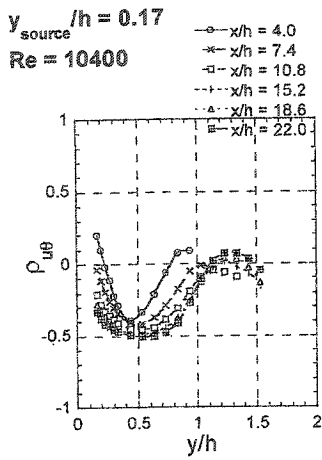


Figure A-6 – Temperature-velocity correlations: $Re=10400$; $y_{source}=0.17$

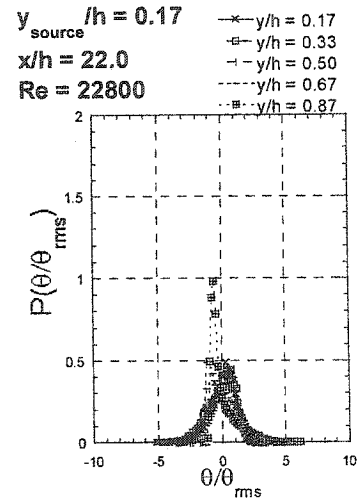
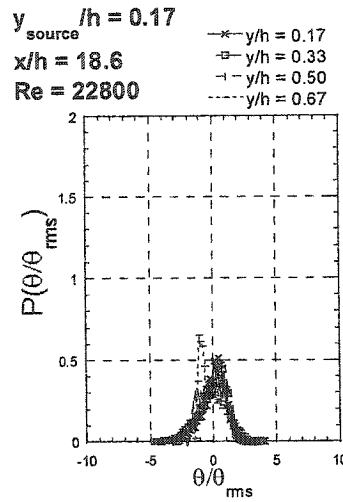
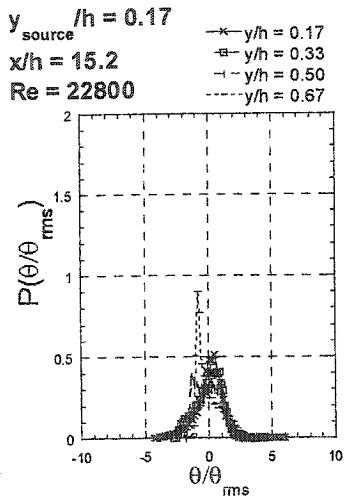
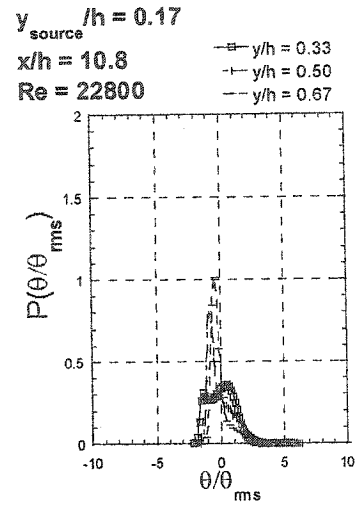
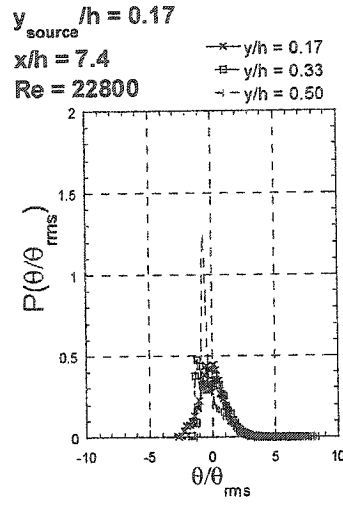
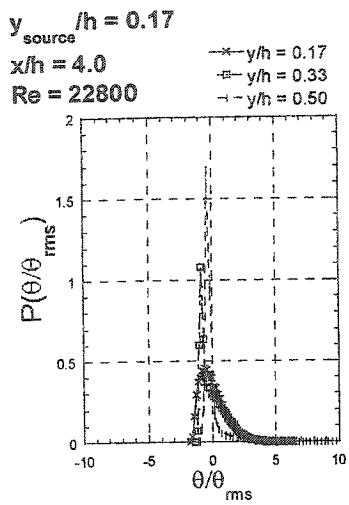


Figure A-7 – PDFs: $Re=22800$; $y_{source}=0.17$

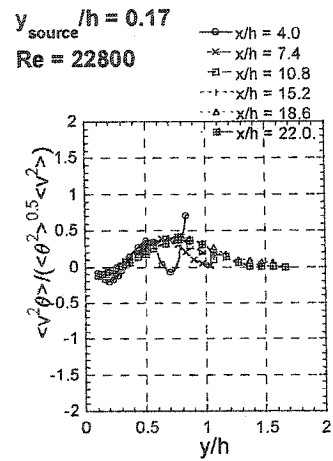
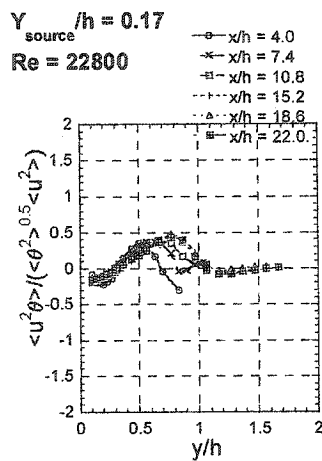
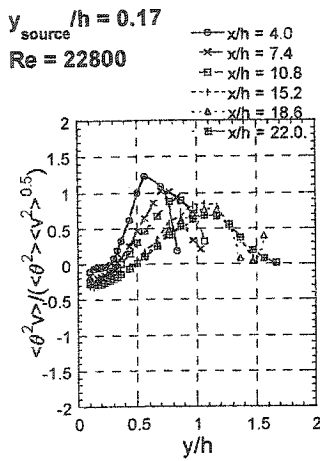
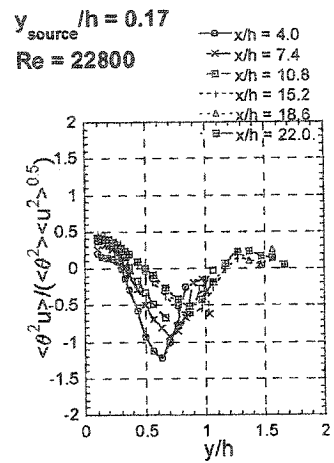
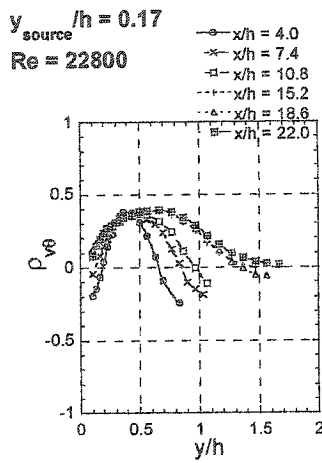
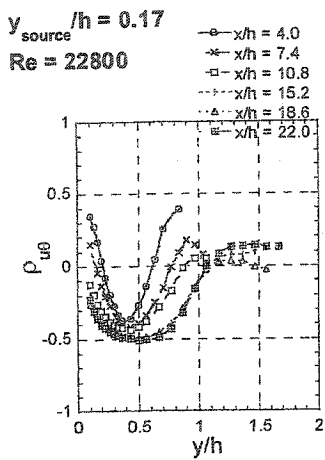


Figure A-8 – Temperature-velocity correlations: $Re=22800$; $y_{source}=0.17$

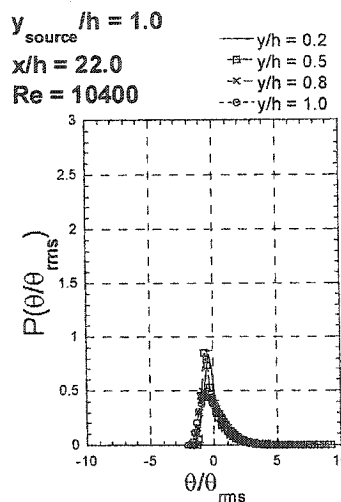
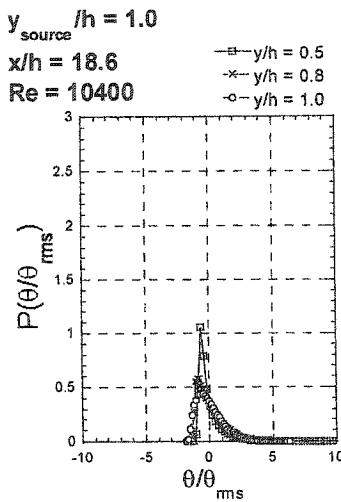
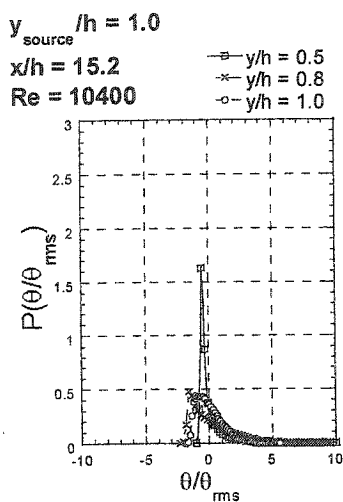
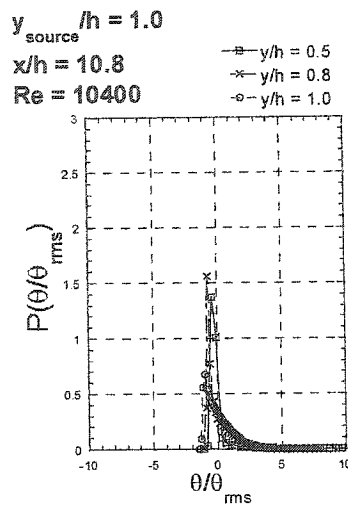
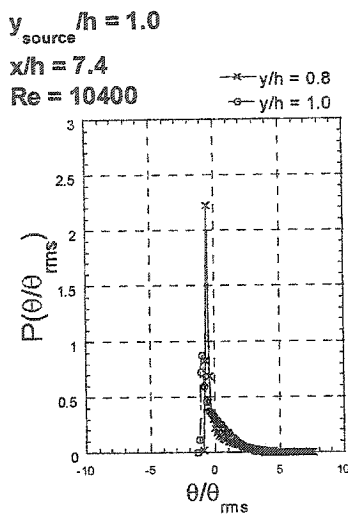
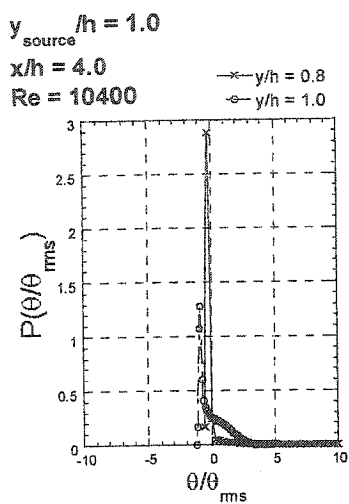


Figure A-9 – PDFs: $Re=10400$; $y_{source}=1.0$

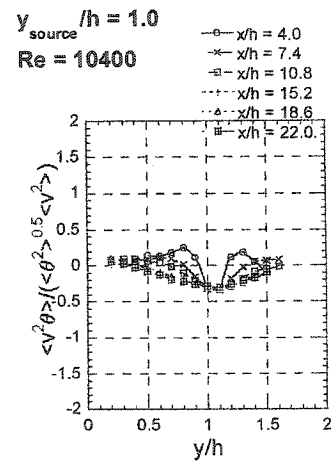
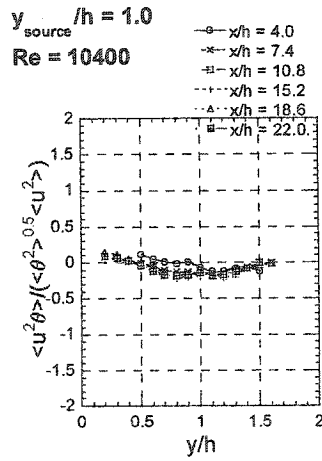
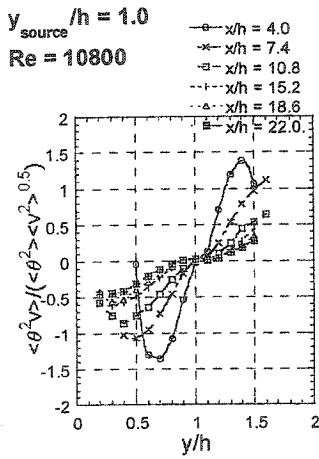
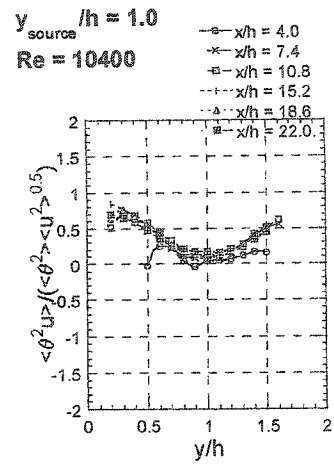
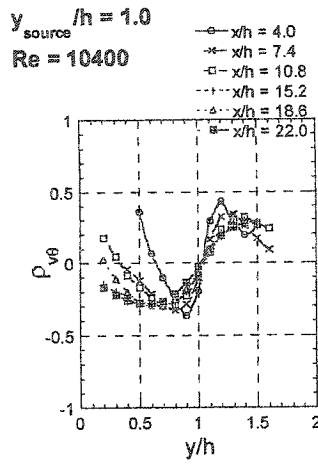
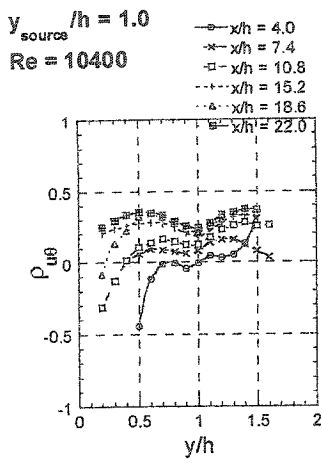


Figure A-10 – Temperature-velocity correlations: $Re=10400$; $y_{source}=1.0$

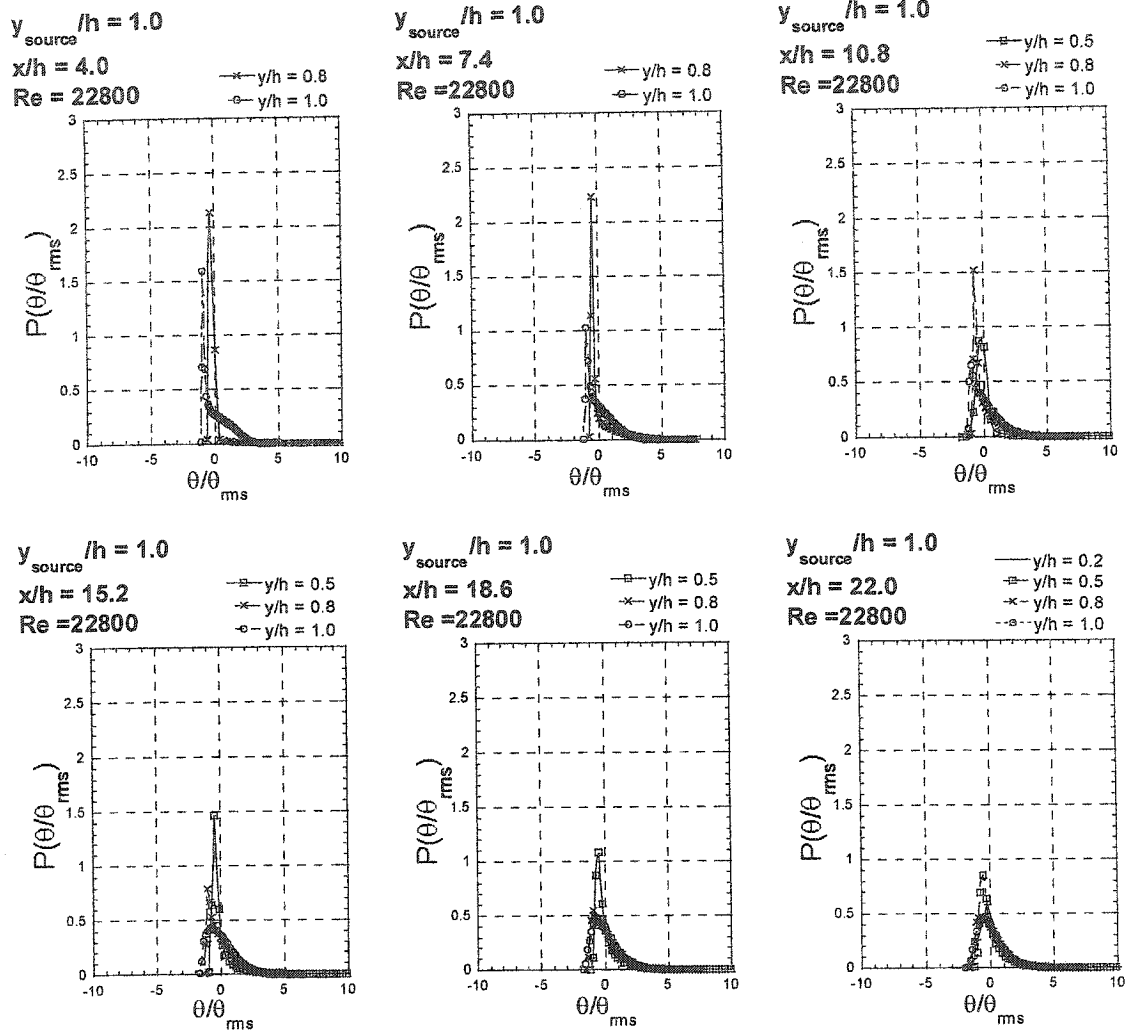


Figure A-11 – PDFs: $Re=22800$; $y_{source}=1.0$

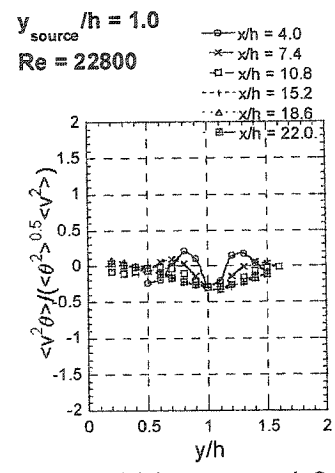
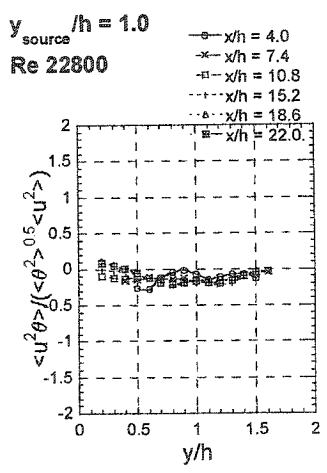
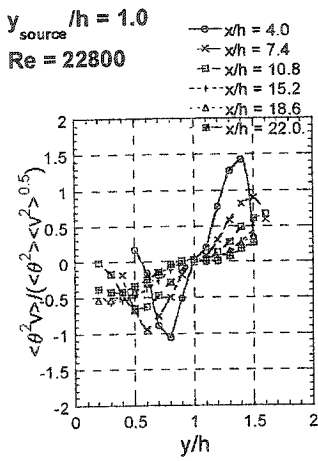
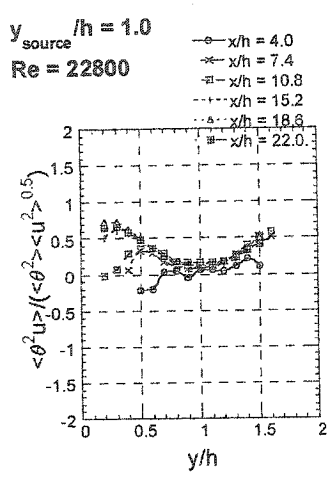
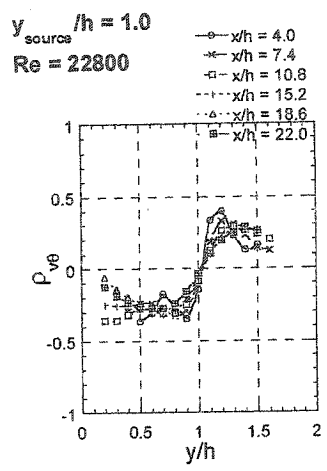
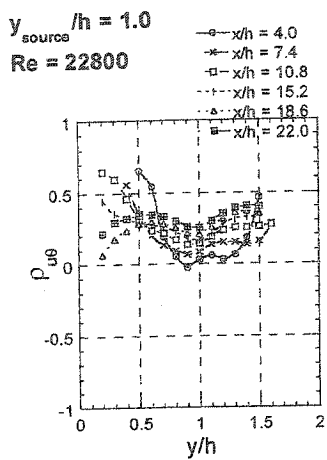


Figure A-12 – Temperature-velocity correlations: $Re=22800$; $y_{source}=1.0$